UNIVERSITÀ DI PARMA

UNIVERSITÀ DEGLI STUDI DI PARMA

DOTTORATO DI RICERCA IN
"TECNOLOGIE DELL'INFORMAZIONE"

CICLO XXXVI

Experimental characterization and modelling of specialty optical fibres for bio-medical applications

Coordinatore:
Prof. Marco Locatelli

Tutors:
Prof. Annamaria Cucinotta
Prof. Federica Poli

Dottoranda: Foroogh Khozeymeh Sarbishe

Anni 2020-2023

I dedicate my thesis to my mother, Mina Alikhani. Words can hardly describe my thanks and appreciation to you. Without your endless love and encouragement, I would never have been able to complete my graduate studies. I am truly thankful and honored to have you as my mother. I love you and I appreciate everything that you have done for me.

Contents

Introduction

Specialty optical fibers (SOF) which have at least one property different from standard ones are gaining more and more attention in bio-medical applications. These fibers include a wide group of liquid core fibers, photonic crystal fibers (PCFs), and active fibers. Particularly during the last years, employing the PCFs as optical biosensors has received much attention in the scientific community. Generally speaking, optical biosensors are of special interest because of the increasing demand for biological and chemical analyte detection in a wide range of applications including clinical analysis [1], food quality control [2], defense and security [3], and environmental monitoring [4]. Briefly, a biosensor device is made of three main elements: the biorecognition element, the transducer, and the receiver. There are different kinds of biosensors named electrochemical, thermometric, piezoelectric, and magnetic sensors [5, 6]. Among them, especially, optical biosensors look promising for point-of-care-based diagnosis [1] and food quality control [2]. These biosensors are modern analytical devices that employ light-guiding technologies as their transducer part and exploit the properties of light for bio/analyte detection. Changes in the optical properties of the light in contact with the bio/chemical analytes lead to changes in the output spectrum or the electrical signal recorded by the photodetector. Some of the advantages of optical biosensors compared with other sensors are the immunity of EM fields to electrical noises, higher sensitivity, simpler mechanism and detection protocol, more reliability, more flexibility, lower cost, and more compactness [5]. Regarding the pros of being simple, compact, and usability with untrained personnel, particularly label-free optical biosensors are attracting more attention [5].

In this scheme of detection, the bio/chemical analytes are directly detected without the laborious process of analyte molecule labeling [7, 8, 9]. Regarding their transducer part, optical biosensors are categorized into different groups resonator-based [10, 11, 12], waveguide-based [13, 14], and interferometric-devices based [15, 16]. Although these optical sensors have demonstrated high sensitivities for both bulk and surface sensing measurements [17, 18, 19], they still suffer from a critical issue. Indeed, the integration need of photonic and fluidic technologies [20, 21] envisages unified sensor devices. PCF-based biosensors are a group of optical biosensors that meet the need for effective integration between fluidics and photonics [22, 23]. The integration of fluidics and photonics in these miniaturized structures may pave the way for lab-in-fiber technologies employing in vivo biosensing [21]. PCFs can be referred to the structures that confine the light inside a core surrounded by a microstructured cladding composed of air holes running along the length of the fiber [22]. Thus, gas or liquid solutions can be infiltrated inside these air holes leading to the creation of biological layers on the dielectric inner walls of the fiber [24]. This advantage can be further exploited if HC-PCFs are considered thanks to the possibility of having a strong interaction between the sample and the light guided by the fiber. HC-PCFs can rely on two different transmission mechanisms: Photonic Band-gap (PBG) or inhibited coupling (IC) [25]. The former presents disadvantages in terms of bandwidth and, moreover, this mechanism requires complicated microstructured cladding, while the latter allows covering a wider range of wavelengths. The transmission spectra of this kind of fiber are characterized by an alternating sequence of high and low transmission bands. In particular, there is high transmission when the coupling between the fundamental core mode and the cladding modes is prevented [26]. The position of the transmission bands is defined by the thickness of the microstructured cladding which can be composed of much simpler structures and larger pitches with respect to PBG fibers, allowing easier infiltration of solutions. So, HC-IC specialty fibers represent a promising platform for the development of label-free sensors for biological molecule detection [25, 27]. The formation of a biological layer due to the molecular interaction of the target analyte with the suitably functionalized glass core surface is exploited for detection because it changes the thickness of cladding that is directly

translated into a red shift in the transmission spectrum of the fiber without the use of additional transducers. In the first part of this thesis, we aim to demonstrate, as a proof of concept, the suitability of the HC-IC specialty fibers as a platform for DNA detection. For this purpose, two different kinds of HC-IC specialty fibers, tube-lattice (TL), and Kagome-lattice (KL) HC-IC fibers have been selected for DNA detection. Then precise functionalization process of the inner surface of the fiber has been performed. In the functionalization process, new steps have been added to increase the possibility of DNA detection. The experimental setup including optical and chemical parts, the methods, and the material are explained in Chapter 1, and the obtained results, their analysis, and reliability will be discussed in Chapter 2.

In Chapter 3, we will deal with another kind of specialty fiber used to develop yellow lasers for ophthalmology applications. These lasers have proven to be effective in treating a variety of retinal diseases. Recently, visible lasers with applications in medicine, biology, metrology, optical storage, and display technology have been interesting subjects for many research worldwide groups [28]. For visible laser generation, there are several techniques based on gas lasers, Dye lasers, second harmonic generation (SHG), or optical parametric oscillator (OPO) techniques that can be adapted for visible laser development [29, 30, 31]. Nevertheless, in general, these techniques suffer from low efficiency, complexity, and high costs. On the other hand, fiber lasers have the advantages of high beam quality, stability, excellent excitation efficiency, and an alignment-free design which enables low-cost and high-quality lasers. Particularly yellow fiber-based lasers emitting around 565-590 nm are of particular interest for their existing and potential applications in sodium laser guide star [32], optical clock [33], ophthalmology [34], and in particular medical treatment for diabetic retinopathy (DR) [35]. DR is the most common eye disease among diabetic patients which causes vision impairment and blindness. In the treatment of DR, experimental investigations on animals and humans, but also numerical analysis, have confirmed that yellow laser emission is the most suitable candidate, because it is effective with low power, and presents good clinical results with minimal collateral effects [36, 35, 37]. So far yellow emission has been possible with several techniques from copper bromide laser [38], Yb−doped fiber [39], bi−fiber lasers [40], opti-

cally pumped semiconductor lasers [41]. However, these techniques demand bulky structures with several free-space alignments, high maintenance, and tight limitations on the pump conditions. For accessing high-efficiency and simple direct yellow laser emission, particularly dysprosium Dy−doped ZBLAN fiber lasers exploiting transition from $^4F_{9/2}$ to $^6H_{13/2}$ level, is a desirable candidate. Therefore, the design, modeling, and fabrication of compact and efficient Dy−doped yellow fiber lasers are of critical importance. In 2001 [42], the first CW yellow emission in a Dy−doped ZBLAN fiber laser was demonstrated. Although Dy−doped yellow fiber lasers have been analyzed in some other research works [30, 43, 44], still the reported slope efficiencies were less than 13.2%. Indeed, in a considerable time, due to the lack of high-performance gain fibers and high-power GaN blue lasers as the pumping sources, no significant research progress has been observed in Dy−doped fiber yellow lasers. In 2020, thanks to the breakthroughs of both Dy−doped fluoride fibers and high-power blue GaN laser diodes, the first Dy−doped ZBLAN fiber laser pumped by GaN laser diode, emitting at 445 nm, was reported [45]. In that experiment, the maximum laser slope efficiency of 2.3% and 0.9% was reported for absorbed pump power in a Dy−doped fiber with lengths of 0.6 m and 5.95 m. In 2021, the same researchers investigated the potential causes of the low experimental slope efficiency and found contributions from the background loss of the fiber and excited-state absorption (ESA) of the intracavity yellow light [46]. They measured a maximum slope efficiency of 33% [46], which is still less than half of the Stokes limit which is about 78%. Recently, Dy−doped multi-component phosphate glass was examined and showed a strong yellow emission which was due to the high asymmetry and covalency of the local field and the high phonon energy [47]. In that work, Dy−doped multi-component phosphate core glass fiber was successfully drawn by using a rod-in-tube method. Furthermore in [48], another Dy−doped $NaLa(WO_4)_2$ glass ceramic fiber with good uniformity was fabricated using the molten core method, showing that it can be a very promising material candidate for tunable yellow lasers [48]. Despite these positive results in the fabrication technology of new glasses, the most promising commercially available Dy−doped fiber is the ZBLAN one produced by Le Verre Fluoré, France [49]. Interesting results have been obtained so far with this

fiber [46, 45, 50], even if the maximum reported slope efficiency is still quite low. Until now, few research works have dealt fully with the causes of the low slope efficiency in Dy−doped fiber yellow lasers. Therefore, it is necessary to propose more numerical and analytical methods for further improvements in the performance of Dy−doped ZBLAN fiber lasers.

In my thesis activity, it is proposed to use a Forward Time Centered Space (FTCS) method [51] and analytical methods for deep analysis and further understanding of Dy−doped ZBLAN fiber laser properties. In this way, a suitable and comprehensive model is obtained that figures out the impact of different physical parameters, such as pump and signal overlap integrals with the doped region, as well as cavity parameters (active fiber length and mirror's reflectivity), on laser output performance. On the other hand, the developed numerical method asses the impact of both ESA and amplified spontaneous emission (ASE) on the output power of the laser. Finally, the optimization criteria providing high slope efficiency (more than half of the Stokes limit) for yellow lasers, have been found. This in turn will pave the way for design, modeling, and employing the high slope efficiency Dy−doped ZBLAN fiber lasers in DR treatments. The modeling and simulation of the yellow-fiber laser will be represented in Chapter 4. Towards the final application of the yellow fiber lasers studied with numerical simulations, in Chapter 5, cell irradiation experiments are carried out, which obtain preliminary results. Finally, in Chapter 6, we conclude our research studies.

Chapter 1

Hollow-Core Fiber-Based Biosensors

1.1 HC Fibers

Nowadays, the demand for chemical and biological detection is gaining more and more attention. The main reason for that is the urgent need for bio/chemical detection in different areas of healthcare, defense, industrial, and pharmaceutical sectors. The unique properties of optical biosensors have turned them into good candidates to meet the needs of bio/chemical detection. One of the promising technologies in this category is fiber-based biosensors [21, 52]. In recent years, particularly inhibited coupling (IC) hollow-core (HC) photonic crystal fibers (PCFs) [25, 27, 53] with the advantage of an increased surface-to-volume ratio of interaction between the light and bio/chemical analytes, have been under research studies. The HCPCFs can confine the electromagnetic (EM) field inside an air core surrounded by a microstructured cladding. In this thesis, we focus on the capabilities of two different kinds of HC-fiber as high-sensitive biosensors. Their capabilities have been demonstrated through the chemical process of bio/analyte immobilization and monitoring the output spectra of the fiber. There are two main types of HC-PCFs named Tube Lattice (TL) and Kagome Lattice (KL) recently proposed for bioanalyte detection [27, 54]. One of the

promising technologies in this category is fiber-based biosensors [21, 52]. In recent years, particularly inhibited coupling (IC) hollow-core (HC) photonic crystal fibers (PCFs) [25, 27, 53] with the advantage of an increased surface-to-volume ratio of interaction between the light and bio/chemical analytes, have been under research studies. The HCPCFs can confine the electromagnetic (EM) field inside an air core surrounded by a microstructured cladding. In this thesis, we focus on the capabilities of two different kinds of HC fiber as highly sensitive biosensors. Their capabilities have been demonstrated through the chemical process of bio/analyte immobilization and monitoring the output spectra of the fiber. There are two main types of HC-PCFs named Tube Lattice (TL) and Kagome Lattice (KL) recently proposed for bioanalyte detection [27, 54]. In this research, KL and TL fibers are studied as the biological sensor platforms. The transmission of these fibers shows successive high and low transmission areas. In other words, this behavior is due to the inhibition of the coupling between the EM core modes and cladding modes.

1.1.1 Working Principle

The biosensors proposed here are based on HC-TLFs and HC-KLFs. The chosen biosensors based on a piece of HC-TLF with a length L are shown in Figure 2.7a. The fiber cross-section is schematically shown in Figure 2.7b. The fiber has a hollow core with radius R_{co}, surrounded by eight silica tubes with thickness t, radius r_t, and refractive index n_d. The waveguiding mechanism of the HC-TLFs is based on the interaction between the core modes (CMs) confined in the HC and the cladding modes (CLMs) confined inside the silica tubes [26]. According to the coupled-mode theory, power exchanging or coupling between the modes depends on the phase-matching and the amount of overlap integral between the modes [25]. In ICFs, the latter strongly depends on the transverse spatial oscillations of the CLMs. CLMs with slow spatial oscillations give high overlap integral with CMs and make them highly lossy. CLMs with quick spatial oscillations are weakly coupled with CMs which exhibit low loss. The phase-matching condition with slow oscillating CLMs occurs at the spectral regions corresponding to wavelength close to:

$$\lambda_m = \frac{2t}{m}\sqrt{n_d^2 - 1} \tag{1.1}$$

being m and integer number. Conversely, weak coupling with quickly varying CLMs corresponds to:

$$\lambda_{m+1/2} = \frac{2t}{m+1/2}\sqrt{n_d^2 - 1}. \tag{1.2}$$

Once the phase-matching condition between the modes is met ($n_{eff-co} = n_{eff-cl}$) and the overlap integral on the fiber-cross section is high, the strong coupling between the modes will result in the high-loss regions in the output spectrum of the fiber. On the other hand, once the coupling conditions are not met, there is no power exchange between the modes which will emerge as the low-loss region in the output spectrum of the fiber.

Therefore, the spectrum of transmissivity is defined as:

$$T = \frac{P_{out}}{P_{in}} \tag{1.3}$$

with P_{out} and P_{in} being the output and input power of the fiber, which is characterized by a succession of high and low transmission regions located, respectively, at $\lambda_{m+1/2}$ and λ_m. Figure 1.2 shows an example of T spectrum.

The working mechanism of sensing here discussed is based on the dependence of those wavelengths on the tube thickness t. This is different from PC-fiber-based biosensors based on the interaction between the core modes and analytes [24]. In the HC-TLF-based biosensor examined here, the creation of the bio-layers with a thickness of the t_{bi} on the tube surfaces (Figure 2.7c), will increase the total tube thickness causing a red-shift of the fiber transmissivity spectrum (see Figure 1.2). The spectral sensitivity (S) of the high transmissivity band edges can be expressed as:

$$S_{\lambda,t_{bi}} = \frac{d\lambda}{t_{bi}}, \tag{1.4}$$

where $d\lambda$ is the spectral wavelength shift and $t_{bi} = dt/2$ is half of the tube thickness variation. It is worth mentioning that, unlike the other PC-fiber-based biosensors,

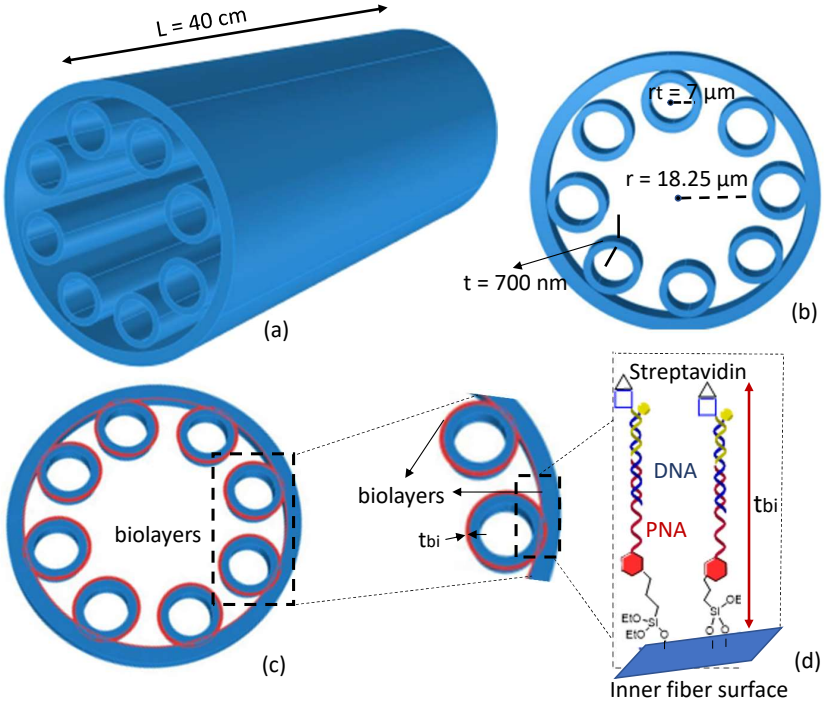

Figure 1.1: Schematics of (**a**) HCTLF-based biosensor with L = 40 cm, (**b**) fiber cross-section view with structural parameters, (**c**) Sensing mechanism and formation of the bio-layers inside the fiber surfaces, and (**d**) details about the formation of the bio-layers, bioreceptors, and streptavidin analytes.

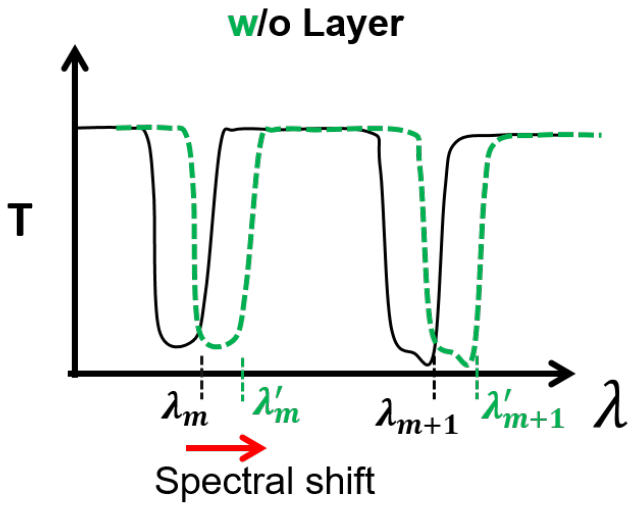

Figure 1.2: The sketched T spectrum shift due to the bio-layer binding of the inner surface of the fiber. The presence or absence of bio-layer has been shown, respectively, with W (green) and without O (black).

the spectral red-shift and, consequently, the sensitivity of this biosensor is not due to the guided mode effective refractive index changes. The formed bio-layer in the proposed biosensor here does not affect the effective refractive indices of the core modes and just affects the cladding mode parameters. More theoretical details about the estimation of this spectral shift can be found in [25]. The process of bio-layers formation on the internal surfaces of the fiber includes five steps, described in detail in the next section, and contains the bindings among the PNA, DNA, streptavidin molecules, and other chemical components used in the chemical functionalization of the HC-TLF. A schematic of the resulting bio-layer is shown in Figure 2.7d.

1.2 Fuctionalization Process

To have a selective detection of DNA and streptavidin analytes using the proposed HC-TLF, a five-step functionalization process for binding peptide nucleic acid (PNA) probes to the inner surface was used. Once the fiber was prepared, DNA detection was performed by infiltration of the sample, followed by that of a second biotinylated PNA probe and then of a streptavidin solution. These processes are shown in Figure 1.3. In the first derivatization step, the HC-TLF is cleaned and activated with a strong acid solution (MeOH: HCl, 1:1), to remove eventual residues of organic compounds and to activate the silica surface; then, the fiber is infiltrated with a solution of (3-aminopropyl) triethoxysilane (APTES, 0.1 %) in absolute ethanol. This organofunctional alkoxysilane molecule allows us to have the silanization of the inner fiber surface and to have a positively charged layer, in specific the terminal amino groups that are protonated at neutral pH (Figure 1.3 a). In the second step as can be seen in Figure 1.3 b, we flow through the fiber a solution of succinic anhydride (0.25 M in N, N-dimethylformamide (DMF)) to obtain terminal acidic moiety attached to the fiber. In the third step, we follow the functionalization process with infiltration of the fiber with a solution of N, N'-diisopropyl carbodiimide (DIC), and N-hydroxysuccinimide (NHS) in DMF as a solvent (c = 0.25 M for both solutions). This is a crucial step because the reaction between these two reagents allows us to have an activated ester on the fiber surface available to react with the free amino group of the PNA solution, producing the corresponding amide bond. After this step, a solution of the PNA capture probe in DMF (30 μM concentration) in the presence of excess DIPEA (50 μM concentration) has flowed through the fiber to obtain the desired binding (Figure 1.3 c).

In the detection steps, the functionalization procedure was changed compared with [27] to optimize the DNA detection process and avoid unspecific binding, by infiltration with ethanolamine in TRIS base (0.3% ETA pH:9) solution (Figure 1.3d), to block the unreacted active sites. Using these derivatized fibers, the DNA sensing protocol was performed. The fiber was flowed with complementary DNA (5 μM concentration) in PBS as a buffer for the capture of the target DNA by the forma-

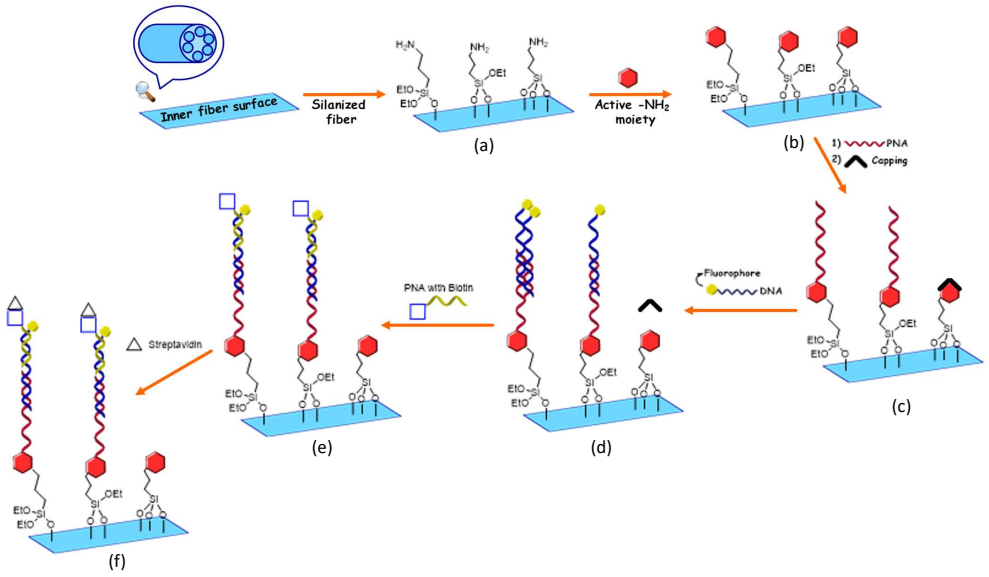

Figure 1.3: Derivatization scheme used for the HC-TLF: (**a**–**c**): derivatization; (**d**–**f**) DNA detection. (**a**) Silanization, (**b**) Reaction with succinic anhydride and activation of the terminal carboxylic moiety, (**c**) Coupling with the PNA through the terminal amino group, and blocking the unreacted active sites, (**d**) Infiltration of the HC-TLF with DNA complementary for the formation of the duplex PNA: DNA, (**e**) Flowing the biotinylated PNA signaling probe, and (**f**) infiltration of a streptavidin solution for signal magnification.

Table 1.1: Different summarized Oligo chemicals used in the chemical infiltration process.

Oligo	Name	Sequence
PNA	PNA Soy RR	N_{term} H-O-TGC TAG AGT CAG CTT-NH_2 C_{term}
DNA	50-mer SOY	5'- ACC CTA ATC ATT TCA TTT GGA GAG
	RR	GAC ACG CTG ACA AGC TGA CTC TAG CA -3'
Biotinylated PNA	PNA 8 mer-Biotin	N_{term} Biotin-O-TGG GAT TA-Gly-NH_2 C_{term}

tion of the stable duplex DNA: PNA (Figure 1.3d). Then, (Figure 1.3e) a solution of a second PNA functionalized with biotin (signaling probe) in DMF solution (30 μM concentration) was injected inside the fiber to label the DNA with biotin through non-covalent DNA: PNA interactions at the opposite end of the DNA. Finally, in the last step, infiltration of a solution including the streptavidin analytes (1 mg/ml concentration) has been performed (Figure 1.3f). To increase the thickness of the bio-layer for optical detection. The chemical properties of the PNA, DNA, and biotinylated PNA used in our experiments, are mentioned in Table 1.1.

The internal fluid-infiltration of the HC-TLF was performed by applying a nitrogen pressure of 2 atm to a polytetrafluoroethylene (PTFE) tubing reservoir (100 μL), connected to the terminal part of the fiber through a polyetheretherketone (PEEK) ferrule and a PTFE adapter. The flow of all the solutions through the fiber was confirmed by observing the drops of a liquid flow at the opposite end of the fiber. Furthermore, during the infiltration, the system was controlled regularly to ensure a right and precise infiltration. After each step in both the derivatization and sensing processes, the fiber has flowed with double distilled water and then emptied by flowing nitrogen. Finally, we performed the optical measurements on these empty fibers. During all the steps of derivatization and sensing processes, to avoid environmental errors and contaminations, fiber was kept fixed in the same position as much as possible. Furthermore, all the measurements were carried out in a clean room.

1.3 Optical Setup

The optical setup for employing HC-TLFs and HC-KLFs as the biosensor is depicted in Figure 2.8. As a light source, a supercontinuum white light source with diffraction-limited light in the wavelength range of 450-2400 nm was used. The alignment of the setup includes two main steps. In the first step, the output light of the laser is coupled to the 40 cm long HC-TLF through the appropriate lens with an appropriate focal length and a 3-axis NanoMax Flexure stage. This stage with micro-metric, precise, and continuous motions along the three-axis of X, Y, and Z enables us to couple input light into the HCTLF-input (left side of Figure 2.8). The chosen lens in the case of KL fiber is different. In the second step of setup alignment, the output light passed from an optical objective lens, is hit on a CCM1PBS252/M 30 mm Cage Cube-Mounted beam splitter cube, applicable in the wavelength range of 620-1000 nm (middle of the Figure 2.8). One beam is guided to an ultra-compact, lightweight Zelux Camera with a visible range of wavelengths connected to a laptop for real-time monitoring of the output beam. The second beam after passing the final objective is sent to an optical spectrum analyzer (OSA) (AQ-6315A/-6315B) with a resolution bandwidth of 0.5 nm to measure the output transmission spectrum in the wavelength range of 350-1750 nm. Both the schematic and real stage of the optical setup have been shown in Figure 2.8. As can be seen in Figure 2.8 (top), another advantage of this sensor is that it does not require a coherent source of light.

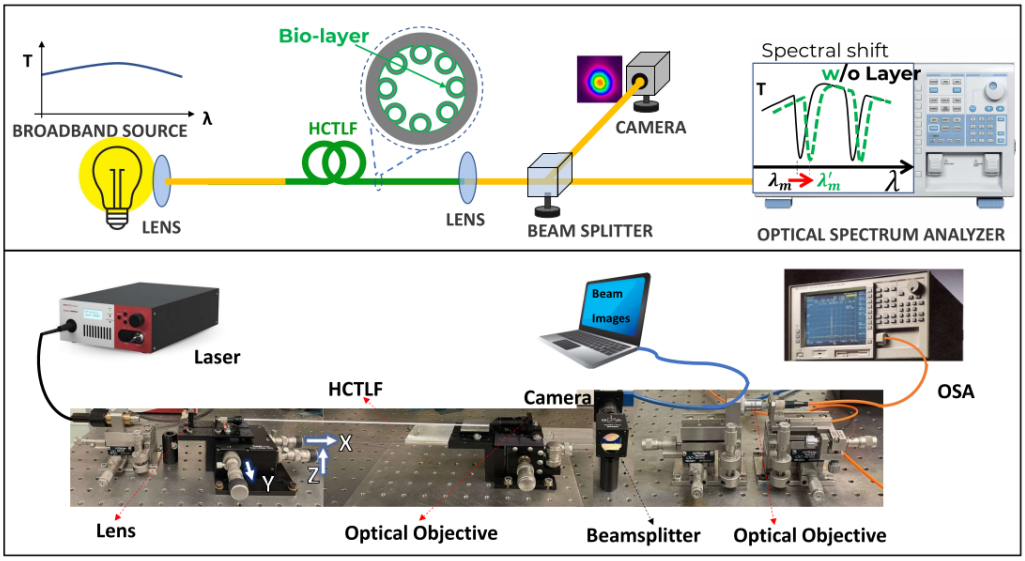

Figure 1.4: (**Top**) The schematic setup of the experiment includes a broadband coherent or incoherent source of light coupled at one end of the fiber. The transmitted light is collected in the output end of the fiber and finally, its spectrum is analyzed. The presence or absence of a spectral shift corresponds to the presence or absence of the DNA sequence searched for which have been shown, respectively, with (W) and without(O) bio-layer, (**bottom**) Image of optical setup including the laser, systems of lenses, camera, mechanical stages (with the possibility of micrometric movements along the three axes of X, Y, and Z), for guiding the laser light beam, and OSA connected to the camera is employed for recording the spectrum

.

Chapter 2

HCF Experimental Results and Discussions

2.1 Tube-Lattice Fibre

Figure 2.1 shows the HC-TLF cross-section used in our experiments. The fiber has a core radius R_{co} = 18 μm and it is surrounded by eight silica tubes with a radius of r_t = 7 μm and thickness of t = 700 nm.

2.1.1 Optical Measurements

The transmission spectrum shown in Figure 2.1 is acquired by the OSA before infiltrating the biochemical solutions inside the fiber. The transmission spectrum includes three high-loss regions in the wavelength ranges of approximately 500-540 nm, 729-805 nm, and 1277-1645 nm. Precise monitoring of the spectrum shift is obtained by monitoring the wavelengths corresponding to the sharp transition from high and low T.

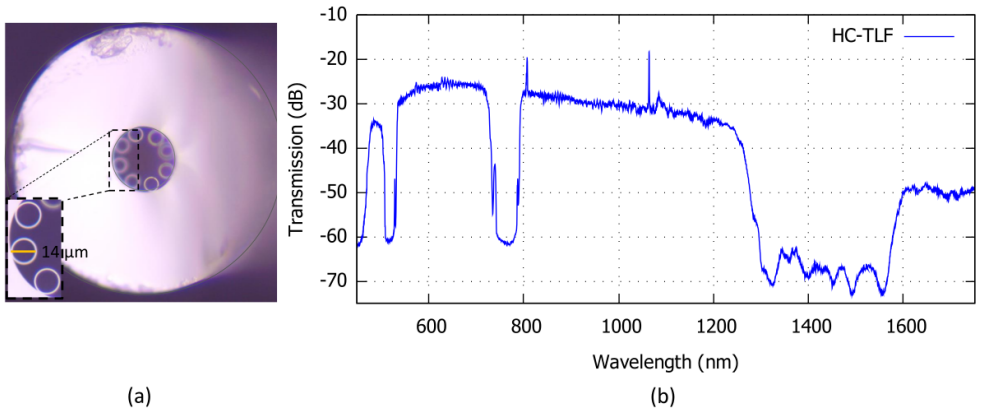

Figure 2.1: (**a**) Optical microscope image of HC-TLF cross-section (inset: magnification of the inner structure), (**b**) Transmission spectrum of the HC-TLF.

2.1.2 Field Images

After each step of the HCTLF infiltration, we obtained the near-field image of the EM field coupled into the fibers (stimulated as the linearly polarized LP01 and LP11 modes). We further have recorded the output spectra of the HCTLF-based biosensor. The Zelux camera images obtained respectively before infiltration, and after Aptes, PNA, DNA, PNA+Biotin, and streptavidin infiltration have been shown in Figure 2.2. As can be seen in this Figure, fundamental core modes are excited. It has been confirmed by the marginal octagonal patterns of the EM field inside the core region. EM field profile differences among the images are due to different alignment conditions in each step. Notice that in each step of infiltration, the fiber is launched in the pressure-flow system and then positioned in the optical setup for optical measurements. Therefore, new alignment conditions might be set. However, the sensing technique offered by the proposed HCTLF would be valid in case of higher-order modes (HOMs) excitation inside it [25]. This is one of the advantages of HCTLF-based biosensors compared with PC-based biosensors. It's worth mentioning that it is preferable to excite the fundamental mode, but preliminary studies reported in [25] show that the functioning of the sensor is not compromised even if the HHOMs are

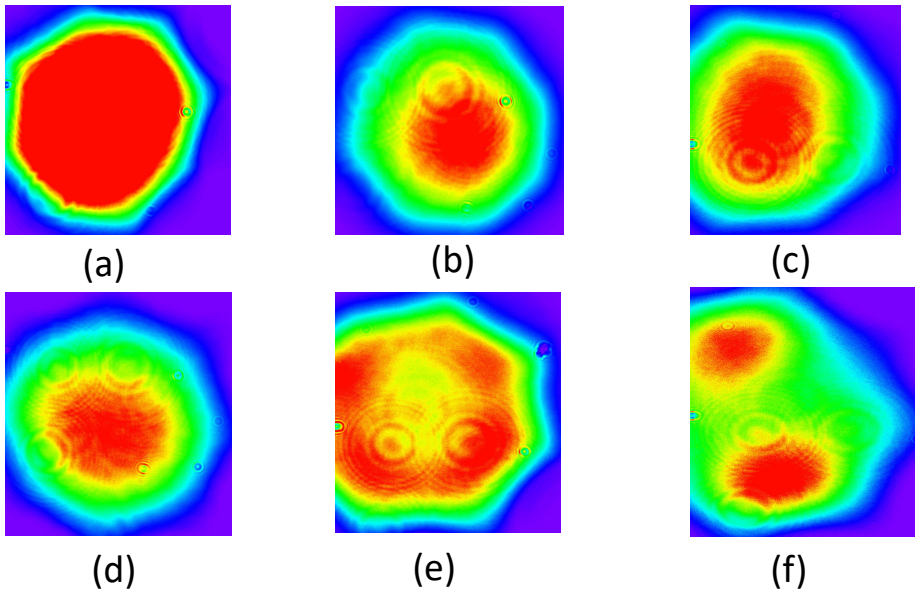

Figure 2.2: Near-field experimental profiles recorded at the 40 cm long HCTLF output (a) before infiltration, after infiltration with (b) Aptes, (c) PNA, (d) DNA, (e) PNA+Biotin, and (f) Streptavidin solution.

excited. Additionally, TLFs are multimode fibers. Though HOMs can be filtered out with a proper design of the tubes [26, 55], in this research, TLFs without HOMs suppression are considered. As mentioned in [25], HOMs are excited in case of imperfect coupling between source and fiber. In [25], the effect of multimode propagation due to imperfect fiber excitation on sensor performance was examined. Different inappropriate conditions of excitation including both wrong spot size and axis misalignment were analyzed. The obtained results showed that despite the alteration of the transmittance spectrum in case of inappropriate conditions, the red shift due to bio-layer is still clear and well-separated. This robustness is because the high-loss regions of HOMs are also governed by Eq. 1.1.

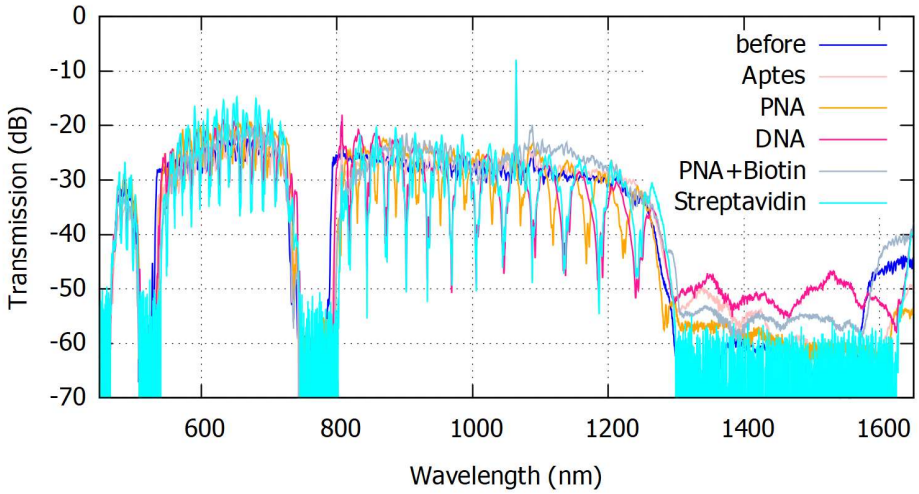

Figure 2.3: Experimental transmission spectra of HCTLF before infiltration, and after infiltration with Aptes, PNA, DNA, PNA+Biotin, and streptavidin solutions.

2.1.3 Output Spectra

The transmission spectra of the TLF-based biosensor have been depicted in Figures 2.3 and 2.4. The spectra of the modes shown in Figure 2.2 (a)-(f), corresponding to the respectively before fiber infiltration, and after Aptes, PNA, DNA, PNA + Biotin, and streptavidin fiber infiltration have been shown in Figure 2.3. Every time for further verification of the spectral positions, the measurements have been repeated at least three times. As can be seen in Figure 2.4, the spectral positions of the loss regions have been changed. In other words, a wavelength red-shift of 1.69 nm in the first loss region, can be measured between the output spectra before and after infiltration of the streptavidin analyte molecules. This shift demonstrates the detection of the formed DNA molecules. The shifts are further increased into respectively 9.88 nm (4.73 nm), and 45.3 nm at longer wavelengths related to the respectively, second and third loss regions. In the case of the second loss region, redshifts in both the back and forward edges have been mentioned (see Figure 2.4).

To test the reliability of the results, we have repeated all the processes of chemical

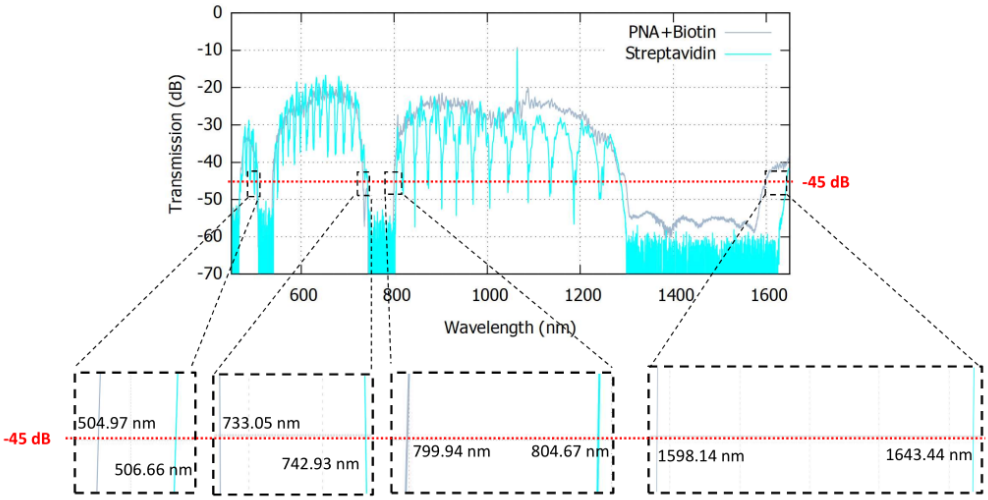

Figure 2.4: Experimental transmission spectra of HCTLF infiltrated with PNA+Biotin, and streptavidin solutions, insets show the zoomed images of the high loss regions at the reference level of -45 dB.

functionalization and optical measurements of the HCTLF-based biosensor. In this case, we also measured a wavelength red shift in the first, second, and third loss regions. For each step of fiber functionalization, we repeated the optical measurements three times and we calculated the average amount of the wavelengths and shifts. In this case, figure 2.5 compares the transmission spectra before (biotinylated PNA) and after (streptavidin) bio-layer binding (steps e and f in Figure 1.3, respectively). To test the reliability of the results, the process has been repeated three times, as shown by (1), (2), and (3) in Figure 2.5. A red-shift of the transitions in the first, second, and third regions is observed. As it can be seen in Figure 2.5, the wavelength shifts range from 1.83 nm to 3.81 nm for the front, from 2.84 nm to 5.76 nm, and from 9.82 nm to 17.92 nm, are measured at a reference signal level of -35 dB, respectively, in the first, second, and third loss regions.

Furthermore, at other reference signal levels (from -35 dB to -50 dB), the average wavelength shift between the graphs can be observed and measured. In Figure 2.6, the wavelength shifts between the transmission spectra of the fiber before

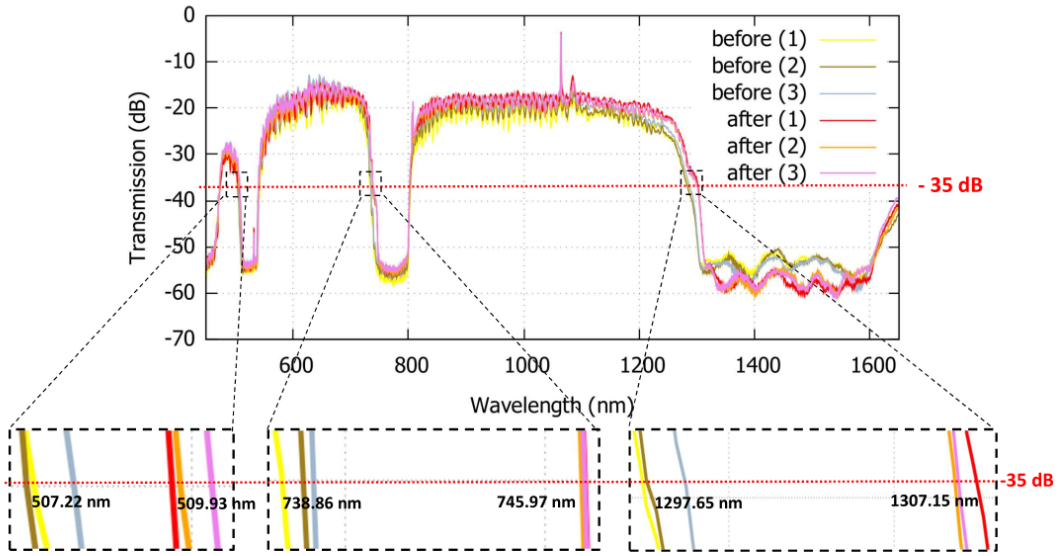

Figure 2.5: Transmission spectra of HC-TLF before and after infiltration with streptavidin solution, insets show the zoomed images of the high loss regions at the reference level of -35 dB. For both the before and after infiltration, optical measurements were repeated three times, shown by 1, 2, and 3.

and after infiltration of the solution containing the streptavidin molecules, are measured. These values have been measured at, respectively, three different wavelengths of 505 nm, 735 nm, and 1290 nm. The obtained results are comparable with the reported values in other works [19, 56], where detection of Biotin-Streptavidin binding layers is performed. As the final remark, it has been mentioned that the measured red-shifts which can be referred to as the detection of DNA and streptavidin molecules are comparable to the size of the protein molecules. It is worth mentioning that the protein molecules detected here have a refractive index of 1.45 RIU. However, the proposed biosensor can be applied for the detection of molecules such as breast cancer molecules with an RI of 1.401 [57]. In this case, another functionalization process will need to be taken. Furthermore, the red-wavelength shift observed in three wavelength bandwidths shows the flexibility of the proposed biosensor alongside usages of different light sources. Since the shift observed in the case of the second and third bands was significant (5.76 and 17.92 nm, respectively), according to the 3-sigma criterion, though we did not perform a calibration curve to determine the limit of detection (LOD), we can state that the LOD should be lower than the concentration used in the test (5 μM). It's worth mentioning that LOD is taken as the lowest concentration of an analyte in a sample that can be detected. LOD can be calculated as $\frac{3.3\times\sigma}{S}$, where σ is the standard deviation of the response and S is the sensitivity of the biosensor or slope of the calibration curve [58]. Here, in this thesis, we have described the first demonstration of the changes in HC-TLF fiber upon DNA capture and subsequent decoration with streptavidin through a PNA-signalling probe. The work aimed to show that the derivatization of the surface with PNA capture probes is feasible and that an appropriate sensing format can be used to generate an optical signal detectable in the fiber transmission spectrum. The method was found to be reproducible and can subsequently be extended to quantitative measurements. Indeed we envisage that the method can be used for quantitative measurement of the DNA content, since a different concentration of DNA will lead to a different degree of 'capture' of the target DNA and, therefore, to the capture of streptavidin to a different extent, leading to a different shift, as previously observed with a similar format on Bragg-grated PCF using gold nanoparticles as enhancers [59].

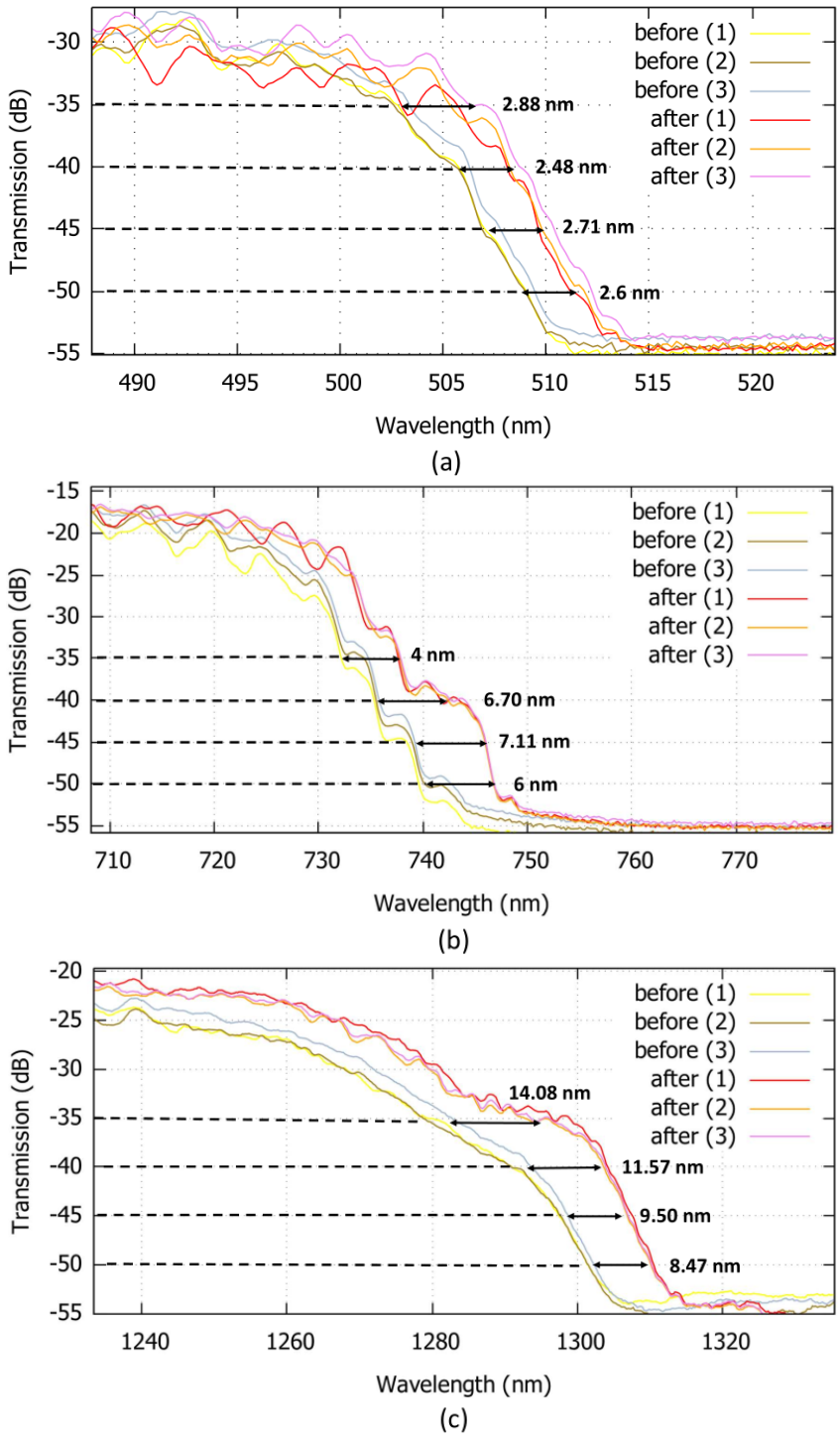

Figure 2.6: Zoomed images of the high loss regions at the reference level of -35 dB, -40 dB, -45 dB, and -50 dB, in different wavelength ranges of (**a**) 500-520 nm, (**b**) 720-750 nm, and (**c**) 1290-1320 nm. The results related to the first (1), second (2), and third (3) measurements before and after streptavidin solution infiltration, are observable.

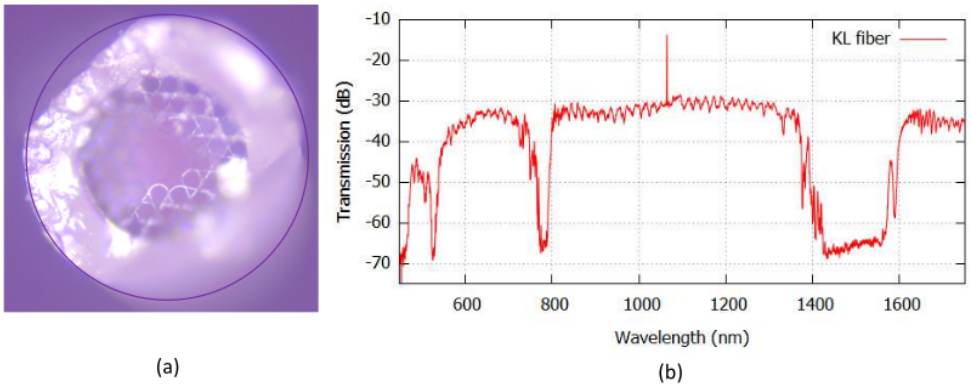

Figure 2.7: (a) Cross-section geometry of the KL fiber acquired by a 40x optical microscope. (b) Transmission spectra of the fiber recorded by OSA.

2.2 Kagome-Lattice Fibre

The KL-HCMOF fiber structure, investigated here includes a piece 40 cm long with an air core of 60 μm surrounded by the silica struts. There is a specific waveguide mechanism of light in this fiber which is based on inhibited coupling between the core modes and cladding modes.

2.2.1 Optical Measurements

In Fig. 2.7 (a), an optical microscope image of the KL fiber has been shown. The relatively large size of the air core will cause the creation of other high-order LP-like modes. However, we have carried out our experiments by selecting the LP-like core modes. We tried to find the best condition of the setup alignment for the excitation of the LP-like core modes. The transmission spectrum of this fiber recorded by an optical spectrum analyzer (OSA) used in our experiments has been shown in Fig. 2.7 (b). As can be seen, it includes three central low-transmission regions. The positions of the slop fronts of these regions are the places that highly depend on the interaction between the core and cladding modes.

2.2.2 Output Spectra and field images

After having formed the bio-layers on the internal surface of the KL-HC fiber, the output spectra and experimental EM field images of the LP sensing modes are recorded. It is worth mentioning that rinsing and drying the internal surfaces of the fiber is an important step before optical measurements. For performing the optical measurements the fiber is placed in the related optical setup. In this setup, as a light source, a super-continuum white light source in the wavelength range of 450-2400 nm, has been used. The light leaving the end-side of the fiber is hit on the lateral side of a beam splitter. Here, half of the light is guided to the OSA and another half to the Zelux camera. Both the OSA and camera are connected to a laptop in order to record the output spectra and near-field images of the LP-like modes. In Fig. 2.8 (a) and (b), the image of the coupled field inside the fiber and the corresponding transmission spectra are shown. As can be seen in Fig. 2.8 (a), an LP-like core mode is excited. It has been confirmed by the marginal octagonal patterns of the EM field inside the core region. Both the images in Fig. 2.8, have been acquired after the fiber infiltration process which demonstrates the fiber persistence, reliability, and its potential as a label-free bio/chemical sensor.

As can be seen in Fig. 2.8 (b), there are a few nanometres redshifts in the high transmission band of the output spectrum. The first redshift observed in the rising edge of the central high transmission band is measured to be 5 nm around the wavelength of 800 nm. The second red shift observed in the falling edge of the same wavelength band is measured to be 9 nm around the wavelength of 1400 nm. These wavelength shifts have been measured at a signal level of -50 dB. However, at different signal levels, the redshifts can be measured. To be sure that these shifts are not coming from other reasons, like changes in the fiber-alignment setup, the measurements have been repeated several times. The detected redshift for every measurement proves the feasibility of using the KL-HC fiber as a sensor platform. Furthermore, regarding these shifts, the values are consistent with the typical dimension of the analytes here examined, i.e. streptavidin molecules.

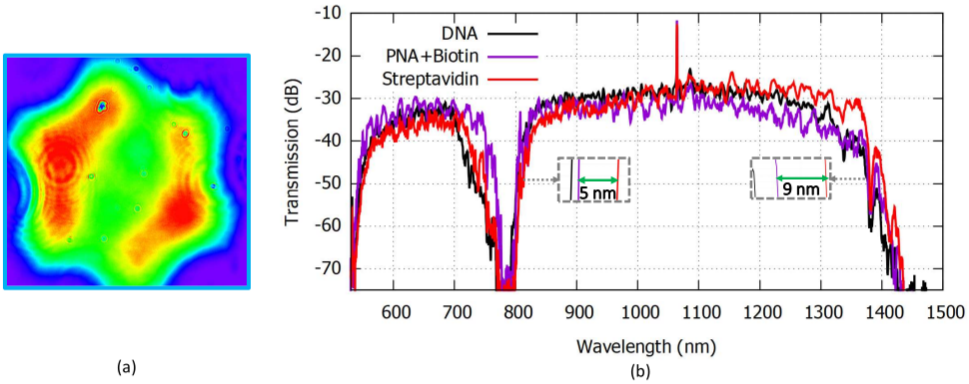

Figure 2.8: (a) Field intensity image of the coupled field into the fiber (acquired by the Zelux camera), exciting a quasi-LP11 mode, (b) transmission spectra of the fiber after infiltration, a red-shift of a few nanometers between PNA+Biotin and Streptavidin spectra are measured.

Chapter 3

Fiber Amplifiers and Lasers

3.1 Fibre lasers

The concept of amplification of radiation through stimulated emission with coherency was introduced in 1917 by Albert Einstein [60]. After that, on May 16, 1960, the first working laser, which was a ruby one was demonstrated by Theodore Maiman [61]. The fiber lasers were proposed and developed [62]. Silica fibers were among the first fibers introduced as the gain medium for the laser [63]. Soon after, the first working silica fiber laser [64] was demonstrated. Since then, many experimental and theoretical results on silica- and fluoride-doped fiber amplifiers and lasers with various rare-earth dopants have been reported. Fiber lasers are low-cost and relatively easy to produce sources of excellent beam quality, emitting light in different parts of the electromagnetic spectrum including infrared, visible, and ultraviolet ranges. For this reason, fiber amplifiers and lasers have evolved to be some of the most successful technologies in different areas of photonics. They are appropriate candidates for applications in telecommunication, medicine, manufacturing industry, and metrology. Different kinds of fiber lasers including continuous wave, pulsed, narrow-linewidth, single frequency, tuneable, and high-power sources have been developed to meet the increasing demands of various industries. Simply, fiber laser structure includes a gain medium made of an optical fiber doped with rare-earth ions and a feedback mech-

anism. The feedback mechanism is provided by a resonant cavity formed by either physical mirrors or the frequency selective fiber Bragg grating (FBG), written into the core of the fiber [51].

3.2 Visible lasers

During the last few years, visible light sources emitting around 400–700 nm have attracted the scientific community's attention, since they are extensively employed in different domains such as metrology, medicine, optical storage, and laser guide star systems [65, 40, 37, 66]. For visible laser generation, there are several techniques shown in Figure 3.1. Although gas lasers and dye lasers have often been used in scientific research, they suffer from delicate operation and high maintenance [30]. Nowadays due to the progress in nonlinear optics, second harmonic generation (SHG), or optical parametric oscillator (OPO) techniques are interesting alternatives for visible laser development. However, these techniques have some disadvantages such as low efficiency, complexity, reliability issues, and high costs. On the other hand, for visible solid-state lasers, there is the problem of the lack of good excitation sources. It is worth mentioning that visible semiconductor lasers are well developed to use, but their operating power has still some limitations [30]. Generally speaking, it must be underlined that the design of a compact visible laser is very challenging because there are no direct diode or solid-state sources available.

In my research activity, we deal with visible lasers particularly in the yellow range of EM spectrum, based on specialty active fiber technology. These fiber sources compared with the previously mentioned technologies for visible laser developments, have less complex optical arrangements and better wall-plug efficiencies.

3.2.1 Yellow-fibre laser

In the second part of my Ph.D. course, we particularly focus on developing a compact and efficient yellow fiber-based laser system for ophthalmologic surgery, in particular, for the treatment of Diabetic Retinopathy (DR), which affects about one-third of the diabetic population according to the META-EYE Study [67]. Because of the

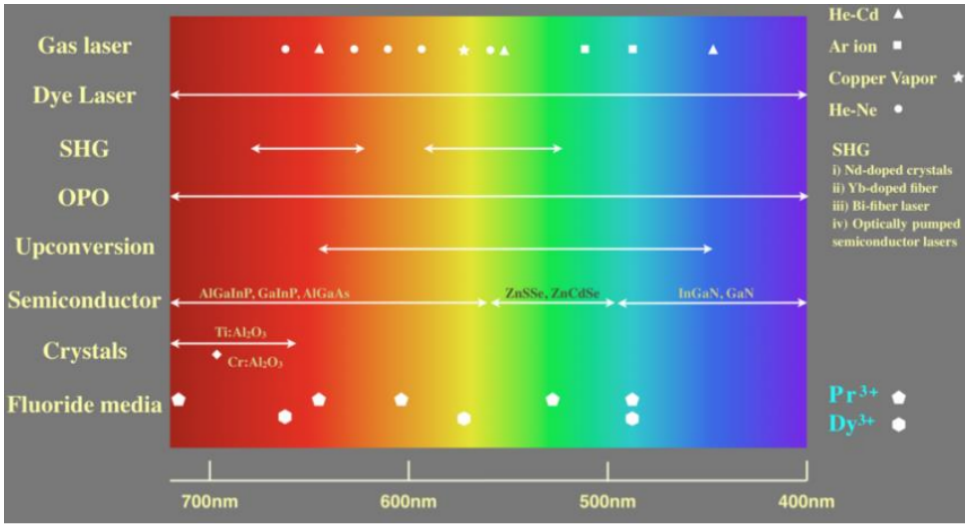

Figure 3.1: Different techniques for visible laser generation [30].

good combination of the absorption values of the main tissue components at this wavelength (see Figure 3.2), yellow emitting lasers (565–590 nm) are well suited for medical treatments in ophthalmology and dermatology. In particular, yellow light at 577 nm is considered to be the best choice for the macular retinopathy treatment by photocoagulation since the lower absorption by the retinal and foveal pigments is compensated by the higher absorption of oxyhemoglobin and the lower scattering by the eye tissue, allowing central macular edema treatments free of foveal damages. Originally green lasers (532 nm) were used but switching to yellow lasers has paved the way for new treatments for these frail retinal areas. Experimental investigations on animals and humans, but also numerical analyses, have confirmed that yellow light is the most suitable candidate for retinopathies because it is effective with lower power, preventing thermal damage to neighboring areas [35].

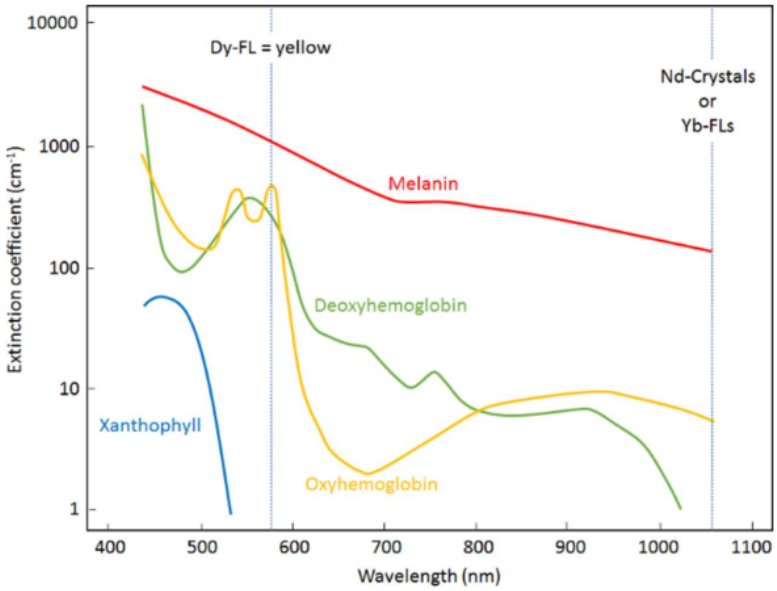

Figure 3.2: Laser wavelength and effective light absorption.

3.3 Dysprosium-doped Yellow-fibre laser

Access to yellow emission has been possible with several developed techniques with copper bromide laser [38], upconversion [68], or second harmonic generation in Nd-doped crystals [29], Yb-doped fibers[39], bi-fiber lasers [40], optically pumped semiconductor lasers [41]. However, these techniques demand bulky structures with several free-space alignments, high maintenance, and tight limitations on the pump conditions. For accessing high-efficiency and simple direct yellow laser emission, the trivalent dysprosium ion (Dy^{3+}) is a very attractive candidate. There is a strong yellow fluorescence coming from $^4F_{9/2}$ to $^6H_{13/2}$ transition in the spectral band of Dy^{3+} ion. In [42], J. Limpert et al. demonstrated the first CW yellow emission in a $Dy-$doped ZBLAN fiber laser by using a bulky air-cooled Argon-ion laser emitting at 457 nm as a pump source. Then in 2011, a low-loss $Dy-$doped optical fiber (0.3 dB/m at 532 nm) made of a fluoro-aluminate glass was used to demonstrate yellow laser oscillation [30]. In that work, the $Dy-$doped fluoride fiber was pumped by a

398.8 nm GaN laser diode, and the maximum output power was 10.3 mW [30]. In the following years, yellow lasers, from Dy−doped yttrium aluminum garnet with 12% slope efficiency and Dy^{3+}–Tb^{3+} co-doped $LiLuF_4$ crystal with 13.2 % slope efficiency have also been reported [43, 44]. Nevertheless, in a considerable period, due to the lack of high-performance gain fibers and high-power GaN blue lasers as the pumping sources, no significant research progress has been observed in Dy−doped fiber yellow lasers. Then, in 2020, thanks to the breakthroughs of both Dy−doped fluoride fiber fabrication technology and high-power blue GaN laser diodes (LD), emitting at 445 nm, the first GaN laser diode pumped Dy−doped ZBLAN fiber laser for yellow emission was reported using a simple setup [45]. In that experiment, a commercially available Dy−doped ZBLAN fiber, originally designed for mid-infrared emission was used. Furthermore, the performance of the yellow laser system was investigated by using two different Dy−doped fiber lengths (0.6 m and 5.95 m). Authors of [45] obtained the maximum laser slope efficiency of 2.3% and 0.9% for absorbed pump power respectively for 0.6 m and 5.95 m of Dy−doped fiber. One year later, in 2021, the same research group investigated the potential causes of the low experimental slope efficiency and they found contributions from the background loss of the fiber and excited-state absorption (ESA) of the intracavity yellow light [46]. They demonstrated a detailed experimental and theoretical analysis of the $^4F_{9/2}$ to $^6H_{13/2}$ lasing transition of a Dy−doped ZBLAN fiber and measured a yellow laser output generated with a maximum slope efficiency of 33%, which is less than half of the Stokes limit ($\sim$ 78%) [46]. Although these new researches were so important in the field of Dy−doped yellow fiber sources, the laser output powers were still limited to the mW levels. The possible causes of this challenge are difficulties in the manufacture of Dy^{3+} fluoride fibers with low loss and high gain; the commercially available high-power GaN blue laser sources with high beam quality are scarce; the construction of yellow fiber laser cavity with high efficiency and simple structure is relatively difficult. This challenge has been overcome in [50], by reporting a Watt-level yellow Dy− doped ZBLAN fiber laser by using optimized cavity designs. The suggested yellow fiber laser in [50] simply consisted of a Dy−doped ZBLAN fiber as the gain medium, a fiber end-facet mirror with high reflectivity at the yellow wave-

length, and a 450-nm diode laser as the pump source. The yellow Dy−doped ZBLAN fiber laser was realized with a maximum output power of 1.12 W at 575 nm, which was achieved at a pump power of 4.20 W.

It is worth mentioning that most of these works were dedicated to experimental activities. Developing trustworthy numerical models is of great importance to understand, analyze, and predict the potential improvement of this fiber laser system. Therefore, in this part of my research, we develop the analytical and numerical methods for a comprehensive analysis of the Dy−doped yellow fiber laser. As mentioned earlier, the yellow emission (i.e.$\sim$ 565-590 nm) can be obtained by considering the ${}^4F_{9/2} \rightarrow {}^6H_{13/2}$ energy transition in Dy−doped fiber. As shown in Figure 3.3, for the yellow lasing transition and excitation of the electrons from the ground-state population to the upper yellow lasing level (${}^4F_{9/2}$), several shorter wavelengths ranging from the ultraviolet to the blue spectral range can be used. In the next sections, I discuss in more detail the energy levels involved in pumping and lasing of the laser.

3.4 Rare earth−doped fibre amplifiers and lasers

As it is well known, rare earth ions have a long history in optical and magnetic applications. Generally speaking, rare-earth elements are classified into two groups, namely lanthanides, with atomic numbers ranging from 57 to 71, and actinides, with atomic numbers ranging from 83 to 103. In solid-state laser technology, lanthanides are more important than actinides, because they have interesting optical properties that distinguish them from other optically active ions. Some of these characteristics are: emission and absorption over narrow wavelength ranges, wavelengths of the emission and absorption transitions relatively insensitive to host material, weak intensities of these transitions, long lifetimes of meta-stable states, quantum efficiencies that tend to be high, except in aqueous solutions [69]. These characteristics are all due to the nature of the states involved in these processes and lead to the excellent performance of rare earth ions in many optical applications such as lasers and amplifiers. These devices that provide gain must have low scattering losses, and one is restricted to using single-crystal or glass hosts. Nowadays, many doped fiber lasers

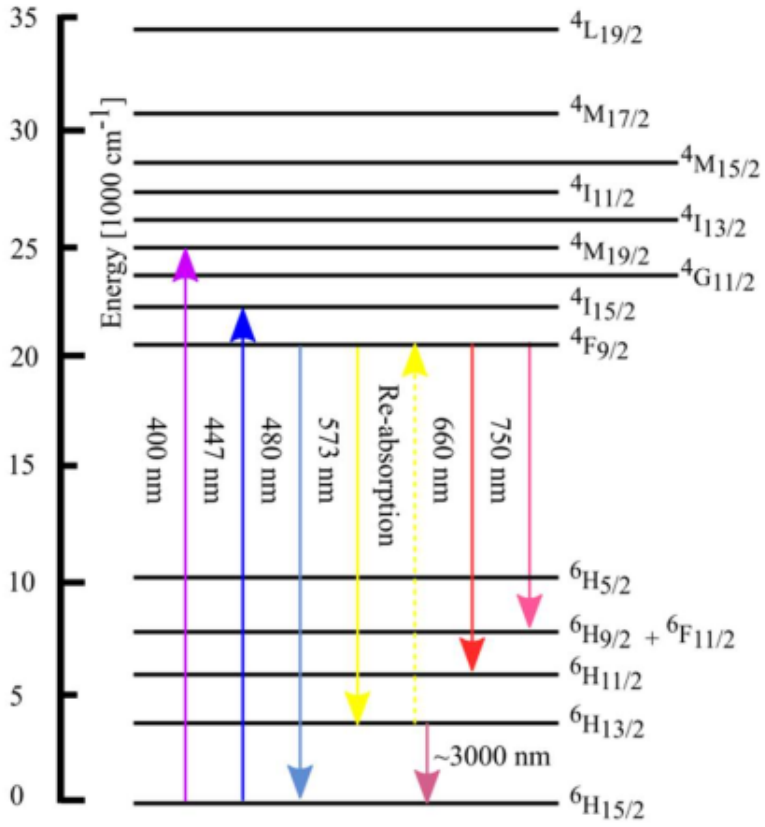

Figure 3.3: Energy-level schematic diagram of Dy^{3+} in ZBLAN glass [46]. The ground-state absorption (GSA) for $\sim$ 400 nm and $\sim$ 447 nm have been shown with upward arrows. Two lasing levels, $^4F_{9/2}$ and $^6H_{13/2}$, generate emission in the visible, near-infrared, and mid-infrared (mid-IR) regions in ZBLAN glass, shown by the downward arrows. In ZBLAN glass, the lifetime of the lower laser level ($^6H_{13/2}$) of the yellow laser transition is comparable to the upper laser level ($^4F_{9/2}$), meaning the yellow light is reabsorbed (as shown by the upward dashed line).

have been reported with lasing wavelengths from 550 nm to 2900 nm based on erbium (Er^{3+}), neodymium (Nd^{3+}), ytterbium (Yb^{3+}), holmium (Ho^{3+}), thulium (Tm^{3+}), praseodymium (Pr^{3+}), samarium (Sm^{3+}) [70, 69], and Dy^{3+} [30, 45]. The broadened linewidths of rare-earth ions in glass also enable wide tuning ranges [71] and are suitable for short-pulse mode locking [72].

3.4.1 Methods of Analysis

Developing fiber laser systems relying on just experimental work is inefficient and inadequate. Additionally, the current progress of fiber lasers and amplifiers requires accurate and simple theoretical or numerical modeling of the system. Several numerical models and analytical solutions exist that are based on different simplifying assumptions. Usually, analytical models produce solutions for the small-signal gain of three- and four-level fiber lasers [73, 74]. These approaches give a good insight into the physics of the system, but they require knowledge of fiber parameters that are difficult to measure, such as optical mode distributions, dopant-ion concentration and distribution within the fiber, emission, and absorption cross sections, and decay times [75]. Therefore the mentioned disadvantages should be considered in choosing the appropriate analytical methods. On the other hand, accurate models of a rare-earth-doped laser are obtainable with numerical methods. Choosing the suitable numerical model is advantageous because it provides not only an understanding of the system under investigation but also the possibility to conduct a wide range of experiments to optimize the device's design and foresee its limitations. In other words, using a good model helps to predict the behavior of the characteristics of the fiber laser without performing experiments, which can be difficult to carry out in laboratory conditions. Analysis and simulation of the fiber amplifier and laser systems require the solution of two groups of equations. The first group of equations is the rate equations of the active medium which describes the distributions of the population inversion. The second group of equations is the propagation equation consisting of several coupled non-linear first-order ordinary differential equations (ODE) which describe the propagation of the optical fields inside the cavity. For solving these equations, appropriate boundary conditions must be employed. It should be mentioned that the boundary

conditions depend on the working regime (continuous or pulsed) of the fiber laser. Finally, the resulting systems of equations are complex. Accordingly, finding the right solutions whether analytically or numerically might become impossible. Therefore, to avoid these possibilities, approximations and simplifications can be applied.

3.5 Four-level system of Dy−doped fibre

One of the simplification schemes in solving the equations is to reduce the number of energy levels involved. In the case of approximation of a 3-energy level system to a 2-energy level one, the lifetime of the uppermost energy level such as the $^4I_{11/2}$ manifold of Erbium, should be short [74]. It's worth mentioning that the most simple model of the matured system of the erbium-doped fiber amplifier is considered a pure three-level atomic system. In this way, most of the important characteristics of the amplifier can be interpreted. However, in some cases like the short cavity rare-earth-doped fiber lasers with a high concentration of rare-earth ions, the 2 and 3-energy level systems are not accurate models. In addition, there are other cases where more than three energy levels should be considered including thulium, neodymium, and dysprosium ions which cannot be described as a two-level system. For these ions, it's difficult to find analytical solutions for the equations, and one usually relies on numerical solutions. The system that we are dealing with is a four-level Dy−doped fiber laser. The energy levels of this rare earth ion are shown in Figure 3.3. For the yellow lasing transition and excitation of the electrons from the ground-state population to the upper yellow lasing level ($^4F_{9/2}$), several shorter wavelengths ranging from the ultraviolet to the blue spectral range can be used. Here in my study, I have considered the transitions and effects that are important for the efficiency of the system, shown in Figure 3.4.

As seen in Figure 3.4, a four-level system is considered with a ground state denoted by 0, the highest state labeled 3 (into which energy is pumped), and states 1 and 2 which are lower and upper lasing transition. The upper lasing level (level 2 in our system) often has a long lifetime in the case of efficient lasers and amplifiers. Hence, it is sometimes referred to as the meta-stable level. The populations of the levels are

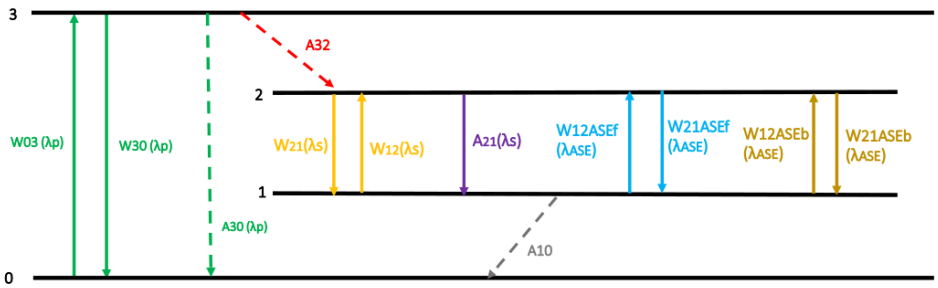

Figure 3.4: Simplified Energy-level schematic diagram of Dy^{3+}. The ground state is shown with 0, and upper levels accordingly are labeled with 1-3. The upper laser level, ${}^4F_{9/2}$ is named 2, and the lower laser level, ${}^6H_{13/2}$, is shown with 1.

labeled N_0, N_1, N_2, and N_3. This four-level system is intended to represent that part of the energy level structure of Dy−doped fiber amplifiers and lasers that is relevant to the yellow-light emission process. To obtain amplification, we need a population inversion between the involved states in the amplification or lasing process, which are states 1 and 2.

3.5.1 Rate equations

According to the electronic transition process of a four-level system of Dy^{3+} ions, shown schematically in Figure 3.4, the populations of different levels are expressed by the following rate equations

$$\frac{dN_0}{dt} = -W_{03}N_0 + (W_{30} + A_{30})N_3 + A_{10}N_1 \tag{3.1}$$

$$\frac{dN_1}{dt} = (W_{21} + A_{21} + W_{21f} + W_{21b})N_2 - A_{10}N_1 - (W_{12} + W_{12f} + W_{12b})N_1 \tag{3.2}$$

$$\frac{dN_2}{dt} = -(W_{21} + A_{21} + W_{21f} + W_{21b})N_2 + A_{32}N_3 + (W_{12} + A_{12} + W_{12f} + W_{12b})N_1 \tag{3.3}$$

$$\frac{dN_3}{dt} = W_{03}N_0 - (W_{30} + A_{30})N_3 + A_{32}N_3 \tag{3.4}$$

In a steady-state situation, the time derivatives will all be zero,

$$\frac{dN_0}{dt} = \frac{dN_1}{dt} = \frac{dN_2}{dt} = \frac{dN_3}{dt} = 0 \tag{3.5}$$

and the total population N_t is given by

$$N_t = N_0 + N_1 + N_2 + N_3 \tag{3.6}$$

Under these constraints and after algebraic manipulating of the system of equations 3.1–3.6, the population of levels can be written as

$$N_1 = \frac{ce - bf}{ae - bd} \tag{3.7}$$

$$N_2 = \frac{af - cd}{ae - bd} \tag{3.8}$$

where the coefficients of a, b, c, d, e, and f are respectively $(W_{12} + W_{12f} + W_{12b} + A_{10})$, $(W_{21} + A_{21} + W_{21f} + W_{21b})$, 0, $\frac{(W_{30}+A_{30}+A_{32}+W_{03})A_{10}}{W_{03}A_{32}}$ + 1, 1, and 1. Other population of N_0 and N_3 can be found by finding for N_1 (Equation 3.7), N_2 (Equation 3.8), with some algebraic calculations. Various coefficients used in the system of Equations 3.1–3.6 are defined in Table 3.1.

In Table 3.1, P represents the power (for the pump, signal, or amplified spontaneous emission), $\sigma_{12(21)}$ is the absorption (or emission) cross-section between energy levels 1 and 2 (2 and 1), h is the Planck constant and ν is the frequency of the radiation. ASE stands for amplified spontaneous emission, which considers the amplification rate for spontaneous emission of all wavelengths in the radiation spectrum. For defining the ASE phenomenon it is worth mentioning that all the excited ions in level number 2 can spontaneously decay from the upper state to the ground one by emitting a photon. The photon emitted in this process is uncorrelated with the signal photons and can be considered a source of noise. However, since the amplification can occur for these spontaneously emitted photons, they amplify and cause the emission

Table 3.1: **Coefficients used in the system of equations 3.1–3.4.**

Parameter	Definition	Relation
W_{03}	Pump absorption rate at λ_p	$\frac{\sigma_{03}P_p}{h\nu_p}$
W_{30}	Stimulated emission rate at λ_p	$\frac{\sigma_{30}P_p}{h\nu_p}$
A_{30}	Spontaneous emission rate from level 3	$\frac{1}{\tau_{03}}$
A_{10}	Spontaneous emission rate from level 1	$\frac{1}{\tau_{10}}$
W_{21}	Stimulated emission rate at λ_s	$\frac{\sigma_{21}P_s}{h\nu_s}$
A_{21}	Spontaneous emission rate from level 2	$\frac{1}{\tau_{21}}$
W_{21f}	Stimulated emission rate at λ_{ASEF}	ASETerm (λ_i, σ_{21})
W_{21b}	Stimulated emission rate at λ_{ASEb}	ASETerm (λ_i, σ_{21})
W_{12}	Absorption rate at λ_s	$\frac{\sigma_{12}P_s}{h\nu_s}$
W_{12f}	Absorption rate at λ_{ASEF}	ASETerm (λ_i, σ_{12})
W_{12b}	Absorption rate at λ_{ASEb}	ASETerm (λ_i, σ_{12})

of more photons from excited ions, as they travel along the fiber. This phenomenon, which can occur at any wavelength within the fluorescence spectrum of the amplifier or laser transitions, is called amplified spontaneous emission. In this parasitic process, released photons are amplified in both the forward ($+z$) and backward ($-z$) directions and generate two waves. ASE is an important source of noise and poor performance of rare-earth-doped fiber amplifiers and lasers. To compute the ASE power at the output of the fiber, first, we need to calculate the spontaneous emission power at a given point in the fiber. This power is sometimes referred to as an equivalent noise power [76]. For a single mode fiber with two independent polarizations for a given mode at frequency ν, the noise power in a bandwidth $\Delta\nu$, corresponding to spontaneous emission, is equal to ASETerm = 2 $h\nu\Delta\nu$. The total ASE power at point z along the fiber is the sum of the ASE power from the previous sections of the fiber and the added local noise power. Calculation of this parameter would require the equations of quantum electrodynamics which will not be presented here. Thus for the system of equations here considered, the final expression for ASE calculation is expressed as ASEterm. ASETerm is given by the function of $\frac{2\Delta\lambda\Gamma_s\sigma_{12(21)}hc^2}{\lambda_i^3}N_t$.

3.5.2 Power propagation equations

The power propagation equations describe the evolution of the pump, signal or laser radiation, and amplified spontaneous emission along the active fiber. For a systematic formulation, the wavelength spectrum is divided into slots, and in each slot the evolution of these quantities along the z direction is determined by a set of coupled first-order differential equations [76] as follows:

$$\frac{dP_p}{dz} = -\Gamma_p \sigma_{03} N_0 P_p + \Gamma_p \sigma_{30} N_3 P_{0p} - \alpha P_p \tag{3.9}$$

$$\frac{dP_s}{dz} = -\Gamma_s \sigma_{12} N_1 P_s + \Gamma_s \sigma_{21} N_2 P_s - \alpha P_s + ASETerm(\lambda_s)\frac{N_2}{N_t} \tag{3.10}$$

$$\frac{dp_{ASEF}}{dz} = -\Gamma_s \sigma_{12} N_1 P_{ASEF} + \Gamma_s \sigma_{21} N_2 P_{ASEF} - \alpha P_{ASEF} + ASETerm(\lambda_{ASEF})\frac{N_2}{N_t} \tag{3.11}$$

$$\frac{dp_{ASEB}}{dz} = -\Gamma_s \sigma_{12} N_1 P_{ASEB} + \Gamma_s \sigma_{21} N_2 P_{ASEB} - \alpha P_{ASEB} + ASETerm(\lambda_{ASEB})\frac{N_2}{N_t} \tag{3.12}$$

where Γ_p and Γ_s represent the overlap integrals between pump radiation and active-ion distribution, signal light, and active-ion distribution respectively. If we assume that the dysprosium ions are uniformly distributed in a disk of radius b concentric to the core of radius a, then the overlap integrals of pump and signal can be defined as [77]

$$\Gamma_{p(s)} = \int_0^{2\pi} \int_0^b i_{p(s)}(r,\phi) r dr d\phi \tag{3.13}$$

where $i_{p(s)}$ represents the normalized optical intensity at pump (signal) wavelengths and is expressed as:

$$i_{p(s)} = \frac{I_{p(s)}(r,\phi,z)}{P_{p(s)}(z)} \tag{3.14}$$

where I_p is the intensity of the pump beam with frequency $\nu_p = \frac{c}{\lambda_p}$. The intensity I_s of the transverse field corresponds to the magnitude of the Poynting vector of the fundamental mode of the fiber at wavelength λ_s. The optical power of the beam traveling for a length z along the fiber will thus be:

$$P_s(z) = \int_0^{2\pi} \int_0^{\infty} I_s(r, \phi, z) r dr d\phi \tag{3.15}$$

It's worth mentioning that if we consider non-uniform dopant distributions of ions, we need to change how to calculate the overlap integral with the mode field distribution. In this case, the overlap integrals could be calculated by using the COMSOL software which provides us with the spatial distribution of the electric or magnetic field vector, to calculate the overlap with a more complex dopant distribution. However, at the moment, the Dy-doped fiber used in most of the papers on yellow fiber lasers is the one made by Le Verre Fluoré (France) [46], which has a uniform dopant distribution in the core.

3.6 Solving methods

Equations 3.9–3.12 are completed by the boundary conditions. In the case of fiber lasers, the boundary conditions depend on the kind of cavity used in the laser configuration. The number of equations to be solved depends on the width and therefore the number of slots used to discretize the wavelength spectrum. In other words, if the spectrum is divided into n intervals, the number of equations to be solved will be ($2n$ + 4) [51]. Coefficient 2 accounts for the forward and backward amplified spontaneous emission frequencies in each slot. For example, if we consider the spectrum of Erbium ions expands from approximately 1500 nm to 1650 nm, then it can be divided into 100 slots of width 1.5 nm each resulting in 204 equations to be solved. Nevertheless, it is worth mentioning that the number of equations determines the computational speed of the method. Therefore, the optimized method should be found where both the minimum number of equations without compromising accuracy can be obtained.

3.6.1 Runge-Kutta method

Runge-Kutta (RK) method is generally referred to as "$RK4$", the "classic Runge–Kutta method" or simply as "the Runge–Kutta method". As it is well known it is an efficient and commonly used approach for solving initial-value problems of differential equations [78]. Since Equations 3.9–3.12 are a set of first-order differential equations with a unique independent variable z, they can be solved by the Runge-Kutta method. Given ordinary Equations 3.9–3.12, considered as

$$\frac{dy}{dx} = f(x,y) \tag{3.16}$$

with initial conditions x_0 andy_0, the RK method can be applied. In this case, first, a step interval h is chosen. h is the step between the two points at which equations must be solved, that is

$$x_{n+1} = x_n + h \tag{3.17}$$

The following relation gives the corresponding value of the function at this point

$$y_{n+1} = y_n + \Delta_y \tag{3.18}$$

where,

$$k_1 = h.f(x_n, y_n) \tag{3.19}$$

$$k_2 = h.f(x_n + \frac{h}{2}, y_n + \frac{k_1}{2}) \tag{3.20}$$

$$k_3 = h.f(x_n + \frac{h}{2}, y_n + \frac{k_2}{2}) \tag{3.21}$$

$$k_4 = h.f(x_n + h, y_n + k_3) \tag{3.22}$$

$$\Delta_y = \frac{1}{6}(k_1 + 2k_2 + 2k_3 + k_4) \tag{3.23}$$

Here y_{n+1} is the $RK4$ approximation of $y(x_{n+1})$, and the next value (y_{n+1}) is determined by the present value (y_n) plus the weighted average of four increments, where each increment is the product of the size of the interval, h, and an estimated slope specified by function f on the right-hand side of the differential equation. It should be mentioned that for each of the pumps, signal, forward ASE, and backward ASE wavelength, $RK4$ initialization must be written separately. Recently, the $RK4$ for ODE systems of the Er-doped amplifier system has been successfully employed [79].

3.6.2 Shooting methods

The ODE system of Equations 3.9–3.12 can be solved by the shooting methods. These methods include a trial and error scheme in which the unknown boundary value at the beginning of the fiber ($z = 0$) is guessed. The system of equations is then integrated from $z = 0$ to the end of the fiber ($z = L$), where the boundary condition at $z = L$ is applied to the field. The equations are then integrated from $z = L$ to $z = 0$. The calculated boundary value at $z = 0$ is compared with the guessed value and the difference is used to correct the guess in subsequent trials. Guess correction can be done using a classical one-dimensional root-finding technique such as the secant method or Newton-Raphson method. More details about these methods can be found in [51].

3.6.3 Relaxation methods

In relaxation methods, the pump, signal, and ASE power are integrated back and forth using the boundary conditions at each end until the change of population density distribution from one iteration to the next is below a fixed value. The relaxation method has the advantage of a high speed of convergence and robustness [51].

3.6.4 Finite difference methods

The system of rate and propagation equations presented in the previous section is appropriate to model fiber lasers, particularly in continuous wave regime. Nevertheless, in the case of pulsed fiber lasers or strongly time-dependent phenomena such as

transient states, the mentioned system of equations in 3.9–3.12 is no longer applicable. This is due to the significance of level population densities and other parameters' temporal dependence. In these conditions, a traveling wave model is preferred to employ. The model includes a system of coupled partial differential equations with time and space as variables. The traveling wave model equations in the simple case of a two-level fiber laser system with N_1 and N_2 can be written as follows:

$$N_t = N_1 + N_2 \tag{3.24}$$

$$\begin{aligned}\frac{\partial N_2}{\partial t} + \frac{N_2}{\tau} = \frac{\Gamma_p \lambda_p}{hcA}[\sigma_a(\lambda_p)N_1 - \sigma_e(\lambda_p)N_2](P_p^+ + P_p^-) \\ + \sum \frac{\Gamma_k(\lambda_k)}{hcA}[\sigma_a(\lambda_k)N_1 - \sigma_e(\lambda_k)N_1](P_k^+ + P_k^-)\end{aligned} \tag{3.25}$$

$$\pm\frac{\partial P_p^\pm}{\partial z} + \frac{1}{\nu_p}\frac{\partial P_p^\pm}{\partial t} = -\Gamma_p[\sigma_e(\lambda_p)N_2 - \sigma_a(\lambda_p)N_1]P_p^\pm(z,t) - \alpha_p(\lambda_p)P_p^\pm(z,t) \tag{3.26}$$

$$\begin{aligned}\pm\frac{\partial P_k^\pm}{\partial z} + \frac{1}{\nu_k}\frac{\partial P_k^\pm}{\partial t} = -\Gamma_k[\sigma_e(\lambda_k)N_2 - \sigma_a(\lambda_k)N_1]P_k^\pm(z,t) \\ -\alpha_a(\lambda_k)P_k^\pm(z,t) + 2\sigma_e(\lambda_k)N_2\frac{hc^2}{\lambda_k^3}\Delta\lambda_k\end{aligned} \tag{3.27}$$

where $k = 1, ..., K$, N is dopant concentration, A is effective dopant area. The parameters ν_k and ν_p represent the group velocities of the amplified spontaneous emission and pump power in the doped fiber, and c is the speed of light in free space. The system of Equations 3.24-3.27 are completed by boundary condition which depends on the type of cavity in the laser configuration and also on the pumping scheme. If time-dependent boundary conditions are taken into account, the coupled propagation equations must be solved numerically using the finite difference method (FDM).

Applying the FDM to a differential equation involves replacing all the partial derivatives in the equations with a finite difference formula. Accordingly, the space

axis and time axis are divided into small pieces Δ_z and Δ_t respectively. Then the differential equation is transformed into a set of algebraic equations that can be evaluated with numerical methods. In this way, a grid of points gives the value of the pump power, forward and backward output power at every point of the gain medium and every time [51]. Generally speaking, FDMs can be divided into three groups explicit finite difference, implicit finite difference, and Crank-Nicholson [80]. Amongst all these three, the easiest one to implement is the explicit method. However, it has a disadvantage. It is only numerically stable and convergent when the courant condition ($\Delta_t = \frac{\Delta_z}{v}$) is satisfied. On the other hand, the other two methods, namely, implicit finite difference, and Crank-Nicholson are always stable but they have the disadvantage of intensive computations. Between these two methods, Crank-Nicholson is even more stable.

Due to the flexible conditions at which FDM applies to the system of rate and propagation equation, it is chosen in the analysis of the 4-level system of $Dy-$doped fiber laser, discussed in this thesis.

Chapter 4

Dy−doped Fiber Laser Model and Results

4.1 Mathematical model for Dy−doped fiber laser

According to the FDTD method, chosen for the system's modeling, the rate and propagation Equations 3.1–3.12 written in the previous chapter for Dy−doped fiber, are rewritten as

$$\frac{\partial N_2(z,t)}{\partial t} = \sum_{k=1}^{K} \frac{\Gamma_k \lambda_k}{h \nu_k A_k} [\sigma_{12}(\lambda_k) N_1 - \sigma_{21}(\lambda_k) N_2](P_k^+(z,t) + P_k^-(z,t)) - \frac{N_2(z,t)}{\tau} \quad (4.1)$$

$$N_t = N_0 + N_1 + N_2 + N_3 \quad (4.2)$$

$$\pm \frac{\partial P_p^{\pm}(z,t)}{\partial z} + \frac{1}{\nu_p} \frac{\partial P_p^{\pm}(z,t)}{\partial t} = -\Gamma_p [\sigma_{30}(\lambda_p) N_3 - \sigma_{03}(\lambda_p) N_0] P_p^{\pm}(z,t) - \alpha_p(\lambda_p) P_p^{\pm}(z,t) \quad (4.3)$$

$$\begin{aligned}\pm\frac{\partial P_k^{\pm}(z,t)}{\partial z}+\frac{1}{\nu_k}\frac{\partial P_k^{\pm}(z,t)}{\partial t} &= \Gamma_k[\sigma_{21}(\lambda_k)N_2-\sigma_{12}(\lambda_k)N_1]P_k^{\pm}(z,t)\\ &\quad -\alpha_a(\lambda_k)P_k^{\pm}(z,t)+2\sigma_{21}(\lambda_k)N_2\frac{hc^2}{\lambda_k^3}\Delta\lambda_k \\ &\quad k=1,.....,K,k\neq s\end{aligned} \tag{4.4}$$

where N_t is the dysprosium dopant concentration, which is assumed to be uniform along the fiber. N_0 and N_3 are ground and stimulated level populations, N_1 and N_2 are lower and upper lasing level populations. P_p shows the pump power and P_k shows the ASE power of each channel ($\pm$ corresponds to forward and backward propagation, respectively). It should be mentioned that, in the presence of the forward signal, P_k thus represents the lasing or signal power. This processing is rational, because, in the corresponding spectral slot ($k=s$), the signal power is stronger than the ASE one by at least three orders of magnitude, and ASE can be regarded as a weak background noise. ν_p and ν_k are the group velocities of the pump and ASE in the fiber. In our Dy− doped fiber system, the chromatic dispersion effect can be neglected, thus ν is independent of wavelength. σ_{03} and σ_{21} are the pump absorption and yellow signal emission cross sections of dysprosium ions, respectively. A is the doped area of the Dy−doped fiber, and Γ_p (Γ_k) is the overlapping factor between the pump (ASE) field and the fiber-doped area. The initial boundary conditions on the propagating waves associated with the above partial differential equation (PDEs) are written as

$$\begin{aligned}P_p^{+}(0,t) &= P_p^{+}(t)\\ P_p^{-}(L,t) &= P_p^{-}(t)\\ P_k^{+}(0,t) &= P_s(t), k=s\\ P_k^{+}(0,t) &= 0, k\neq s\\ P_k^{-}(L,t) &= 0, k\neq s\end{aligned} \tag{4.5}$$

where $P_p^{+}(t)$ and $P_p^{-}(t)$ are forward and backward pump powers injected into the Dy−doped fiber. $P_s(t)$ is the input signal power and ASE forward and backward pow-

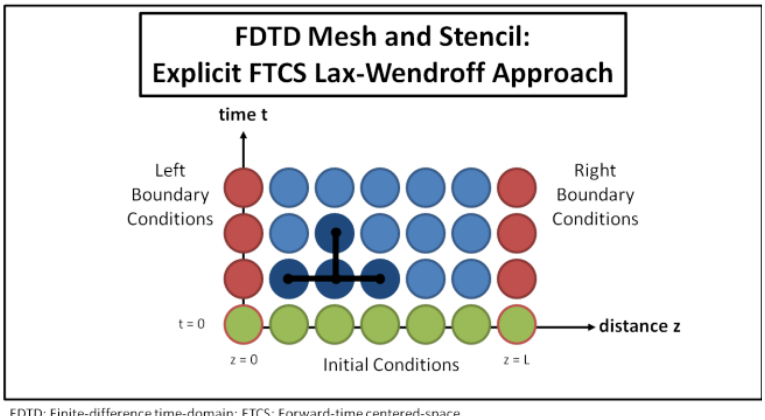

Figure 4.1: Numerical simulation mesh and FDTD stencil [82].

ers at the beginning and end of fiber are zero ($P_k^+(0,t), P_k^-(L,t)$). The above initial-boundary-value problem of a Dy− doped fiber amplifier system can be numerically solved through FDM and inserting the correct values for the fiber parameters, pump and input signals, and resonator or amplifier losses.

4.1.1 Forward-Time, Centered-Space explicit FDM

For solving the 1D PDEs 4.1-4.5, many solvers exist. However, we have primarily chosen to use a MATLAB toolbox dedicated to Er and Yb−doped fiber amplifiers and lasers. This selection has been made based on the flexibility of the simulation, and considering time-varying parameters, offered by the FDTD method in this toolbox. The employed simulation shown in Figure 4.1 is based on a forward-time centered-space (FTCS) FDTD approach [81].

Equation 4.5, can be written as an inhomogenous one-way wave equation by combining the right-hand side into a single term $F(z,t)$

$$\frac{\partial P(z,t)}{\partial z} + \frac{1}{v}\frac{\partial P(z,t)}{\partial t} = F(z,t) \tag{4.6}$$

Notably, wavelength dependence is dropped for clarity and all initial and bound-

ary conditions are given by Equations 4.5. After rearranging Equation 4.5, to solve for $\frac{\partial P(z,t)}{\partial t}$, we obtain

$$\frac{\partial P(z,t)}{\partial t} = -\frac{\partial P(z,t)}{\partial z} + \nu F(z,t) \tag{4.7}$$

The Taylor series expansion of $P(z,t)$ around t is

$$P(z,t+\Delta t) = P(z,t) + \Delta t \frac{\partial P(z,t)}{\partial t} + O(\Delta t^2) \tag{4.8}$$

and the FTCS approximation of $\frac{\partial P(z,t)}{\partial z}$, is

$$\frac{\partial P(z,t)}{\partial z} = \frac{P(z+\Delta z,t) - P(z-\Delta z,t)}{2\Delta z} \tag{4.9}$$

Then, after replacing Equations 4.7 and 4.9 in Equation 4.8 we will have

$$P(z,t+\Delta t) = P(z,t) + \Delta t[-\nu \frac{P(z+\Delta z,t) - P(z-\Delta z,t)}{2\Delta z} + \nu F(z,t)] + O(\Delta t^2) \tag{4.10}$$

After that, a Lax-Wendroff modification has been used to ensure numerical stability [82]. This approach selects the first three terms of the Taylor series expansion:

$$P(z,t+\Delta t) = P(z,t) + \Delta t \frac{\partial P(z,t)}{\partial t} + \frac{\Delta t^2}{2} \frac{\partial^2 P(z,t)}{\partial t^2} + O(\Delta t^3) \tag{4.11}$$

By using the Equation 4.7, the partial derivatives of $P(z,t)$ can be expressed as

$$\frac{\partial P(z,t)}{\partial t} = -\nu \frac{\partial P(z,t)}{\partial z} + \nu F(z,t) \tag{4.12}$$

$$\frac{\partial^2 P(z,t)}{\partial^2 t} = \nu^2 \frac{\partial^2 P(z,t)}{\partial z^2} - \nu^2 \frac{\partial F(z,t)}{\partial z} + \nu \frac{\partial F(z,t)}{\partial t} \tag{4.13}$$

where the partial derivatives of $F(z,t)$ can be expressed using the FTCS approximations

$$\frac{\partial F(z,t)}{\partial z} = \frac{F(z+\Delta z,t) - F(z-\Delta z,t)}{2\Delta z} \tag{4.14}$$

$$\frac{\partial F(z,t)}{\partial t} = \frac{F(z,t+\Delta t) - F(z,t)}{\Delta t} \tag{4.15}$$

Substituting Equations 4.12 - 4.15 into the Taylor series of $P(z,t)$ (Equation 4.10) allows explicit propagation in time with second-order accuracy to both space and time.

$$P(z,t+\Delta t) = P(z,t) + \Delta t[-\nu\frac{\partial P(z,t)}{\partial z} + \nu F(z,t)] + \frac{\Delta t^2}{2}[\nu^2\frac{\partial^2 P(z,t)}{\partial z^2} - \nu^2\frac{F(z+\Delta z,t) - F(z-\Delta z,t)}{2\Delta z} + \nu\frac{F(z,t+\Delta t) - F(z,t)}{\Delta t}] + O(\Delta^3) \tag{4.16}$$

The temporal step size Δt is chosen according to the Courant-Friedrichs-Lewy condition $\frac{\nu\Delta t}{\Delta z} \leq 1$ to ensure stability. The upper laser population $N_2(z,t)$ is calculated from Equation 4.1 after each time step. The simulation is considered to have converged when subsequent time iterations produce no change above a convergence threshold (set to 10^{-3} by default) in any value of $P^{\pm}(z,t,\lambda)$. It should be noted that simulation run times depend on the number of points in the spatial mesh. Mesh spacing is driven by the gain per fiber length of the system: a fast-changing signal requires a denser mesh for convergence. Due to the characteristics of the system, simulating a high gain amplifier or laser stage requires high mesh density for convergence so the simulation time is relatively long.

4.2 Method's verification

Verification of the explicit forward-time centered-space FDTD method is carried out in 3 steps. As we mentioned this method has been primarily written for an Er−doped amplifier. Therefore we first simulated the Er−doped fiber amplifier with other numerical methods implemented in MATLAB and Python, and secondly compared the obtained results. Having confirmed the accuracy of this method in an effective or quasi-two-level system, we extended it to a four-level system by writing the rate and propagation Equations 4.1-4.4. Then we analyzed a four-level system that is a

Nd−doped fiber amplifier with this method. The obtained results show a good agreement with the Nd−doped fiber amplifier analyzed in [83]. Finally, we have applied the modified method to our interested Dy−doped fiber amplifier system.

4.2.1 Er−doped fibre amplifier

Er−doped fiber amplifiers (EDFAs) are extensively employed in fiber optical networks. They can provide amplification for long-distance systems based on the fibers with a loss of less than 0.2 dB/km, for signals in the long wavelength window near 1550 nm. Practically, the most common EDFA configuration is the forward pumping one using the 980 nm pump. This is because this configuration makes the most efficient use of cost-effective, reliable, and low-power consumption fiber amplifiers. An Er−doped fiber amplifier with physical parameters similar to the one discussed in [76], is considered. Energy levels of the Er−doped system, with their spectroscopy notation, are shown in Figure 4.2. As can be seen, there are three energy levels: the $^4I_{15/2}$, $^4I_{13/2}$, and $^4I_{11/2}$ representing respectively the ground state, the upper state, and the metastable state. The populations of the levels are labeled N_1, N_2, and N_3. To have amplification, a population inversion is necessary between states 1 and 2, and since state 1 is also the ground state, at least half of the total population of erbium ions needs to be excited to level 2 to have population inversion. The incident beam of light on the system with appropriate frequency, able to excite ions to higher levels, is called pump radiation. In the examined EDFA, the pump is chosen at 980 nm which excites the ions to the upper-level $^4I_{11/2}$. The lifetime of this upper level is approximately 1 μs. Thus, the ions readily decay to the metastable level $^4I_{13/2}$ by non-radiative transition, i.e. by releasing heat. The time constant at the metastable energy state $^4I_{13/2}$, is 10 ms and, therefore, relatively high. This leads to a high population inversion even at moderate pump powers. Propagation equations and population equations have been written for a 3-level system of Er^{3+} with 980 nm pump wavelength but with an approximation of a quasi-two-level system ($N_3 = 0$).

The EDFA considered here is similar to the one in [76], since the fiber has a core radius of 1.4 μm and a refractive index difference between core and cladding of 0.026. The overlap integral between mode intensity and erbium distribution is

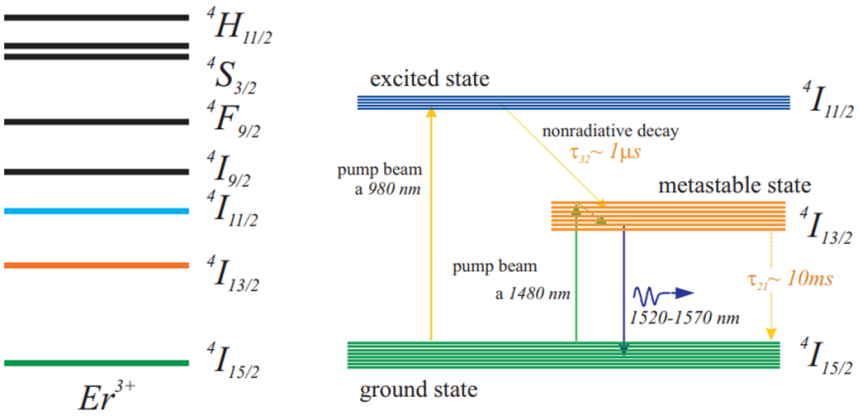

Figure 4.2: Energy levels of Erbium (Er^{3+}) doped system with their spectroscopy notation. there are three energy levels: the $^4I_{15/2}$, $^4I_{13/2}$, and $^4I_{11/2}$, representing respectively the ground state, the upper state, and the metastable state

Γ= 0.40 at 1550 nm, and Γ= 0.64 at 980 nm. This fiber has an Er^{3+} concentration N_t= 0.7 x 10^{19} cm^{-3}, which is typical of erbium-doped fibers with a few hundred ppm of dopant. This EDFA has been mainly selected because in [76] it has been experimentally measured and theoretically evaluated. The absorption and emission cross-section spectra for EDFA are shown in Figure 4.3. As can be seen for erbium, the emission cross-section is higher than the absorption one in all the wavelength range 1540-1620 nm, whereas at the pump wavelength of 980 nm the emission cross-section is zero. This property is one of the reasons for employing the EDFA in a wide range of applications [77].

Using the given parameters of the Er−doped fiber amplifier, the upper state population inversion ($\frac{N_2}{N_{tot}}$) has been simulated at different values of pump input power. In Figure 4.4 the results calculated with the FTCS method are compared with those obtained in [76]. As can be seen in this figure, the FTCS method (green curves), predicts the same depletion behavior of the population inversion along the fiber length, showing in [76] when the pump input power decreases. In fact, at low input pump power, most of the 980 nm pump is absorbed at the beginning of the fiber. The peak in the population inversion for 40 mW of pump power that is reached near 6 to 8 m,

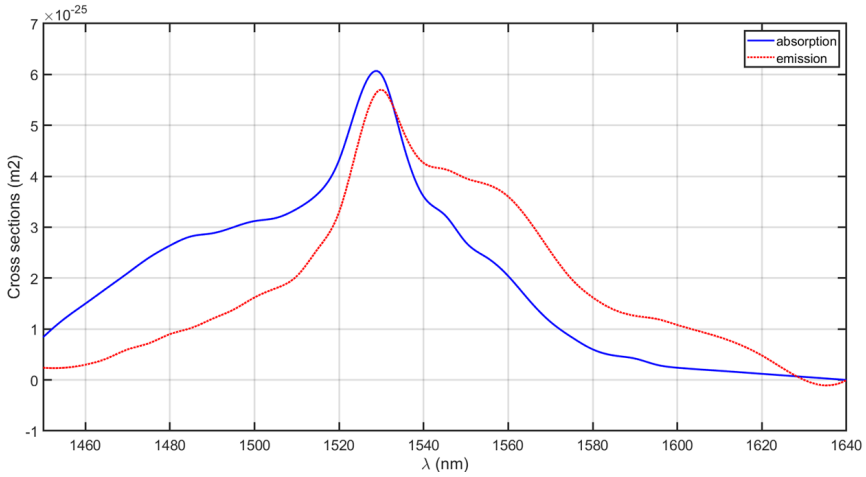

Figure 4.3: A typical absorption and emission cross-section spectra of erbium-doped fiber amplifier.

is because at this position the total ASE (forward and backward) is lowest. It is worth mentioning that the population inversion is lower at the beginning of the fiber, even though the 980 nm pump power is highest there because the backward propagating ASE has reached its highest power and it is significantly depleting the population.

To further verify the correctness of the FTCS method, it is also instructive to calculate another fundamental parameter which is the signal gain. The gain represents the ratio of a signal's output power P_{out} to its input power P_{in}. This parameter depends on different population density levels, and cross-section spectra, and it changes along the length of the fiber [77]. The results for the considered EDFA with a length of 14 m pumped at 980 nm with the small signal power of -40 dBm input at 1550 nm, are shown in Figure 4.5. As can be seen in Figure 4.5, the signal gain calculated by the FTCS method for three different pump powers is similar to the results obtained in [76]. The obtained gain is governed by the population inversion shown in Figure 4.4. For the lowest pump power of 4 mW, in the last section of the fiber, the population inversion is too low and there is an attenuation of the signal rather than gain. As the signal gain is proportional to $(\sigma_{em}N_2 - \sigma_{ab}N_1)$, it has been remarked in [76], when

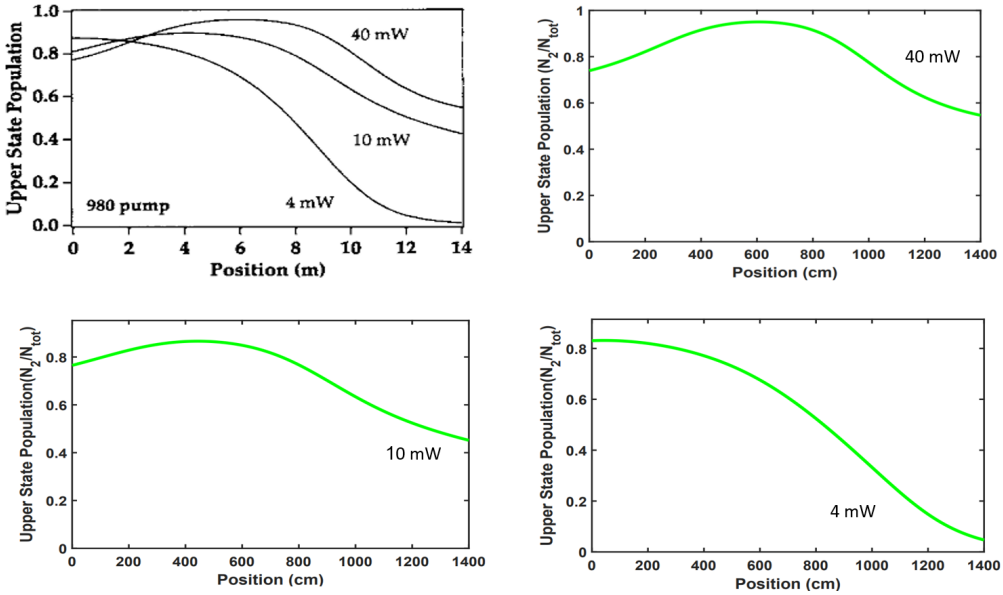

Figure 4.4: Population in the upper state as a function of position along a 14 m long Er−doped fiber amplifier, pumped at 980 nm with different pump powers indicated on the graphs calculated with (top, right) a numerical method mentioned in [76], and with (top, left) the proposed FTCS for 40 mW pump power, (down, right) 10 mW pump power, and (down, left) 4 mW pump power.

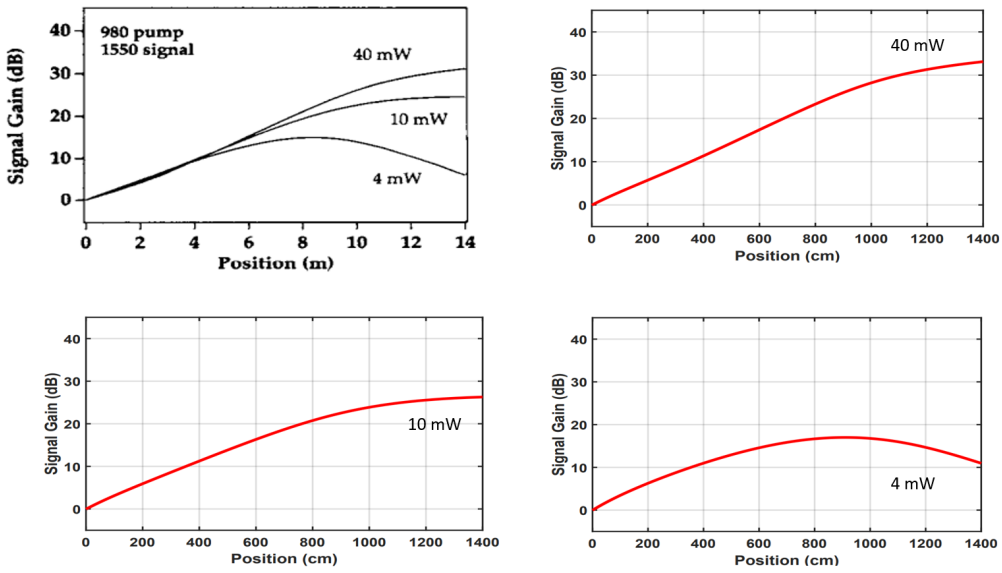

Figure 4.5: Signal gain as a function of position along a 14 m long Er−doped fiber amplifier, pumped at 980 nm with different powers indicated on the graphs calculated with (top, right) a numerical method mentioned in [76], and with (top, left) the proposed FTCS for 40 mW pump power, (down, right) 10 mW pump power, and (down, left) 4 mW of pump power.

$(\frac{N_2}{N_{tot}})$ drops below $(1+\frac{\sigma_e}{\sigma_a})^{-1}$ the signal experiences loss rather than gain.

The last important parameter in the fiber amplifier system considered here is ASE. I have calculated the ASE for the considered EDFA. The total forward and backward ASE power is calculated in the wavelength range of the emission spectrum of the considered EDFA, starting from 1450 nm and ending at 1600 nm. It is noteworthy to mention that ASE modeling has been performed by dividing the range into small wavelength slots of width $d\lambda$ much smaller than the transition bandwidth. The power within each wavelength step can then be propagated as an independent signal and the spectral shape of the output ASE can be computed. An extra complication is that the ASE can propagate in both directions along the fiber, that is co-propagating and counter-propagating with the signal. Figure 4.6 shows the total forward and backward

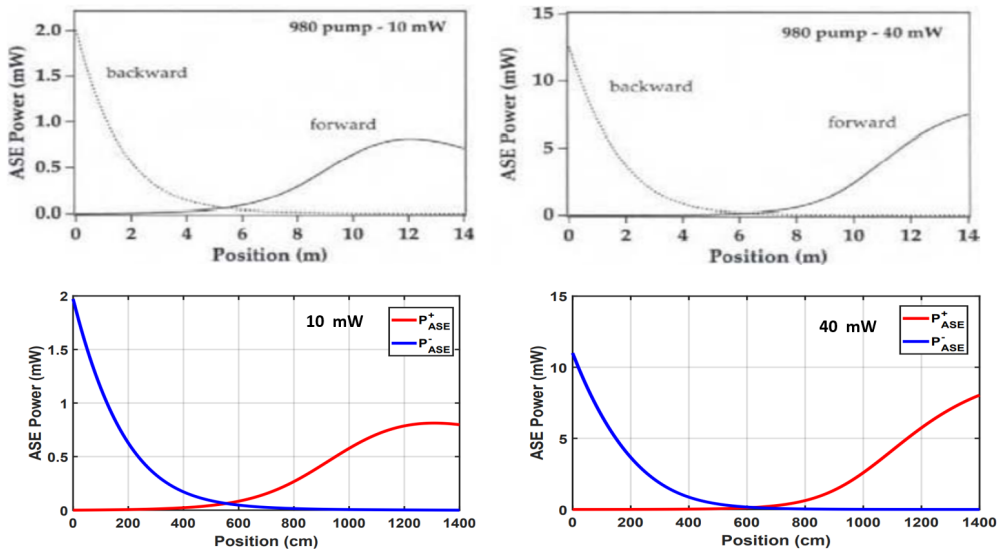

Figure 4.6: Forward (P^+_{ASE}) and backward (P^-_{ASE}) traveling ASE powers in a 14 m long EDFA pumped at 980 nm, with different pump powers indicated on the graphs calculated with a (top, right) numerical method mentioned in [76] for 10 mW pump input power, (top, left) the same numerical method mentioned in [76] for 40 mW pump input power, and with the (down, right) proposed FTCS for 10 mW pump power, and (down, left) 40 mW of the pump power.

ASE as a function of position, for 980 nm pumping wavelength. As can be seen, the results predicted with FTCS are consistent with the ones reported in [76]. The backward ASE benefits from traveling along a piece of fiber with population inversion, while the forward ASE propagates along a piece of the fiber progressively where the population inversion reduces being less amplified. This causes the forward ASE power to evolve more slowly along the fiber length, compared with the backward ASE one.

Having compared the three important parameters of population inversion, gain, and ASE power with their equivalent values reported in [76], we found a high matching between the FTCS results and the analytical method used in [76]. However, to further show the reliability and strengths of the FTCS method we have considered an-

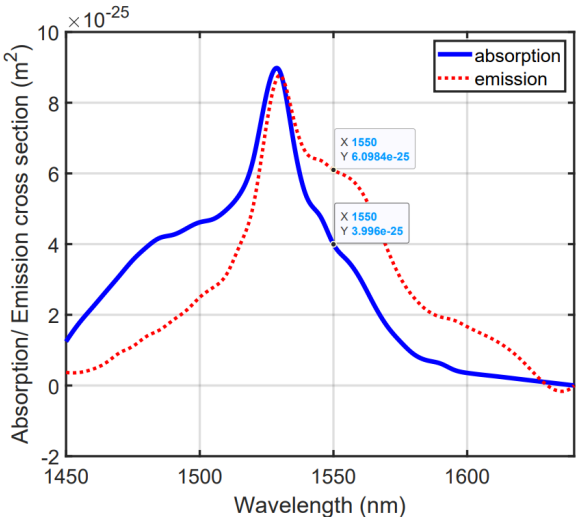

Figure 4.7: Absorption and emission cross-section spectra of the erbium-doped fiber amplifier pumped at 980 nm, calculated and re-scaled according to the absorption and emission cross-section values of the considered fiber [77].

other typical EDFA used for communication and we have evaluated the performance of the EDFA with MATLAB tool using the Runge–Kutta method utilized in Matlab, and an FDM-based tool in Python environment. Then we compared the results of these two methods with the FTCS method's ones. The parameters of the considered EDFA are a fiber core radius of 4 μm, doping concentration N_t = 3 x 10^{24} m $^{-3}$, and a length of 12 m. The overlap integrals for respectively pump and signal waves are $\Gamma_p = 0.93$ and $\Gamma_s = 0.78$. The absorption and emission cross-section values are shown in Figure 4.7. The pump absorption cross-section at 980 nm is 2.5 x 10^{-25} m ^{2}.

The first parameter calculated by all three methods is the higher-lasing level population, N_2. As can be seen in Figure 4.8, the proposed FTCS method predicts a population of 2.87×10^{24} at the beginning of fiber, which is consistent with the predicted values by Runge-Kutta [79] and FDM simulations.

The second parameter evaluated is the pump and signal/lasing power along the fiber. As can be seen in Figure 4.9, the Runge-Kutta method predicts that the signal

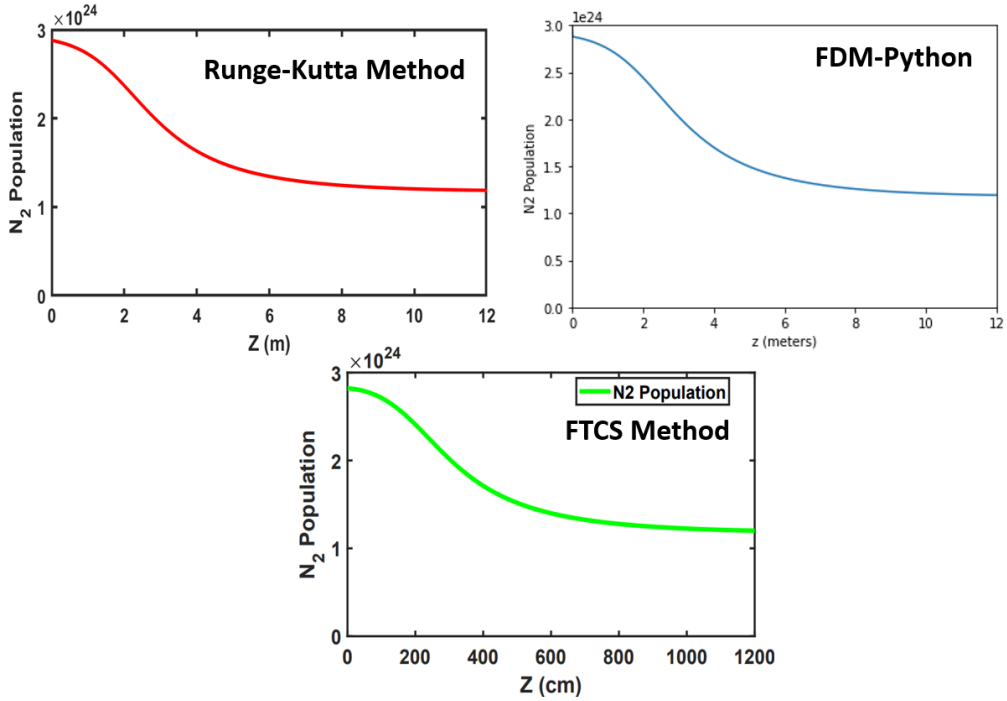

Figure 4.8: Upper laser level population as a function of position along a 12 m length of the considered EDFA, pumped at 980 nm, computed by Runge-Kutta method (top, right) FDM (top, left) and the proposed FTCS (down).

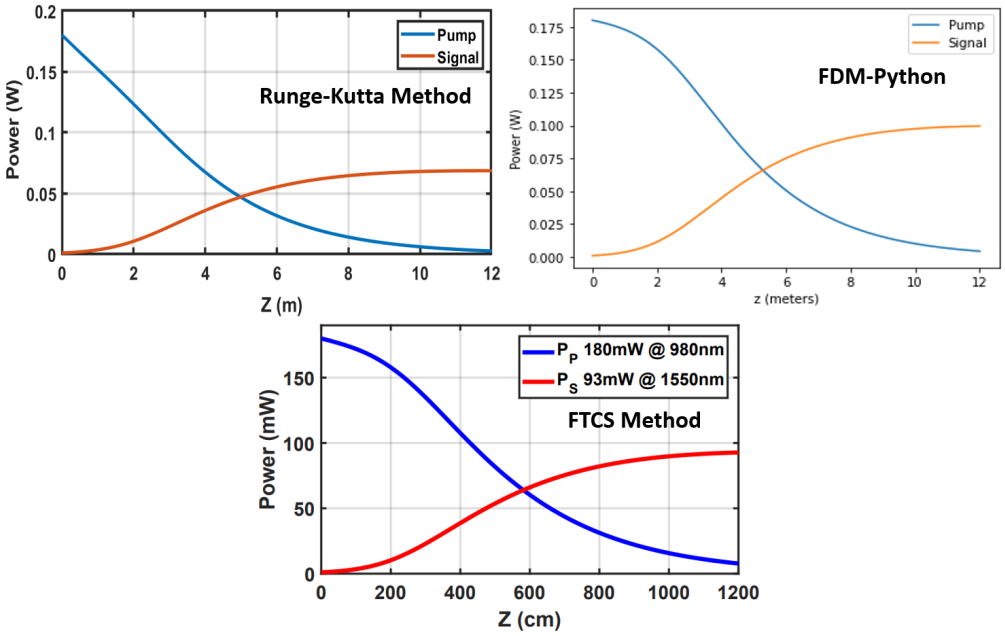

Figure 4.9: Pump and signal power evaluation as a function of position along a 12 m length of the considered EDFA, pumped at 980 nm computed by Runge-Kutta method (top, right) FDM, (top, left) the proposed FTCS (down).

power with an input pump power of 180 mW, increases from 1 mW to 80 mW at the end of fiber. However, the corresponding value in the FTCS method is 93 mW, and in FDM simulations is 100 mW. The main reason for the different predicted powers is that, unlike the two methods of FTCS and Runge-Kutta, in FDM simulations ASE is not considered. Furthermore, the way of calculating ASE with the two methods of FTCS and Runge-Kutta is also different. However, the depletion of the pump power during the propagation along the fiber length is truly predicted by all three methods.

We finally calculated the signal gain along the fiber length illustrated in Figure 4.10. It can be observed that almost all three methods predict a signal gain of 20 dB at the end of the fiber. Regarding the obtained results, the high-data matching between the employed FTCS method and Runge-Kutta method in MATLAB [79] and the house-written FDM codes in Python is confirmed.

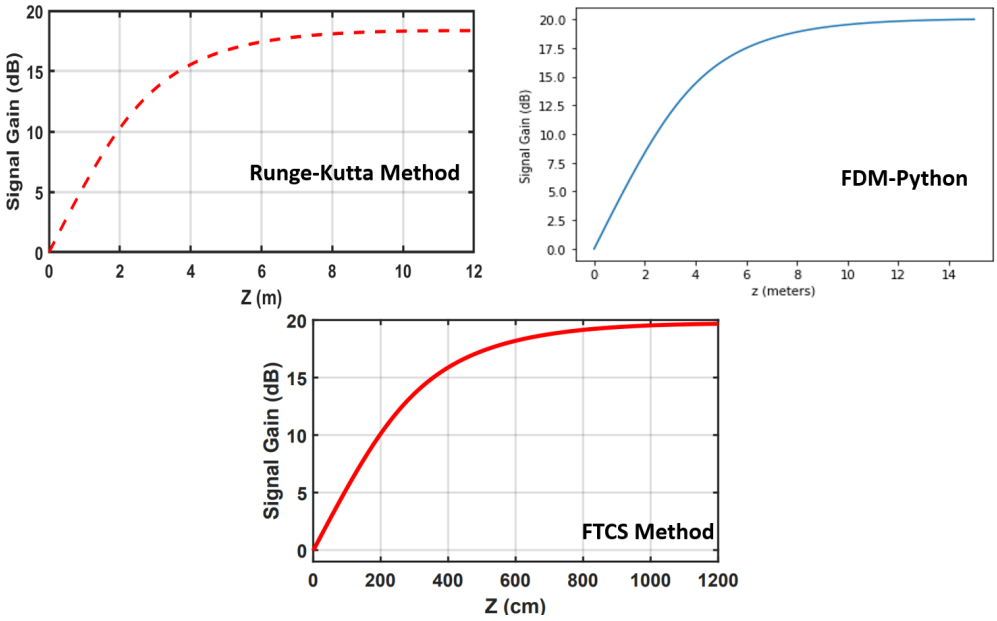

Figure 4.10: Signal gain calculation as a function of position along a 12 m length of the considered EDFA, pumped at 980 nm computed by Runge-Kutta method (top, right) FDM, (top, left) the proposed FTCS (down).

4.2.2 Nd−doped fibre amplifier

After confirming the accuracy of the FTCS method for the two-energy level system of EDFA, through the comparison with other methods, I developed the method for four-energy level systems. I rewrote the rate and propagation equations in this case. The equations were fully described in Sec. 3.5. By applying the FTCS method to these equations, a model for four-energy level amplifiers and lasers is obtained. Before applying this model to the four-energy level system of Dy-doped fiber amplifiers, I verified its correctness. To do that, I used this model to study the performance of the 4-energy level system of an Nd-doped fiber amplifier. The aim was to compare the developed FTCS methods results with the ones obtained with other methods in the case of the 4-energy level system of Nd−doped fiber amplifier [83]. The considered parameters are given in Table 4.1.

Table 4.1: Physical and structural parameters of the four-level system of Nd-doped fiber amplifier [83].

Parameter	value
λ_p	808 nm
λ_s	1060 nm
Γ_s	0.75
Γ_p	0.002
σ_p	2×10^{-24} m ^{2}
P_s	0.1 W
P_p	1, 10 W
τ	4 ms
n	1.5
L	200 m
A	5×10^{-11} m^2
N_t	$2 \times 10^{+24}$ m^{-3}
α	3×10^{-3} m^{-1}

The schematic of the four-energy level system of Nd-doped fiber amplifier (NDFA)

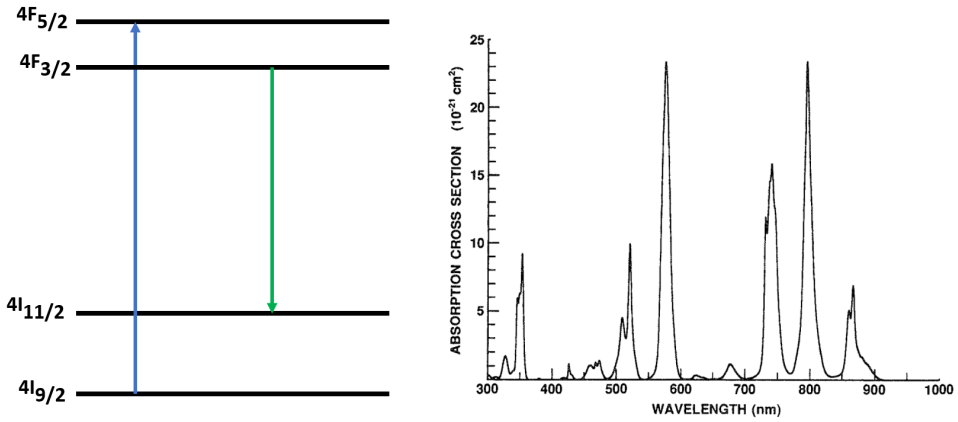

Figure 4.11: (left) Energy-level schematic diagram of Nd^{3+}. The ground-state absorption (GSA) at $\sim$ 808 nm is shown with an upward arrow, The amplifying levels, ${}^4F_{3/2}$ and ${}^4I_{11/2}$, generate emission in the 1060 nm region, as shown by the downward arrow, and (right) the absorption cross-section of Nd^{3+} [69].

is shown in Figure 4.11. As can be seen in this figure, the levels involved in the pumping process are ${}^4I_{9/2}$ and ${}^4F_{5/2}$. The amplification of the signal occurs with ${}^4F_{3/2} \rightarrow {}^4I_{11/2}$ energy transition. In the same Figure, the absorption cross-section for Nd, experimentally obtained in the wavelength range of 300-900 nm [69], is shown. We used the value of 2×10^{-24} m ^{2} as the pump absorption cross-section at 808 nm.

The emission cross-section spectrum of Nd3+ in different glasses is shown in Figure 4.12. We used these spectra to obtain the emission and absorption cross-sections in the wavelength range 1020-1120 nm, considered in the whole process of NDFA calculations. We analyzed the power evolution of the pump and signal waves propagating in the NDFA described in Table 1.1.

Signal amplification for the forward pumping scheme of the considered NDFA for an input launched pump power of 10 W is shown in Figure 4.13. On the right side of this Figure, the solutions obtained by [83] are given. The continuous line shows the numerical solutions whereas the circles describe the approximate analytical ones. Note the excellent agreement between the two of them and on the other hand, the

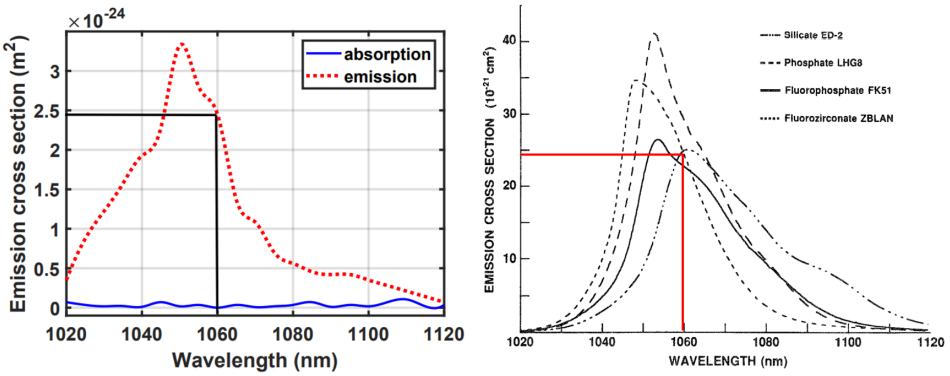

Figure 4.12: (right) ${}^4F_{3/2}$ and ${}^4I_{11/2}$ emission cross-section spectra for different glass types for pumping at 800 nm [69], (left) Emission cross-section of Nd^{3+} used in our calculation.

excellent agreement of both of them with the results of the developed FTCS method for the four-level systems (left side in Figure 4.13). In the results of all three methods, the signal with an input power of 100 mW reaches a maximum power of nearly 3.5 W at 160 m. After this distance, the pump power is too low to amplify the signal, and the latter further slowly attenuates due to scattering loss [83].

To examine the effect of the pumping level on the accuracy of the FTCS method, the previous example is repeated with an input pump power of 1 W. All other parameters are as in Figure 4.13. As can be seen in Figure 4.14, the agreement between our method results and the ones in [83] is quite good. About these cases, it should be mentioned that due to the much lower pump power, the effect of the ASE (which is neglected in the analytic solutions) is more pronounced and, as a consequence, the analytical solutions (circles) for the signal are somewhat higher than the numerical solutions in Figure 4.14, right side. Nevertheless, the agreement between the analytical and numerical methods used in this paper is quite good. It is interesting to note that as the input pump power is reduced by an order of magnitude, the signal is also lower by nearly the same factor (reaching 0.39 W at 160 m length of the NDFA).

The last two cases examined, exploit a forward pumping scheme. In the forward scheme considered in our model, both the signal and pump enter at the beginning

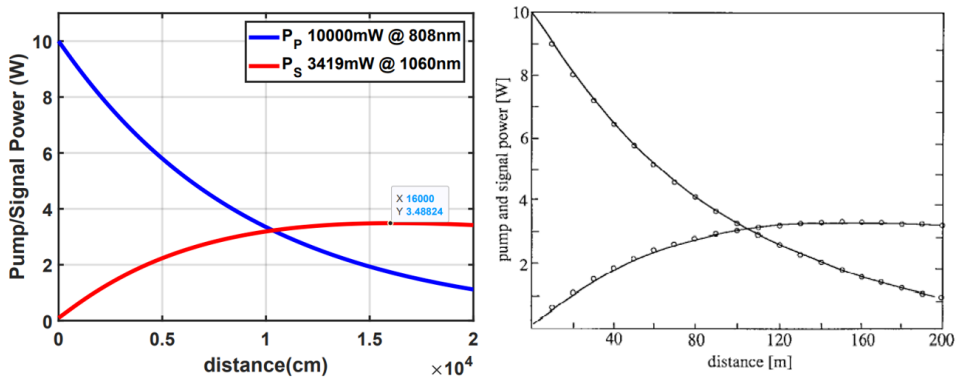

Figure 4.13: (right) Signal amplification and pump attenuation for the four-level system of NDFA for forward pumping at a pump input power of 10 W, obtained by two analytical and numerical methods [83]. Solid lines represent a numerical solution of rate and propagation equations at steady state while circles represent the approximate analytical solutions, and (left) equivalent parameters calculated by the developed FTCS method.

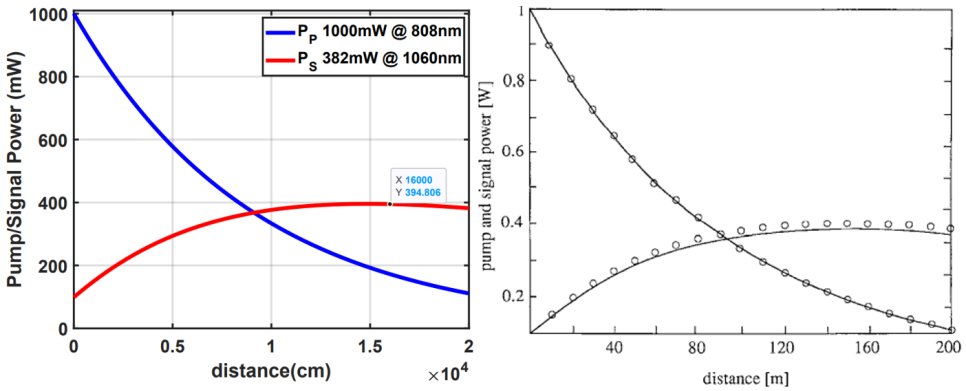

Figure 4.14: Same as the Figure 4.13, but for a pump input power of 1 W.

of the fiber (z = 0 m) which is the same as the forward pumping scheme in [1]. To show the usefulness of the FTCS method, the last two examples will be considered in a backward pumping scheme. In the backward pumping scheme, the pump and signal waves are counter-propagating along the fiber length. In the developed code to study the fiber amplifier, by backward pumping, we mean that the signal is entering at the beginning of the fiber (z = 0 m), and the pump is injected at the ending point of the fiber (z = 200 m). Notice that, the backward pumping considered in [1] is the opposite of our assumptions. In their scheme of backward pumping, the input signal enters from the ending point of the fiber (z = 200 m) and the pump is injected at the beginning of the fiber (z = 0 m). All other parameters are the ones used to obtain results of Figures 4.13 and 4.14. First, we consider the backward pumping with an input power of 10 W. The results are illustrated in Figure 4.15. Consistent with the results in [83], shown in Figure 4.15 (right), for the case of forward pumping, the signal rises monotonically to a value of 4.17 W at the end of the fiber. In the case of forward pumping, the maximum signal power obtained was 3.4 W at the 160 m length of the NDFA (Figure 4.13).

In the second example of the backward pumping scheme, the pump input power is decreased to 1 W injected at $z = 200$ m. The results are illustrated in Figure 4.16. Compared to the results obtained with the forward pumping scheme (Figure 4.14), again an increase in signal output power at the end of the fiber is observable. In summary, predicted results by the FTCS method are in good agreement with both the numerical and analytical method results in four different considered examples. This confirms the validity and correctness of the developed FTCS method for four-level energy systems of fiber amplifiers and lasers.

Notice that different implementations of the backward pumping scheme in our model with the[1], have resulted in the mirror/images in Figures 4.15 and 4.16. However, since all the other parameters are the same the final power of the signal at the opposite end of the fiber is the same.

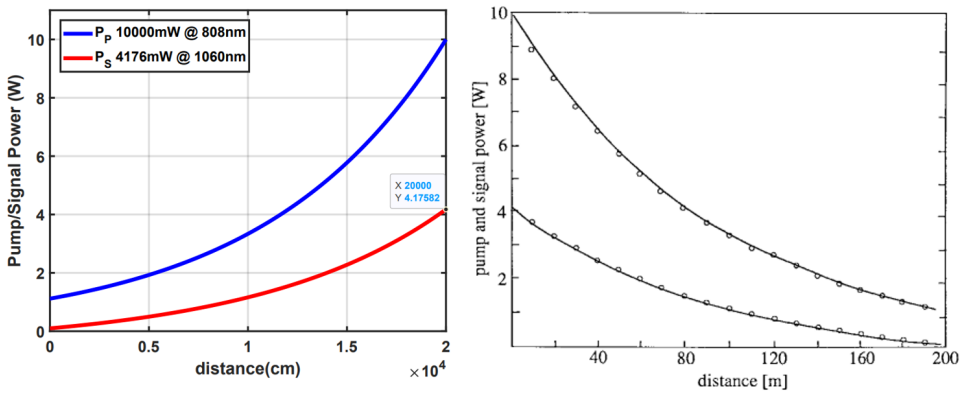

Figure 4.15: (right) Signal amplification and pump attenuation for the four-level system of NDFA for backward pumping at a pump input power of 10 W, obtained by two analytical and numerical methods [83], solid lines represent an exact numerical solution of rate and propagation equations at steady state while circles represent the approximate analytical solutions, and (left) equivalent parameters calculated by the developed FTCS method.

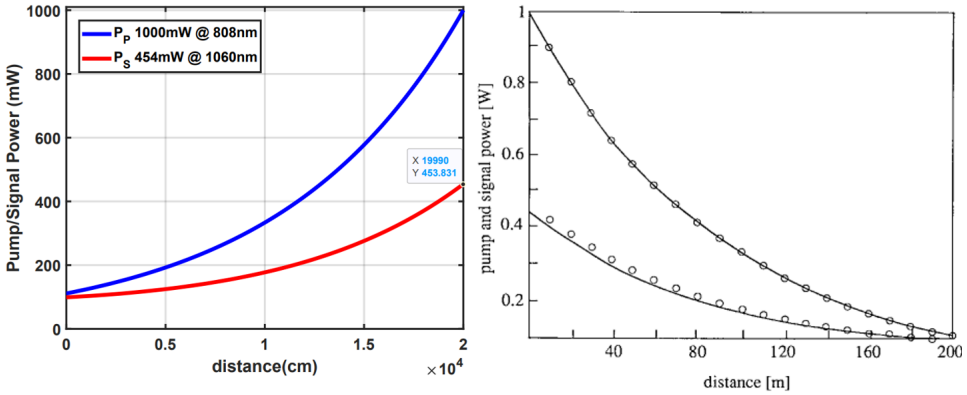

Figure 4.16: same as Figure 4.15 with an input power of 1 W.

4.3 Dy−doped fibre laser

Having confirmed the FTCS method, we have used it for analysis of the Dy−doped fiber laser. A simplified energy level diagram of a Dy−doped fiber is shown in Figure 4.17. As it has been mentioned the $^4F_{9/2} \rightarrow {}^6H_{13/2}$ energy transition, shown in Figure 4.17, produces strong yellow fluorescence ($\sim$ 565-590 nm) [84]. Since, in ZBLAN glass the lifetime of the lower laser level ($^6H_{13/2}$, 0.65 ms) is comparable to the one of the upper laser level ($^4F_{9/2}$, 1.5 ms), the yellow light could also be re-absorbed (as shown by the upward dashed line in Figure 4.17). Hence, a massive population accumulates on the lower laser level, which can subsequently re-absorb the yellow light. To take into account this effect on the lasing performance, a signal re-absorption cross-section is required. Furthermore, according to the lasing transition, for direct excitation of the ground-state population to the upper yellow lasing level, several shorter wavelengths ranging from the ultraviolet to the blue spectral range can be used. Alongside [45, 46], a convenient 450 nm pump source ($^6H_{15/2} \rightarrow {}^4I_{15/2}$) is chosen. The transitions considered in our simulations are shown in Figure 4.17. In this Figure, $A_{32} = 1/\tau_{32}$ shows the nonradiative transition rate of the excited ions from the energy level $^4I_{15/2}$ to the $^4F_{9/2}$ one. Additionally $A_{30} = 1/\tau_{30}$ shows the spontaneous decay rate at the pump wavelength. Finally, the amplified spontaneous emission rate from the upper lasing level to the lower one ($A_{21}(\lambda_s)$), has been also taken into account.

4.3.1 Parameters and Values

In the analysis of Dy−doped fiber lasers we consider a single-clad Dy−doped ZBLAN fiber similar to the one fabricated by Le Verre Fluoré (France) [46]. We first extracted the absorption and emission cross-section spectra of the mentioned Dy−doped fiber from experimental data [45, 46]. The results are presented in Figure 4.18. In the numerical simulation of the spectra, the absorption, emission, and re-absorption cross-sections were calculated in the wavelength range of 550-600 nm with a step of 0.5 nm. On the other hand, in the experimental measurements of the cross-section as explained in [46], the mentioned fiber has been pumped using a GaN laser diode

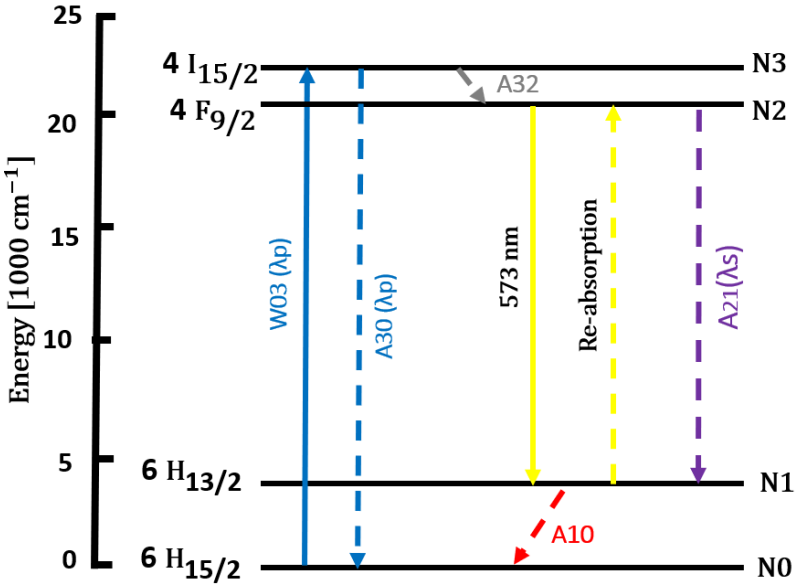

Figure 4.17: Simplified Dy^{3+} energy level diagram shows ground-state absorption (GSA, N_0) for $\sim$ 450 nm pump wavelength with upward arrows. Two lasing levels, $^4F_{9/2}$ and $^6H_{13/2}$, generate emission in the yellow region in ZBLAN glass, shown by the downward arrows. In ZBLAN glass, the lifetime of the lower laser level ($^6H_{13/2}$) of the yellow transition, is comparable to the upper laser level ($^4F_{9/2}$), meaning the yellow light is re-absorbed (as shown by the upward dashed line).

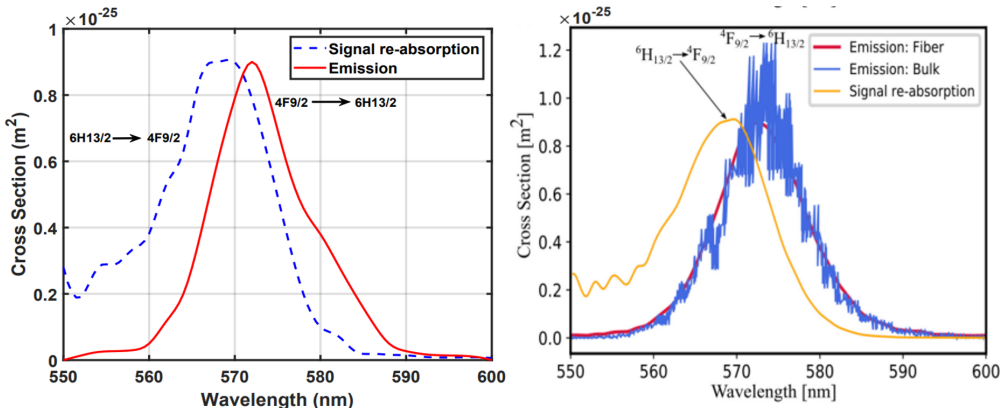

Figure 4.18: (left) Emission and signal re-absorption cross-sections of two lasing levels, ${}^4F_{9/2} \leftrightarrow {}^6H_{13/2}$, in the Dy^{3+} ion, calculated by our numerical method, (right) emission and signal re-absorption cross sections of ${}^4F_{9/2} \leftrightarrow {}^6H_{13/2}$ transition of the Dy^{3+} ion, calculated from measured fluorescence data for a fiber sample with CW pumping at 447 nm [46].

emitting at 447 nm, which excites the ground-state (${}^6H_{13/2}$) Dy^{3+} ions to the ${}^4I_{15/2}$ level as shown in Figure 4.17. Additionally, the signal re-absorption cross-section has been calculated using the measured emission cross-section and the McCumber relation [46].

The structural and physical parameters of the Dy−doped ZBLAN fiber are listed in Tables 4.2 and 4.3, where σ_{abp} is the absorption cross section at the pump wavelength λ_p, σ_{abs} and σ_{ems} are the re-absorption and emission cross sections at the signal wavelength λ_s, τ_{32}, and τ_{21}, τ_{30}, and τ_{10} are the energy level lifetimes. The parameters R_1, R_2, R_3, and R_4 are the reflectivity of input and output mirrors for the signal (laser) and pump wavelengths. For the linear cavity fiber laser considered in this work, the input mirror has reflectivity R_1, and the output mirror has reflectivity R_2 at the signal or laser wavelength. Both mirrors are considered to be transparent at the pump wavelength (R_3 = R_4= 0) so that the pump has only one pass through the fiber. Most of these parameters have been chosen similarly to the Dy−doped ZBLAN fiber theoretically and experimentally examined in [45, 46].

Table 4.2: Structural parameters of the investigated Dy−doped ZBLAN fiber laser.

Structural Parameter	Value
NA	0.16
d_{core}	12.5 μm
doping concentration, N_t	$3.66 \times 10^{25}\ m^{-3}$
Fibre Length, L	4 m
background loss	0.18 dB/m
R_1	90 %
R_2	50 %
R_3	0
R_4	0

As it has been reported in Table 4.2, the numerical aperture (NA) and core diameter of the fiber (d_{cor}) are 0.16 and 12.5 μm, respectively. These parameters guarantee single-mode operation down to 2.6 μm, so the fiber is multi-mode for both the pump and the lasing wavelengths (450 nm and 573 nm), as a consequence higher-order modes can be excited in the fiber core. This also affects the values of the overlap integrals of Γ_p and Γ_s, mentioned in Table 4.3. The values of 0.70 and 0.65 chosen here for Γ_p and Γ_s have been obtained based on the plenty of simulations run results and in comparison with other methods, fiber laser simulation software, and work in [85]. The radiative lifetime values τ_{21} and τ_{10} related to the level $^4F_{9/2}$ and $^6H_{13/2}$ respectively taken from the literature are 1.5 ms and 0.65 ms. On the other hand the nonradiative lifetime τ_{32} and τ_{30} are estimated to be respectively 100×10^{-6} s and 0.01 s. $A_{30} = 1/\tau_{30}$ indicates the spontaneous decay rate at the pump wavelength. It should be mentioned that the nonradiative lifetime of τ_{32} is much lower than that τ_{21}, related to the long-lived lasing level $^4F_{9/2}$.

4.3.2 FTCS Results

Although the yellow lasing transition shows a typical four-level nature, the experimental investigations have demonstrated the existence of excited-state absorption

Table 4.3: Physical parameters of the investigated Dy−doped ZBLAN fiber laser.

Physical Parameters	Value
λ_p	450 nm
λ_s	573 nm
σ_{abp}	$0.64 \times 10^{-25}\ m^2$
σ_{abs}	$0.70 \times 10^{-25}\ m^2$
σ_{ems}	$0.90 \times 10^{-25}\ m^2$
Γ_p	0.70
Γ_s	0.65
τ_{32}	100×10^{-6} s
τ_{21}	1.5×10^{-3} s
τ_{30}	0.01 s
τ_{10}	650×10^{-6} s

(ESA) from the lower laser level ($^6H_{13/2}$). Therefore, in the numerical FTCS model, the signal reabsorption cross-section is used to assess the impact of ESA and the development potential of this lasing transition for future demonstrations of Dy−doped yellow fiber lasers. We first simulated the normalized populations for all appropriate yellow laser levels along the fiber length. This has been performed by numerical analysis of rate Equations 3.1-3.6 reported in the previous chapter. Indeed, the normalized population distributions ($n_j = N_j/N_t$, j = 0-3, $N_t = N_0 + N_1 + N_2 + N_3$) for all appropriate yellow laser levels have been calculated by the FTCS method as a function of fiber length. The results have been shown in Figure 4.19. The population inversion between the lasing levels $^4F_{9/2}$ and $^6H_{13/2}$, along the fiber length, can be evaluated. Notice that the normalized population of $^4F_{9/2}$ level ($n_2 = N_2/N_t$) in the case of ESA is slightly higher than the one when ignoring the ESA. Consequently due to the coupled transitions among the other three levels, their population in the case of ESA is slightly decreased compared with the one ignoring the ESA. Furthermore, since the energy level $^4I_{15/2}$ is strongly non-radiatively coupled to the neighboring lower level $^4F_{9/2}$, the population of $^4I_{15/2}$ energy level is not significant.

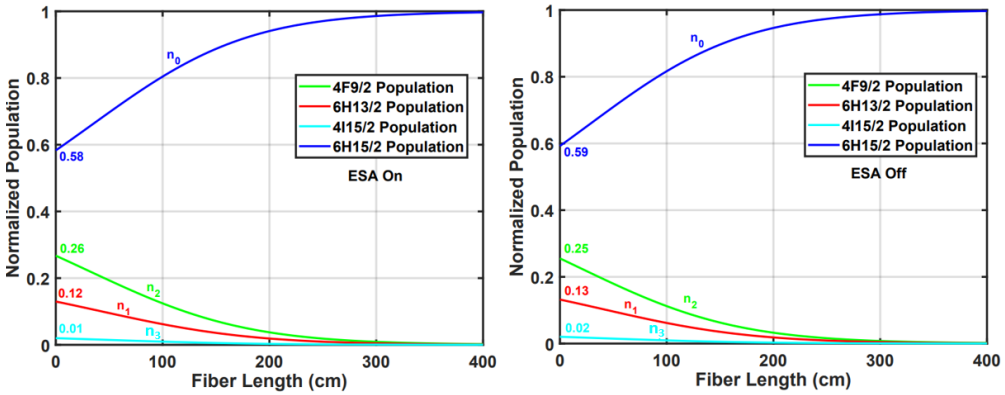

Figure 4.19: Normalized population distribution ($n_j = N_j/N_t$, j = 0-3) along the Dy−doped fiber length, (left) including the signal re-absorption (ESA on) and, (right) ignoring it (ESA off).

In our numerical analysis, we have secondly computed the optical pump and signal power evolution considering the impact of ESA, shown in Figure 4.20. It can be seen that ESA is considered, the signal power is amplified by the Dy−doped yellow fiber and reaches $\sim$ 148 mW from the initial value of the 107 mW. On the other hand, by ignoring the ESA (ESA off in Figure 4.20), further amplification of the signal at the end of the fiber is observed (reaching $\sim$ 173 mW from 107 mW at the beginning of fiber). A higher signal amplification in the case of ignoring the ESA has also been confirmed for a signal with an input power of 127 mW. This has been shown in Figure 4.21. Additionally, the pump output power is partially higher, or pump absorption decreases slightly when ESA is considered. This can be seen by analyzing the population evolution in the long-lived $^4F_{9/2}$ and $^6H_{13/2}$ levels. Because of the re-absorption of the intracavity yellow light from the excited $^6H_{13/2}$ level, the population in the upper $^4F_{9/2}$ lasing level increases. This leads to less effective pump absorption or slightly higher pump power at the end of the fiber.

The higher output signal or laser power in case of ignoring the ESA is due to its role as a source of loss. In other words, ESA occurs when an ion in the long-lived level is promoted to a higher energy level by absorbing either a pump or signal photon.

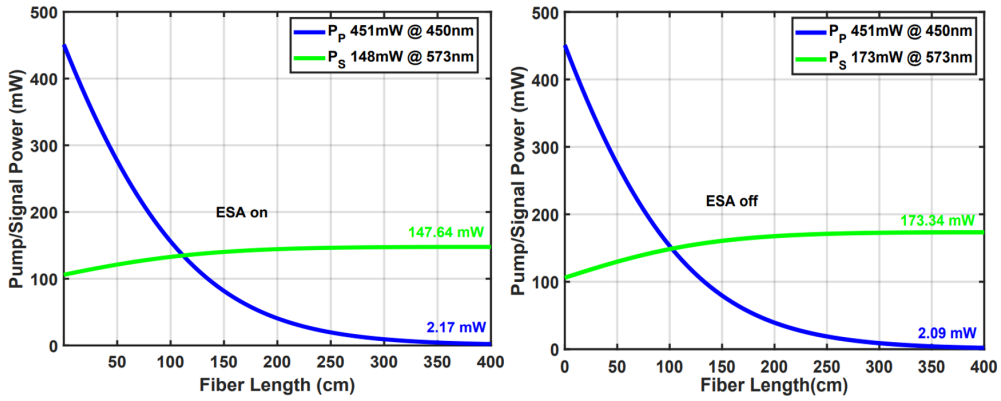

Figure 4.20: Pump and signal power evolution along the Dy−doped fiber for a forward propagating signal with an input power of 107 mW, (left) considering the signal re-absorption (ESA on), and (right) without considering the ESA (ESA off).

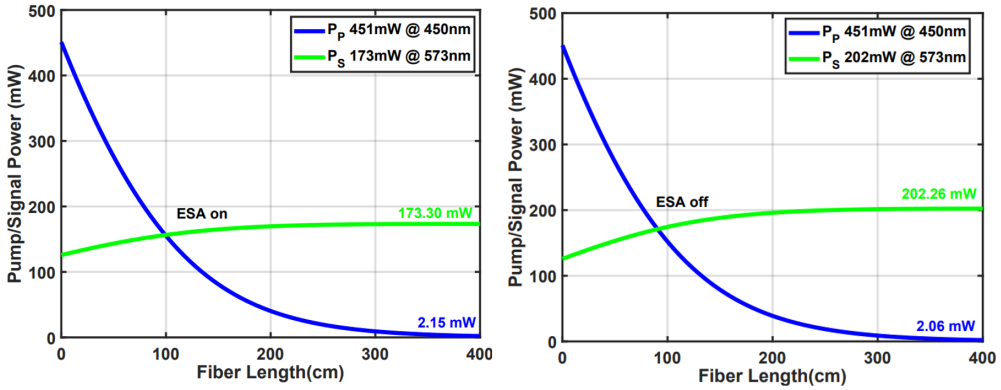

Figure 4.21: The same as Figure 4.20 with an input power of 127 mW.

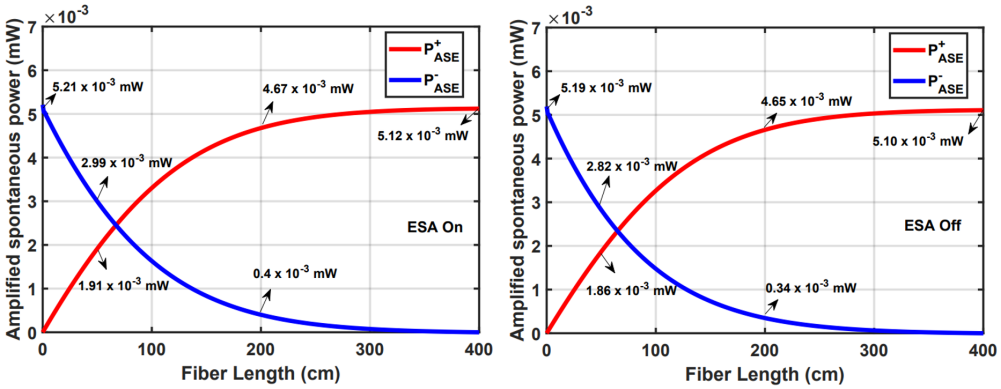

Figure 4.22: Forward and backward ASE power (respectively shown with P^{+}_{ASE} and P^{-}_{ASE}) evolution along the Dy−doped fiber for a forward propagating signal with an input power of 107 mW, (left) With ESA on, and (right) without considering the ESA.

The ion then returns to the long-lived level or ground-state level through phonon interactions and spontaneous emission so that ESA results in an effective loss [75]. It should be mentioned that the laser output power is calculated by multiplying the signal output power at the end of the fiber and the output mirror transmission. Since the output mirror reflectivity at signal wavelength is 50%, the output laser power previously reported is calculated to be 74 mW and 86.5 mW respectively with and without considering the ESA. It is worth mentioning that the calculated laser power of 74 mW, is in good agreement with the experimentally measured output power for a similar fiber laser investigated in [46].
We further analyzed the amplified spontaneous emission (ASE) both in forward and backward directions. This parameter has been calculated in the presence and absence of ESA in the emission wavelength spectrum (550-600 nm). The results in the case of the signal wavelength of Figure 4.20 and Figure 4.21 have been shown in Figure 4.22 and Figure 4.23.

It can be seen in Figure 4.22 that ESA has a partial effect on ASE power. Both the forward and backward ASE powers slightly decrease in case of ignoring ESA. This is predictable since by including the ESA, the population of the upper $^4F_{9/2}$

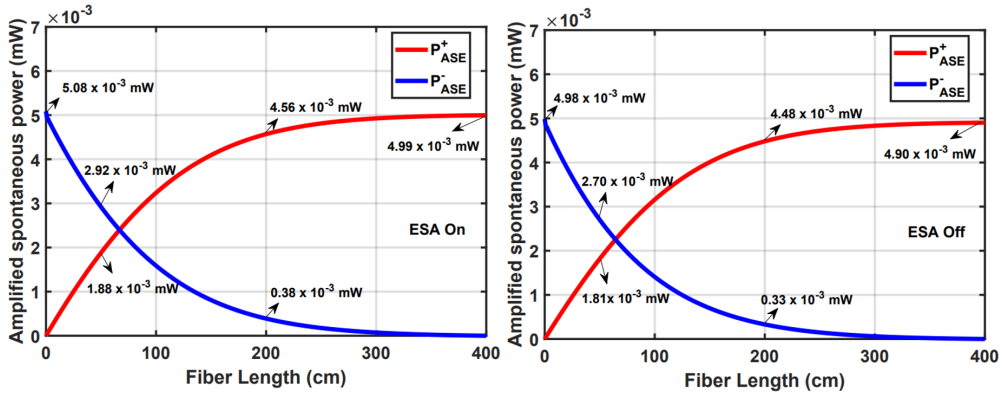

Figure 4.23: The same as Figure 4.22 with an input power of 127 mW.

lasing level increases. This, in turn, causes more ions available in the upper lasing level for ASE. When the signal input power is higher (Figure 4.23), the ASE powers are partially decreasing, and the impact of ESA is slightly greater. In Figures 4.22 and 4.23, P^{+}_{ASE} and P^{-}_{ASE} in three different positions along the fiber L = 0.5, 2, and 4 m, have been compared. Decreasing the power in case of ignoring the ESA, for a higher input power of signals is slightly more than the lower input power of the signal. The evolution of the ASE, signal, and pump power along the fiber length has been illustrated in Figure 4.24. It should be mentioned that the signal and pump power evolution in this Figure is consistent with the one in Figure 4.20.

Then gain parameter which is an important figure of merit for the Dy−doped fiber laser, is calculated. It is worth mentioning that the gain of the laser below the threshold, calculated here is based on an analytical method [86]. In that method, the obtained gain in the fiber length of L is given by

$$G = exp(\int_0^L g(z)dz) \tag{4.17}$$

where $g(z)$ is the local gain.

The dependence of the signal or lasing wavelength on pump conditions is investigated by considering the gain spectrum in the wavelength range of 565-590 nm. Several active fiber lengths L = 1-5 m and at different pump powers in the 226-541 mW range

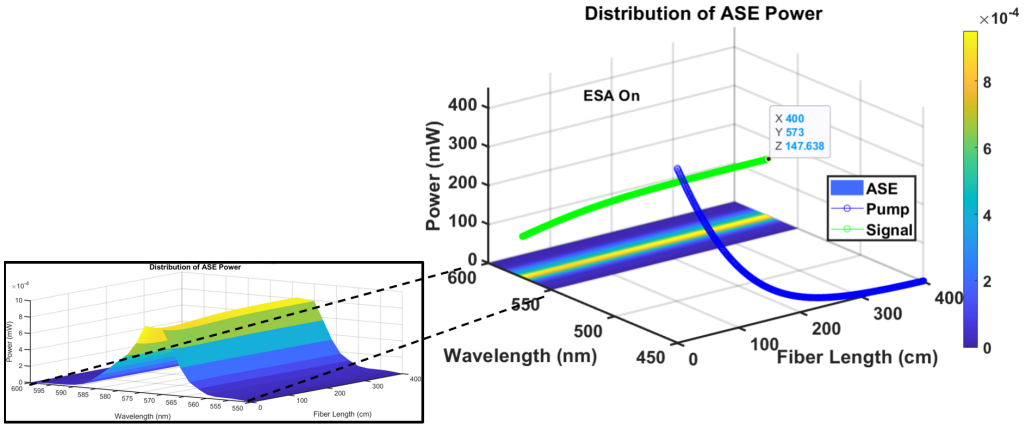

Figure 4.24: Distribution of the pump, signal, and ASE powers in terms of the wavelength and fiber length considering the ESA.

are investigated. For low pump power, the net gain first appears at longer wavelengths for which there is negligible reabsorption from the population in the lower level, as shown in Figure 4.25. As the pump power increases, the maximum gain moves progressively to shorter wavelengths. The highest gain of around 5 dB is found for a 2 m length of Dy−doped fiber pumped with 541 mW.

Finally, the FTCS model is employed to evaluate the effect of lifetime value changes in the four-level system of the Dy−doped fiber laser. Our simulations show that the two lifetimes that mainly affect the laser performance are τ_{30} and τ_{10}. Firstly the spontaneous decay time τ_{30} of the ${}^4I_{15/2}$ level is changed from 1-10^5 μs in two different conditions ESA on and ESA off. The impact of τ_{30} on the laser output power has been illustrated in Figure 4.26. It can be seen that changing the τ_{30} from 1 μs to 1000 μs causes an abrupt increase in the output power (from 52.5 mW to 72.5 mW). This is due to the decrease of the spontaneous decay rate A_{30}, thus improving the laser output performance. However, for τ_{30} values higher than 1000 μs, the output power slightly increases. This proves that the choice of $\tau_{30} = 10^4$ μs in our previous calculations is reasonable and reliable. When $\tau_{30} \geq 10^4$ μs, the output power increase is negligible, which means this parameter is no longer affecting the laser performance.

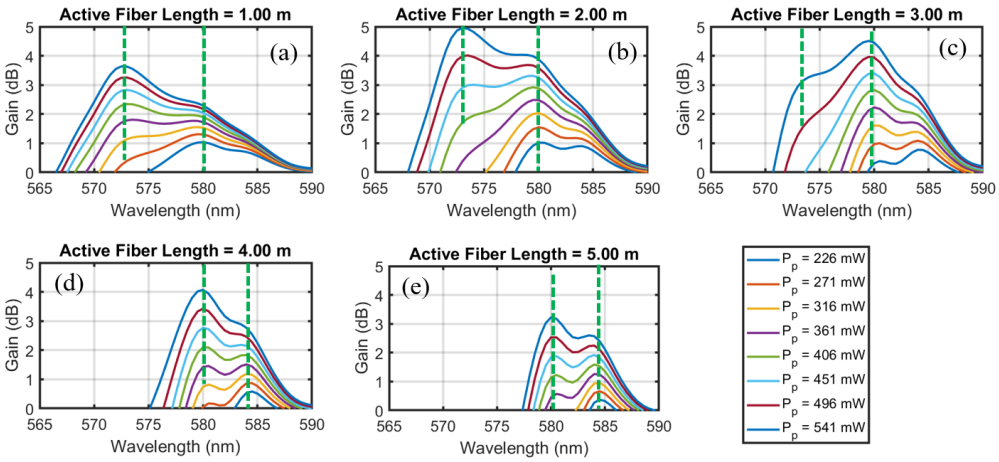

Figure 4.25: Gain for different fiber lengths of a) 1 m, b) 2 m, c) 3 m, d) 4 m, and e) 5 m, at eight different launched pump powers of 226, 271, 316, 361, 406, 451, 496, and 541 mW.

It should be mentioned that the observed behavior of the output power versus τ_{30}, in the case of ignoring ESA is the same as in the case with ESA. However, by ignoring the ESA, all the powers are shifted to a higher value for the case ESA on.

We also considered the effect of ESA on the laser output power. We decreased the τ_{10} value from 650 μs to 10^{-5} μs. At the lowest value of $\tau_{10} = 10^{-5}$ μs, the highest output power of 91.5 mW is obtained. Results have been shown in Figure 2.6. Notice that, by decreasing the lifetime τ_{10} of the lower laser level $^6H_{13/2}$, a higher output laser power is observed. Indeed, decreasing the τ_{10} value is equivalent to reducing the impact of the ESA, thus causing a faster depopulation of the lower level of the yellow laser transition ($^6H_{13/2}$), and consequently a higher pumping to the $^4I_{15/2}$ level and a higher laser output power. The same effect of decreasing τ_{10} in real conditions can be obtained by designing a cascade lasing arrangement in which the lower laser level of yellow transition is employed as the upper laser level of the mid-infrared one [46]. Generally speaking, the FTCS method, proposed and developed for the Dy−doped fiber laser, has been demonstrated to be able to evaluate the most essential parameters of the system. As we expressed, the population of the energy levels, power evolution,

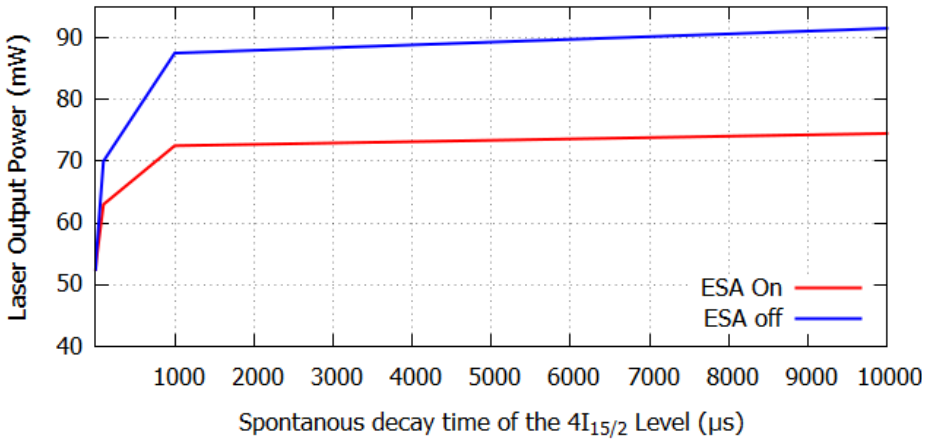

Figure 4.26: Output laser power versus of the spontaneous decay time of the ${}^4I_{15/2}$ level.

ASE, gain parameters, and time transition effects, have been fully described. The ESA phenomenon and its impact on the other system parameters have also been taken into account.

4.3.3 Laser efficiency

The schematic of the Dy−doped yellow fiber laser, modeled and discussed in this work, is shown in Figure 4.28. As can be seen, the laser cavity includes a few meter lengths of Dy−doped active fiber with light emission at 573 nm. The two input and output mirrors with reflectivity R_1 and R_2 at the lasing wavelength compose the linear cavity of the system. Both mirrors are transparent at the pump wavelength so that the pump has only one passe through the fiber ($R_3 = R_4 = 0$). A critical parameter of an optically pumped laser is its slope efficiency (η). The η is defined as the slope of the curve obtained by plotting the laser output (P_{Las}) power versus the pump power. In order to find the efficiency of the laser, first we need to find the pump power threshold P_{th}. At this power, the laser threshold is just reached, usually assuming steady-state conditions, and the small signal gain equals the losses of the laser cavity. Finally, the

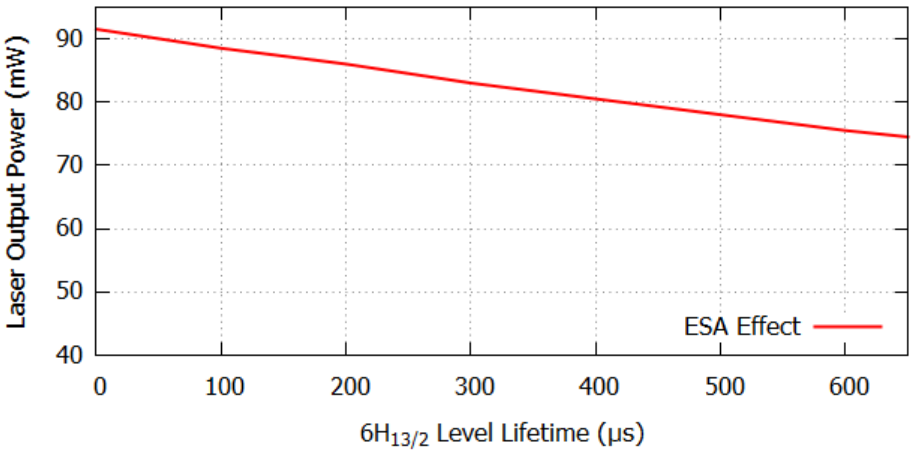

Figure 4.27: Output laser power versus the spontaneous decay time of the ${}^6H_{13/2}$ level.

output power of the laser with threshold pump power P_{th} for a given pump power P_p (above that threshold) can be calculated as follows

$$P_{Las} = \eta(P_p - P_{th}) \tag{4.18}$$

where P_p is the input pump power. Finding P_{th} can be approximately performed by analytical expressions. To obtain the P_{th} in the four-level system of Dy−doped fiber laser, we used the analytical method described in [75] using the intrinsic saturation powers, and cross-saturation powers at the pump and laser wavelengths.

To verify the correctness of this analytical method, we analyzed output power efficiency and pump threshold for different R_2 values similar to the experimental research in [46]. Therefore, different values of output mirror reflectivity R_2 = 50%, 58%, 74%, 86% equivalent to output coupler OC values of, respectively, 50%, 42 %, 26%, and 14%, have been chosen. The simulated laser slope efficiencies and thresholds with the mentioned values of R_2 (shown in Figure 4.29) have been calculated, which are in good agreement with their equivalent values experimentally obtained in [46].

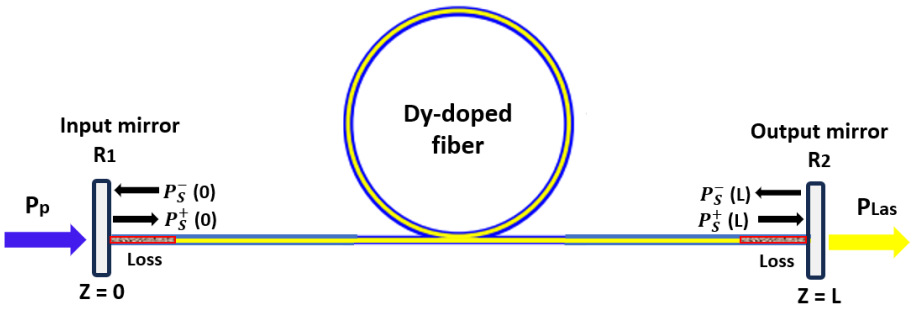

Figure 4.28: Schematic of the fiber laser setup. $P_s^+(z)$ and $P_s^-(z)$ are signal forward and backward propagating respectively in the positive and negative Z direction.

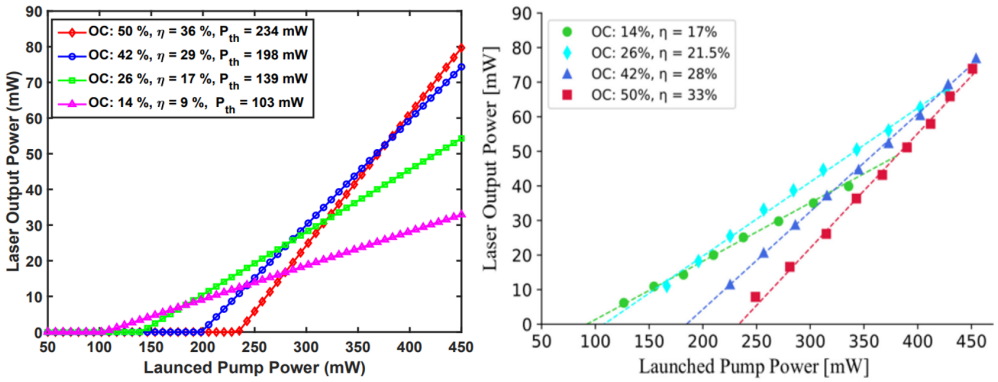

Figure 4.29: Yellow laser output power as a function of launched pump power at different output couplers (left) obtained with simulations, and (right) experimentally obtained in [46].

Regarding the observed curve in Figure 4.29, it should be mentioned that the pump power is related to the operational condition of the laser. Therefore, if the pump power is less than the threshold power, the output power of the laser is zero, and the population inversion linearly increases with the pump power. On the other hand, when the pump power is greater than the threshold power, the population inversion reaches the threshold and subsequently does not change, and the output power increases linearly with the pump power. The higher the pump power, the higher the stimulated emission rate, leading to an increase in the output power. Furthermore, as can be seen in Figure 4.29, the highest efficiency (36%), is related to the highest value of the *OC* that is 50% including the highest P_{th} (234 mW).

To accurately evaluate the impact of different structural and physical parameters on the performance of the laser, and to find the configurations providing the maximum possible slope efficiency, optimization simulations have been performed. In our analysis, the realistic values reported in Table 3.1 are considered. Firstly, we have changed the output mirror reflectivity from R_2 = 30% to R_2 = 90%. In Figure 4.30, the laser slope efficiency η and pump power threshold P_{th} values versus the output mirror reflectivity R_2 are shown. As it is shown in Figure 4.30, the laser efficiency has the maximum value $\eta \sim 65\%$, for the mirror reflectivity $R_2 = 30\%$. However, at this value of R_2, P_{th} is relatively high (P_{th} = 357 mW).

4.3.4 Overlap Integrals

We also simulated laser slope efficiencies and thresholds for different values of signal (Γ_s) and pump (Γ_p) overlap integrals. Since the fiber simulated here is multimode for both the laser and pump wavelength, different lasing and pump modes with different values of overlap integrals might be used in the lasing process. Results obtained by changing Γ_s and Γ_p have been illustrated in Figures 4.31 and 4.32. First, we calculated slope efficiencies and thresholds at a fixed Γ_p = 0.70 by changing Γ_s in the range 0.35-0.65. Second, we calculated slope efficiencies and thresholds at a fixed Γ_s = 0.65 by changing Γ_p in the range 0.65-0.95.

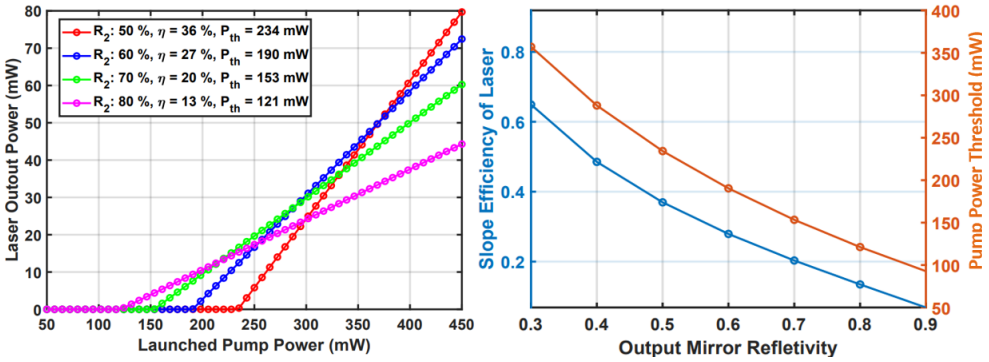

Figure 4.30: (left) Yellow laser output power as a function of launched pump power at different output mirror reflectivity of 50-80 % and (right) calculated values of slope efficiency and pump power threshold for reflectivity in the range of 30-90%.

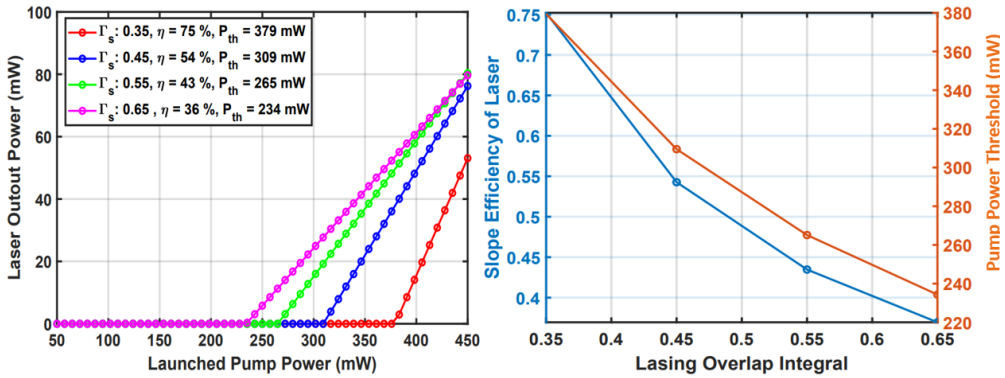

Figure 4.31: (left) Yellow laser output power as a function of launched pump power for different lasing overlap integrals of 0.35-0.65 and (right) calculated values of slope efficiency and pump power threshold versus the signal overlap integral.

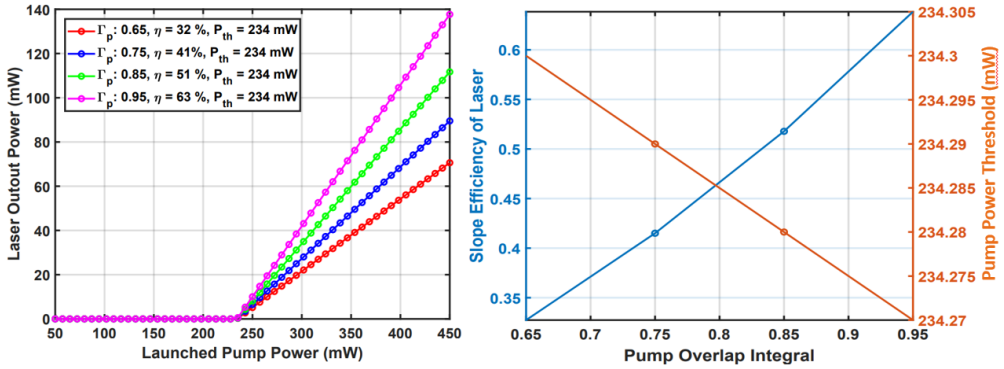

Figure 4.32: (left) Yellow laser output power as a function of launched pump power for different pump overlap integrals of 0.65-0.95 and (right) calculated values of slope efficiency and pump power threshold versus the pump overlap integrals.

4.3.5 Active fiber length

Finally, we evaluate the impact of different active fiber lengths on the laser output performance being the fiber the active medium. As can be seen in Figure 4.33, fiber length is changed from 0.5 m to 4 m. We figured out that the maximum achievable slope efficiency is $\eta \sim 78\%$ for the fiber length $L = 8.5$ m.

4.4 Discussions

The performance of a Dy−doped fiber laser with yellow emission at 573 nm has been analyzed. The Dy−doped fiber simulated in this study has the same characteristics as the commercially available Dy−doped fiber made by the Le Verre Fluoré, France [49]. Two different numerical and analytical approaches are chosen to fully understand the different transitions involved in the lasing mechanism of the fiber and their impact on the laser output performance. Having solved the rate and propagation equations for a four-level Dy−doped fiber laser using the FTCS method, the effect of ESA and ASE on the output power of the laser has been analyzed. ESA has a significant impact on the laser performance. By increasing the transition rate A_{10}, the

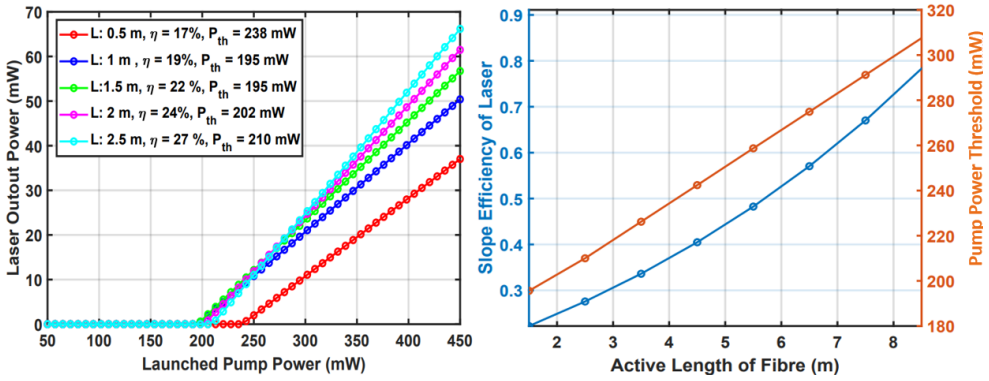

Figure 4.33: (left) Yellow laser output power as a function of launched pump power for different active fiber lengths of 0.5-2.5 m and (right) calculated values of slope efficiency and pump power threshold versus the active fiber lengths.

ESA impact on laser output power is decreased. As can be seen in Figure 4.27, decreasing τ_{10} from 650 μs to 10^{-5} μs, provides an increase of the output power from 74.5 mW to 91.5 mW. Then, further possible changes in laser output power have been predicted by changing the transition rate A_{30} in the fiber laser system. For τ_{30} values higher than 1000 μs, the effect of the pump spontaneous decay is negligible. Hence the output laser power slightly changes.

In Figures 4.30-4.33, pump threshold and laser slope efficiency changes are examined under the variation of four different parameters, that is R_2, Γ_s, Γ_p, and L. First, the pump threshold and slope efficiency have been calculated in the R_2 range 30-90% with a step of 10%. By decreasing the output mirror reflectivity from 50% to 30%, the slope efficiency increases from 36% to 65%. However, the pump power threshold has been also increased from 234 mW to 357 mW which is not desirable. Secondly, we have calculated the output power of the laser, the slope efficiency, and its threshold by changing Γ_s and Γ_p in the ranges, respectively, 0.35-65 and 0.65-0.95 by a step of 0.10. Similar to the impact of R_2, reducing the lasing overlap integral to 0.35 has provided a high slope efficiency of 75% and an increased pump threshold of 379 mW. On the other hand, increasing Γ_p from 0.70 to 0.95 not only will improve the slope

efficiency to 63%, but also the pump threshold remains as low as 234 mW. Nevertheless, Γ_s and Γ_p values for the chosen Dy−doped fiber simulated in this analysis, can not be far apart. In other words, comprise condition of high efficiency and low pump power threshold, can occur when Γ_s and Γ_p are in the range of 0.65-0.85. Finally, by increasing the active fiber length to 8.5 m, the highest η of 78% is achieved while the pump threshold is still relatively low (307 mW). It is worth mentioning that by increasing the active fiber length in the range of 4.5-8.5 m optimized performance of fiber laser can be obtained with a trade-off between the high output efficiency and low pump power threshold. In this range of fiber length slope efficiencies, more than half of the Stokes limit (of 78%) in the range of 40-78% are predicted with low pump power thresholds in the range of 242-307 mW. As a final remark, it should be mentioned that the heat effects in laser efficiency have not been considered, since the yellow laser discussed here is optimized for ophthalmology applications that do not need high power. Therefore the heat effects are not important and effective in the system performance.

Chapter 5

Cell Irradiation by a visible laser

5.1 Experiment description

Alongside our studies about the biomedical application of yellow lasers, we conducted some experiments in which dentary cells were exposed to the radiation of a He-Ne laser at 633 nm wavelength.
These activities have been carried on in the framework of the "Programma Nazionale di Ricerca e Progetti di Rilevante Interesse Nazionale (PRIN)" – Bando PRIN 2020 Yellow Flicker" at the University of Modena and Reggio Emilia, in collaboration with Prof. Laura Bertoni, Department of Surgery, Medicine, Dentistry and Morphological Sciences.
Although in these experiments a red-light laser, was used, the results can still help realize the effect of visible lasers on cells. In other words, the irradiation of any biological system generates a succession of processes that can be grouped into physical, physical-chemical, and biological phases, all characterized by specific events occurring at different times. The most important task of radiobiology is to evaluate the effects that may occur in the weeks, months, and years after radiotherapy. In this way, we would be able to propose improvements to current therapies.

5.1.1 The setup

We used a He-Ne laser at 633 nm with an average power of 6 mW. The intrinsic laser spot size radius is 0.6 mm. We aimed to irradiate the cells implanted in 48-multiwell cell culture plates with a diameter of 1.2 cm. To cover the whole cells inside the 48-well plate, we used a magnifying lens. After that, the pulse radiation was obtained by passing the laser light through a mechanical chopper. The set-up has been shown in Figure 5.1. As can be seen, all the experiments have been done inside the incubator to keep cells under viable conditions. We conducted the experiments in 4 different time exposures of 2-4 min to laser and 2 different frequencies of 250 and 500 Hz.

We irradiated 14 wells in two different seeding cell densities of 10,000 DPSCs/cm^2 and 20,000 DPSCs/cm^2. DPSC stands for Dental pulp-derived stem cells. These two different sets of cells have been shown in Figure 5.2. As can be seen in the up part of this Figure, the cells first are in their own cell growth media. Then for running the laser exposure experiments, they will be diluted in PBS ambient (shown in the down part of the Figure).

5.2 Results

Having irradiated cells, after a few days, cell viability is going to be evaluated. A variety of methods such as methods including the measurement of the overall DNA content, LDH release from cells, incorporation of bromodeoxyuridine or of thymidine analogs during DNA synthesis, the measurement of specific proteins involved in apoptosis, and measurement of the cell metabolic activity like oxidoreductase activity or ATP levels [87]. Each of these methods has advantages and disadvantages (Protocols and Applications Guide). Here in this work, cell viability is examined by MTT assay. The MTT assay measures cellular metabolic activity as an indicator of cell viability, proliferation, and cytotoxicity. This colorimetric assay is based on the reduction of a yellow tetrazolium salt (3-(4,5-dimethylthiazol-2-yl)-2,5-diphenyltetrazolium bromide or MTT) to purple formazan crystals by metabolically active cells. The viable cells contain NAD(P)H-dependent oxidoreductase enzymes which reduce the MTT to formazan. The insoluble formazan crystals are dissolved

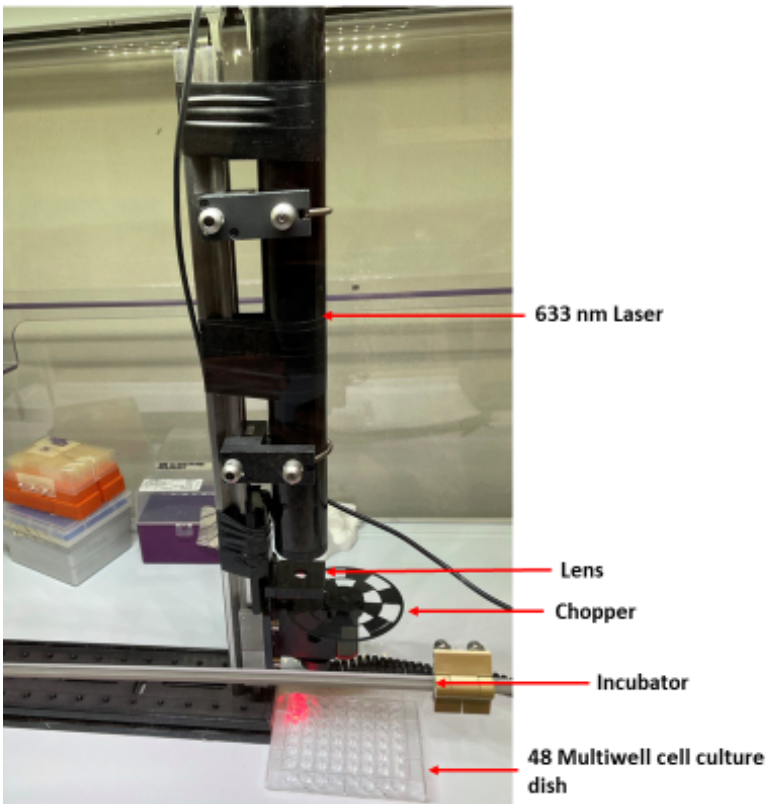

Figure 5.1: The laser setup includes the chopper, magnifying lens, and mechanical stages for cell irradiation.

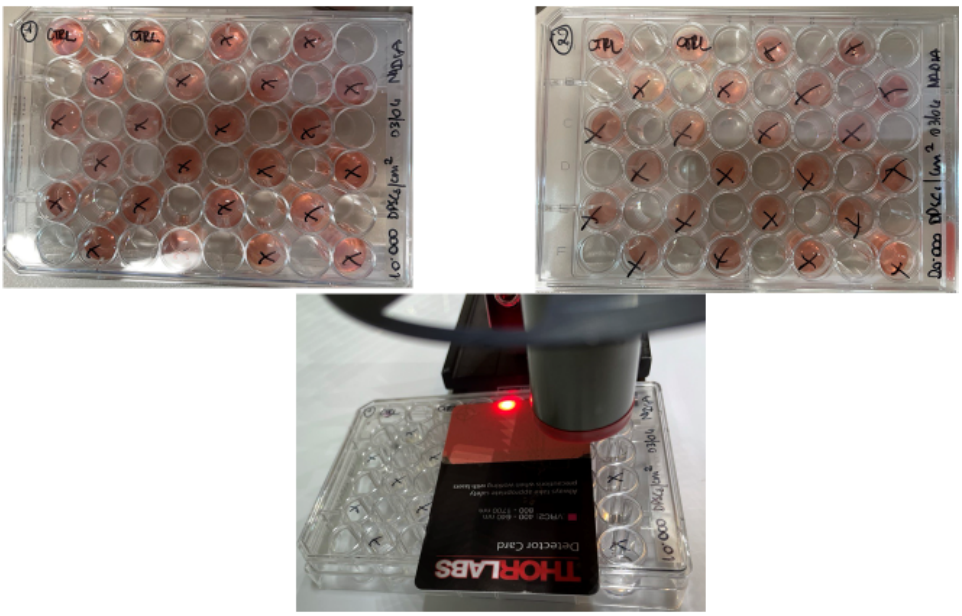

Figure 5.2: The cell culture plates with two densities of 10,000 DPSC/cm^2 (up, right), and 20,000 DPSC/cm^2 (up, left), in their growing medium. Then the cells were diluted in PBS buffer for irradiation experiments (down, center).

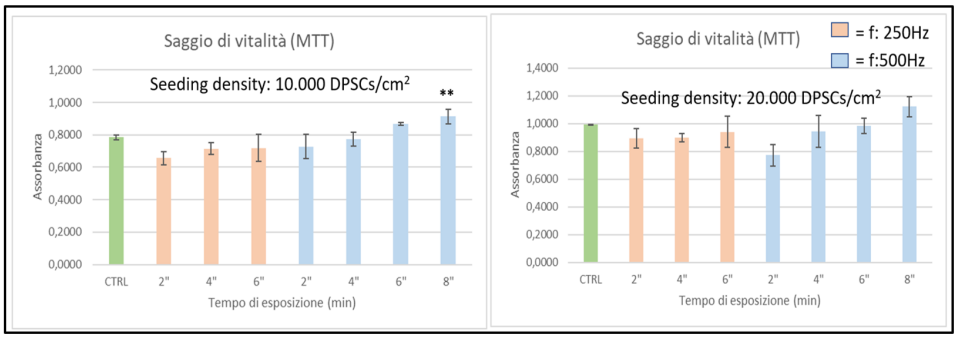

Figure 5.3: The MTT results in two different seeding cell densities of 10,000 DPSC/cm^2 (up, right), and 20,000 DPSC/cm^2 (up, left), in their growing medium.

using a solubilization solution and the resulting colored solution is quantified by measuring absorbance at 500-600 nanometers using a multi-well spectrophotometer. The darker the solution, the greater the number of viable cells. The results of this assay in the case of our experiments, have been illustrated in Figure5.3. As can be seen in this Figure, compared to the control cells without irradiation (CTRL, shown in green), the cells have viability after irradiation. These preliminary results confirm the viability of the oral cells under irradiation of the visible laser which can be promising in therapies improvement technology. More experiments on cell irradiation are still in progress.

Chapter 6

Conclusions

6.1 Conclusion of the First Part

In the first two chapters of the thesis, we dealt with HC-IC fibers as DNA-detection sensors. Two different kinds of HC fibers, TL and KL, were employed for conducting the experiments. Both of the HCF-based biosensing platforms were demonstrated suitable and reliable for the detection of DNA molecules. The red-wavelength spectral shifts before and after the formation of the protein molecule layers prove the detection of the DNA molecules. A modified functionalization process was performed. This five-step functionalization process of the fiber's internal surfaces has been developed to increase the sensitivity and reliability of the detection. In particular, infiltration of the fiber with ethanolamine in TRIS base (pH:9) solution, has enhanced the possibility of DNA binding and final detection of streptavidin. The use of streptavidin in the final step makes the bio-layer thicker, and thus, easier the detect. Despite plenty of infiltrations, no inner fiber structure breaking has been observed. This guarantees the resilience of the internal miniaturized structure of the fiber for bio/chemical applications in fluid environments. The reliability of the results has also been confirmed throughout the multiple repetitions of the infiltration process and optical measurements. The wavelength shifts of 1.83–3.81 nm, 2.84–5.76 nm, and 9.82–17.92 nm in three wavelength ranges of, respectively, 500–540 nm, 729–805 nm and 1277–1645

nm were measured in the case of TLF. This reveals the flexibility of the HC-TLF-biosensor in biomolecule detection in a wide range of applications and its compatibility with numerous optical components and laser sources. Other advantages of the examined biosensor are the simple optical measurements, robustness to the excitation mode, and freedom from any extra reinforced techniques for molecule detection. This biosensor with an unprecedented light-waveguiding mechanism and operating principle, though only tested using standard pure samples, could show promising results for ultra-sensitive detection of the thinner bio-layers including breast cancer molecules in the lab-in-fiber platform. Further studies to assess sensitivity to target interfering biomolecules are needed to fully develop the present method into analytical or clinical applications. As a final remark it's worth noting that here, in this thesis, we have described the first demonstration of the changes in HC-TLF and KLF upon DNA capture and subsequent decoration with streptavidin through a PNA-signalling probe. The work aimed to show that the derivatization of the surface with PNA capture probes is feasible and that an appropriate sensing format can be used to generate an optical signal detectable in the fiber transmission spectrum. The method was found to be reproducible and can subsequently be extended to quantitative measurements.

6.2 Conclusion of the Second Part

In Chapters 3 and 4 yellow fiber lasers were discussed. Notice that developing fiber laser systems relying on just experimental work is inefficient and inadequate. Additionally, the current progress of fiber lasers and amplifiers requires accurate and simple theoretical or numerical modeling of the system. Analysis and simulation of the fiber amplifier and laser systems require the solution of two groups of equations. It is necessary to solve the rate equations for the active medium. The second group of equations is the propagation equations consisting of several coupled non-linear first-order ordinary differential equations (ODE) which describe the propagation of the optical fields inside the cavity. In chapters 3 and 4 of this thesis, the FTCS method for solving the rate and propagation equations of rare-earth-based fiber laser systems is proposed and then extended to the four-level system of $Dy-$doped yellow fiber

laser. In other words, the FTCS numerical method and the analytical approach have been developed to fully evaluate the performance of the Dy−doped fiber laser. Two sources of loss, ESA and ASE, have been taken into account in the model. The influence of the ESA loss on laser output power can be significantly reduced by decreasing τ_{10} to 10^{-5} μs. Exploiting the developed analytical approach for the four-level system of Dy−doped fiber laser, the impact of fiber cavity parameters on the slope efficiency and pump power threshold was investigated. Optimized criteria for finding a Dy−doped yellow fiber laser with high efficiency have been found. The found criteria are output mirror reflectivities less than 50%, lasing overlap integrals less than 0.65, pump overlap integrals higher than 0.75, and finally, fiber length longer than 4.5 m, to obtain $\eta \geq 36\%$. The slope efficiency reported in this work is higher than other values reported in the literature for the same fiber [45, 46]. Additionally, the fiber length parameter is the most effective in achieving efficient Dy−doped fiber yellow fiber lasers. Choosing the active fiber length in the range of 4.5-8.5 m could provide the optimized performance of fiber laser with a trade-off between the high output efficiency and low pump power threshold. In this range of fiber length, slope efficiencies more than half of the Stokes limit, in the range of 40-78% are predicted with low pump power thresholds in the range of 242-307 mW.

As a final remark, it should be mentioned that cell irradiation experiments described in Chapter 5, are one of the crucial technological steps in improving current therapies. In this study, using a 633 He-Ne laser, preliminary results on the oral cell irradiation grown in the 48-well plates were reported. These preliminary results confirmed the viability of the oral cell irradiation with visible laser which can be promising in the improvement of visible light-based technologies for therapies.

List of Publications

The results of the activities during the PhD are reflected in the following articles.

- Khozeymeh Sarbishe, F., Selleri, S., Hamzeh, G., and Razaghi, M. A highly sensitive ring resonator sensor based on subwavelength grating waveguides for biosensing applications. In Proc. of SPIE Vol (Vol. 11786, pp. 117861L-1).
- Giovanardi, F., Khozeymeh, F., Bissoli, F., Rampino, S., Gilioli, E., Trevisi, G., and Selleri, S. (2021, June). Laser scribing of Sb2Se3 thin-film solar cells. In The European Conference on Lasers and Electro-Optics (p. cm-p-36). Optica Publishing Group.
- Khozeymeh, F., Melli, F., Capodaglio, S., Corradini, R., Benabid, F., Vincetti, and L., and Cucinotta, A. (2022, June). A microstructured fiber for streptavidin detection. In 2022 Italian Conference on Optics and Photonics (ICOP) (pp. 1-3). IEEE.
- Khozeymeh, F., Poli, F., and Razaghi, M. (2022, June). Analysis of a silicon subwavelength grating ring resonator as a refractometric sensor. In 2022 Italian Conference on Optics and Photonics (ICOP) (pp. 1-3). IEEE.
- Khozeymeh, F., Melli, F., Capodaglio, S., Corradini, R., Benabid, F., Vincetti, L., and Cucinotta, A. Hollow-core fibers for biological sensing application, XXIV Riunione Nazionale di Elettromagnetismo, Catania, 18-21 September 2022.

- Khozeymeh, F., Melli, F., Capodaglio, S., Corradini, R., Benabid, F., Vincetti, L., and Cucinotta, A. (2022). Hollow-Core Fiber-Based Biosensor: A Platform for Lab-in-Fiber Optical Biosensors for DNA Detection. Sensors, 22(14), 5144.

- Serafini, V., Pugliese, D., Bellone, A., Lousteau, J., Sarbishe, F. K., Poli, F., Perrone, G. (2023, March). Toward the development of direct emission yellow fiber lasers for biomedical applications. In Optical Fibers and Sensors for Medical Diagnostics, Treatment and Environmental Applications XXIII (Vol. 12372, p. 1237202). SPIE.

- Khozeymeh, F., Poli, F., Serafini, Perrone, G. and Cucinotta, A., DESIGN AND MODELLING OF YELLOW FIBRE LASERS FOR OPHTHALMOLOGY APPLICATIONS, 3rd International Conference on Dielectric Photonic Devices and Systems Beyond Visible (D-Photon 2023), Bari, 11-13 July 2023, (Best conference paper award).

- Khozeymeh, F., Poli, F., Chowdhury, W., and Cucinotta, A. (2023). Analysis and optimization of Dysprosium-doped yellow fiber lasers for ophthalmology applications. IEEE Photonics Journal.

Bibliography

[1] Amanda J Haes, Lei Chang, William L Klein, and Richard P Van Duyne. Detection of a biomarker for alzheimer's disease from synthetic and clinical samples using a nanoscale optical biosensor. *Journal of the American Chemical Society*, 127(7):2264–2271, 2005.

[2] Nishtha Khansili, Gurdeep Rattu, and Prayaga M Krishna. Label-free optical biosensors for food and biological sensor applications. *Sensors and Actuators B: Chemical*, 265:35–49, 2018.

[3] Harish Kumar and Renu Rani. Development of biosensors for the detection of biological warfare agents: its issues and challenges. *Science Progress*, 96(3):294–308, 2013.

[4] Maria Teresa Giardi, Viviana Scognamiglio, Giuseppina Rea, Giuseppe Rodio, Amina Antonacci, Maya Lambreva, Gianni Pezzotti, and Udo Johanningmeier. Optical biosensors for environmental monitoring based on computational and biotechnological tools for engineering the photosynthetic d1 protein of chlamydomonas reinhardtii. *Biosensors and Bioelectronics*, 25(2):294–300, 2009.

[5] David L Andrews. *Photonics, Volume 4: Biomedical Photonics, Spectroscopy, and Microscopy*. John Wiley & Sons, 2015.

[6] Jeffrey D Newman and Anthony PF Turner. Biosensors: principles and practice. *Essays in biochemistry*, 27:147–159, 1992.

[7] Giuliano Zanchetta, Roberta Lanfranco, Fabio Giavazzi, Tommaso Bellini, and Marco Buscaglia. Emerging applications of label-free optical biosensors. *Nanophotonics*, 6(4):627–645, 2017.

[8] Eden Morales-Narváez and Arben Merkoçi. Graphene oxide as an optical biosensing platform: a progress report. *Advanced materials*, 31(6):1805043, 2019.

[9] Pedro Chamorro-Posada. Asymmetric concentric microring resonator label-free biosensors. In *Photonics*, volume 9, page 27. Multidisciplinary Digital Publishing Institute, 2022.

[10] Foroogh Khozeymeh and Mohammad Razaghi. Cylindrical optical resonators: fundamental properties and bio-sensing characteristics. *Journal of Optics*, 20(4):045301, 2018.

[11] F Khozeymeh and M Razaghi. Parallel-coupled dual si o x n y racetrack resonators as biosensors with high improved intrinsic limit of detection. *Physical Review Applied*, 12(5):054045, 2019.

[12] Foroogh Khozeymeh and Mohammad Razaghi. Crystalline mgf2 whispering gallery mode resonators as optical refractometric sensors with ultra-high improved sensitivity. *IEEE Sensors Journal*, 2019.

[13] Foroogh Khozeymeh, Mohammad Razaghi, Tatevik Chalyan, and Lorenzo Pavesi. Fast analytical modelling of a soi micro-ring resonator for bio-sensing application. *Journal of Physics D: Applied Physics*, 2018.

[14] F Khozeymeh and M Razaghi. Sensitivity optimization in whispering gallery mode optical cylindrical biosensors. In *Journal of Physics: Conference Series*, volume 956, page 012008. IOP Publishing, 2018.

[15] Linh Viet Nguyen, Kelly Hill, Stephen Warren-Smith, and Tanya Monro. Interferometric-type optical biosensor based on exposed core microstructured optical fiber. *Sensors and Actuators B: chemical*, 221:320–327, 2015.

[16] Xianxin Jiang, Yangqing Chen, Fang Yu, Longhua Tang, Mingyu Li, and Jian-Jun He. High-sensitivity optical biosensor based on cascaded mach–zehnder interferometer and ring resonator using vernier effect. *Optics letters*, 39(22):6363–6366, 2014.

[17] Brian Cunningham, Jean Qiu, Peter Li, and Bo Lin. Enhancing the surface sensitivity of colorimetric resonant optical biosensors. *Sensors and Actuators B: Chemical*, 87(2):365–370, 2002.

[18] Foroogh Khozeymeh and Mohammad Razaghi. Characteristics optimization in single and dual coupled silicon-on-insulator ring (disk) photonic biosensors. *Sensors and Actuators B: Chemical*, 281:998–1008, 2019.

[19] Sahba TalebiFard, Shon Schmidt, Wei Shi, WenXuan Wu, Nicolas AF Jaeger, Ezra Kwok, Daniel M Ratner, and Lukas Chrostowski. Optimized sensitivity of silicon-on-insulator (soi) strip waveguide resonator sensor. *Biomedical optics express*, 8(2):500–511, 2017.

[20] Ana Belén González-Guerrero, Jesús Maldonado, Sonia Herranz, and Laura M Lechuga. Trends in photonic lab-on-chip interferometric biosensors for point-of-care diagnostics. *Analytical methods*, 8(48):8380–8394, 2016.

[21] Armando Ricciardi, Alessio Crescitelli, Patrizio Vaiano, Giuseppe Quero, Marco Consales, Marco Pisco, Emanuela Esposito, and Andrea Cusano. Lab-on-fiber technology: a new vision for chemical and biological sensing. *Analyst*, 140(24):8068–8079, 2015.

[22] Xuan Yang, Chao Shi, Rebecca Newhouse, Jin Z Zhang, and Claire Gu. Hollow-core photonic crystal fibers for surface-enhanced raman scattering probes. *International Journal of Optics*, 2011, 2011.

[23] Ruhallah Nasirifar, Mohammad Danaie, and Abbas Dideban. Hollow-core graded index optical fiber refractive index sensor based on surface plasmon resonance. *Optical and Quantum Electronics*, 52(7):1–23, 2020.

[24] Enrico Coscelli, Michele Sozzi, Federica Poli, Davide Passaro, Annamaria Cucinotta, Stefano Selleri, Roberto Corradini, and Rosangela Marchelli. Toward a highly specific dna biosensor: Pna-modified suspended-core photonic crystal fibers. *IEEE Journal of selected topics in quantum electronics*, 16(4):967–972, 2009.

[25] Fabio Giovanardi, A Cucinotta, and Luca Vincetti. Inhibited coupling guiding hollow fibers for label-free dna detection. *Optics express*, 25(21):26215–26220, 2017.

[26] Luca Vincetti and Valerio Setti. Waveguiding mechanism in tube lattice fibers. *Optics express*, 18(22):23133–23146, 2010.

[27] Fabio Giovanardi, Annamaria Cucinotta, Andrea Rozzi, Roberto Corradini, Fetah Benabid, Lorenzo Rosa, and Luca Vincetti. Hollow core inhibited coupling fibers for biological optical sensing. *Journal of Lightwave Technology*, 37(11):2598–2604, 2019.

[28] Alexander Maninagat Luke, Simy Mathew, Maram Majed Altawash, and Bayan Mohammed Madan. Lasers: A review with their applications in oral medicine. *Journal of lasers in medical sciences*, 10(4):324, 2019.

[29] T Omatsu, A Lee, HM Pask, and J Piper. Passively q-switched yellow laser formed by a self-raman composite nd: Yvo 4/yvo 4 crystal. *Applied Physics B*, 97:799–804, 2009.

[30] Yasushi Fujimoto, Osamu Ishii, and Masaaki Yamazaki. 575 nm laser oscillation in dy3+-doped waterproof fluoro-aluminate glass fiber pumped by violet gan laser diodes. In *Solid State Lasers XX: Technology and Devices*, volume 7912, pages 152–158. SPIE, 2011.

[31] Katsunari Okamoto. *Fundamentals of optical waveguides*. Academic press, 2010.

[32] Daniel Lavinsky, Jenny Wang, Philip Huie, Roopa Dalal, Seung Jun Lee, Dae Yeong Lee, and Daniel Palanker. Nondamaging retinal laser therapy: rationale and applications to the macula. *Investigative Ophthalmology & Visual Science*, 57(6):2488–2500, 2016.

[33] Tao Hong, Claire Cramer, Eryn Cook, Warren Nagourney, and EN Fortson. Observation of the s01–p03 transition in atomic ytterbium for optical clocks and qubit arrays. *Optics Letters*, 30(19):2644–2646, 2005.

[34] Lei Zhang, Huawei Jiang, Shuzhen Cui, Jinmeng Hu, and Yan Feng. Versatile raman fiber laser for sodium laser guide star. *Laser & Photonics Reviews*, 8(6):889–895, 2014.

[35] Kobi Aflalo, Moshe Ben-David, Adrian Stern, and Irit Juwiler. Theoretical investigation of using a yellow (577nm) laser for diabetic retinopathy. *OSA Continuum*, 3(11):3253–3266, 2020.

[36] NS Kapany, NA Peppers, HC Zweng, and M Flocks. Retinal photocoagulation by lasers. *Nature*, 199:146–149, 1963.

[37] Tommaso Verdina, Rossella D'Aloisio, Andrea Lazzerini, Cecilia Ferrari, Edoardo Valerio, Rodolfo Mastropasqua, and Gian Maria Cavallini. The role of subthreshold micropulse yellow laser as an alternative option for the treatment of refractory postoperative cystoid macular edema. *Journal of Clinical Medicine*, 9(4):1066, 2020.

[38] DW Coutts, MD Ainsworth, and JA Piper. Efficient green/yellow conversion of copper vapour laser output. *Optics communications*, 75(3-4):301–306, 1990.

[39] Jun Ota, Akira Shirakawa, and Ken-ichi Ueda. High-power yb-doped double-clad fiber laser directly operating at 1178 nm. *Japanese Journal of Applied Physics*, 45(2L):L117, 2006.

[40] Evgeny M Dianov, Alexey V Shubin, Mikhail A Melkumov, Oleg I Medvedkov, and Igor A Bufetov. High-power cw bismuth-fiber lasers. *JOSA B*, 24(8):1749–1755, 2007.

[41] Mahmoud Fallahi, Li Fan, Yushi Kaneda, Chris Hessenius, JÖrg Hader, Hongbo Li, Jerome V Moloney, Bernardette Kunert, Wolfgang Stolz, Stephan W Koch, et al. 5-w yellow laser by intracavity frequency doubling of high-power vertical-external-cavity surface-emitting laser. *IEEE Photonics Technology Letters*, 20(20):1700–1702, 2008.

[42] J Limpert, H Zellmer, P Riedel, and A Tünnermann. Laser oscillation in yellow and blue spectral range in dy3+: Zblan. In *Conference on Lasers and Electro-Optics*, page CWJ4. Optical Society of America, 2001.

[43] SR Bowman, S O'Connor, and NJ Condon. Diode pumped yellow dysprosium lasers. *Optics Express*, 20(12):12906–12911, 2012.

[44] Giacomo Bolognesi, Daniela Parisi, Davide Calonico, Giovanni Antonio Costanzo, Filippo Levi, Philip Werner Metz, Christian Kränkel, Günter Huber, and Mauro Tonelli. Yellow laser performance of dy 3+ in co-doped dy, tb: Liluf 4. *Optics Letters*, 39(23):6628–6631, 2014.

[45] MZ Amin, MR Majewski, and SD Jackson. Yellow emission from dysprosium-doped zblan fiber laser. In *Fiber Lasers XVII: Technology and Systems*, volume 11260, pages 197–203. SPIE, 2020.

[46] MZ Amin, SD Jackson, and MR Majewski. Experimental and theoretical analysis of dy 3+-doped fiber lasers for efficient yellow emission. *Applied Optics*, 60(16):4613–4621, 2021.

[47] Shuhang Tian, Yipeng Lun, Yongsheng Sun, Dongdan Chen, Guowu Tang, Qi Qian, and Zhongmin Yang. Silicate-clad dy3+ doped multi-component phosphate glass core glass fiber for yellow laser applications. *Journal of Non-Crystalline Solids*, 577:121313, 2022.

[48] Qianyi Chen, Minbo Wu, Puxian Xiong, Yajing Zhao, Shuhang Tian, Yao Xiao, Yongsheng Sun, Dongdan Chen, Shanhui Xu, and Zhongmin Yang. Efficient and broadband emission in dy3+-doped glass-ceramic fibers for tunable yellow fiber laser. *Nanomaterials*, 13(9):1558, 2023.

[49] https://leverrefluore.com/products/active-fibers/re-doped-single-mode-fiber.

[50] Jinhai Zou, Tianran Li, Yanbo Dou, Jin Li, Nan Chen, Yikun Bu, and Zhengqian Luo. Direct generation of watt-level yellow dy 3+-doped fiber laser. *Photonics Research*, 9(4):446–451, 2021.

[51] Johan Meyer, Justice Mpoyo Sompo, and Suné von Solms. *Fiber Lasers: Fundamentals with MATLAB® Modelling*. CRC Press, 2022.

[52] Matteo Barozzi, Alex Manicardi, Armando Vannucci, Alessandro Candiani, Michele Sozzi, Maria Konstantaki, Stavros Pissadakis, Roberto Corradini, Stefano Selleri, and Annamaria Cucinotta. Optical fiber sensors for label-free dna detection. *Journal of Lightwave Technology*, 35(16):3461–3472, 2016.

[53] F Couny, Fetah Benabid, PJ Roberts, PS Light, and MG Raymer. Generation and photonic guidance of multi-octave optical-frequency combs. *Science*, 318(5853):1118–1121, 2007.

[54] Sergey A Pidenko, Natalia A Burmistrova, Andrey A Shuvalov, Anastasiya A Chibrova, Yulia S Skibina, and Irina Y Goryacheva. Microstructured optical fiber-based luminescent biosensing: is there any light at the end of the tunnel?-a review. *Analytica chimica acta*, 1019:14–24, 2018.

[55] Patrick Uebel, Mehmet C Günendi, Michael H Frosz, Goran Ahmed, Nitin N Edavalath, Jean-Michel Ménard, and Philip St J Russell. Broadband robustly single-mode hollow-core pcf by resonant filtering of higher-order modes. *Optics letters*, 41(9):1961–1964, 2016.

[56] Anil Kumar Mudraboyina and Jayshri Sabarinathan. Protein binding detection using on-chip silicon gratings. *Sensors*, 11(12):11295–11304, 2011.

[57] Md Asaduzzaman Jabin, Yanhua Luo, Gang-Ding Peng, Md Juwel Rana, Kawsar Ahmed, Truong Khang Nguyen, Bikash Kumar Paul, and Vigneswaran Dhasarathan. Design and fabrication of amoeba faced photonic crystal fiber for biosensing application. *Sensors and Actuators A: Physical*, 313:112204, 2020.

[58] Alankar Shrivastava, Vipin B Gupta, et al. Methods for the determination of limit of detection and limit of quantitation of the analytical methods. *Chron. Young Sci*, 2(1):21–25, 2011.

[59] Alessandro Bertucci, Alex Manicardi, Alessandro Candiani, Sara Giannetti, Annamaria Cucinotta, Giuseppe Spoto, Maria Konstantaki, Stavros Pissadakis, Stefano Selleri, and Roberto Corradini. Detection of unamplified genomic dna by a pna-based microstructured optical fiber (mof) bragg-grating optofluidic system. *Biosensors and Bioelectronics*, 63:248–254, 2015.

[60] R Friedberg. Einstein and stimulated emission: A completely corpuscular treatment of momentum balance. *American journal of physics*, 62(1):26–32, 1994.

[61] Theodore H Maiman et al. Stimulated optical radiation in ruby. 1960.

[62] Joan Lisa Bromberg. The birth of the laser. *Physics today*, 41(10):26–33, 1988.

[63] Charles J Koester and Elias Snitzer. Amplification in a fiber laser. *Applied optics*, 3(10):1182–1186, 1964.

[64] Elias Snitzer and R Tumminelli. Sio 2-clad fibers with selectively volatilized soft-glass cores. *Optics letters*, 14(14):757–759, 1989.

[65] Susanne E McCoy. Copper bromide laser treatment of facial telangiectasia: results of patients treated over five years. *Lasers in Surgery and Medicine: The Official Journal of the American Society for Laser Medicine and Surgery*, 21(4):329–340, 1997.

[66] Xiaowei Huo, Yaoyao Qi, Yu Zhang, Bin Chen, Zhenxu Bai, Jie Ding, Yulei Wang, and Zhiwei Lu. Research development of 589 nm laser for sodium laser guide stars. *Optics and Lasers in Engineering*, 134:106207, 2020.

[67] Joanne WY Yau, Sophie L Rogers, Ryo Kawasaki, Ecosse L Lamoureux, Jonathan W Kowalski, Toke Bek, Shih-Jen Chen, Jacqueline M Dekker, Astrid Fletcher, Jakob Grauslund, et al. Global prevalence and major risk factors of diabetic retinopathy. *Diabetes care*, 35(3):556–564, 2012.

[68] Dianyuan Wang, Yanyan Guo, Guanghou Sun, Jie Li, Lei Zhao, and Gaoping Xu. Blue, green, yellow and red upconversion fluorescence in tm3+/ho3+: Cs2nagdcl6 crystals under 785 nm laser excitation. *Journal of alloys and compounds*, 451(1-2):122–124, 2008.

[69] Michel JF Digonnet. *Rare-earth-doped fiber lasers and amplifiers, revised and expanded*. CRC press, 2001.

[70] PW France. Optical fibre lasers and amplifiers, boca raton, 1991.

[71] CY Chen, MM Choy, MJ Andrejco, MA Saifi, and Chinlon Lin. A widely tunable erbium-doped fiber laser pumped at 532 nm. *IEEE Photonics Technology Letters*, 2(1):18–20, 1990.

[72] R Davey, N Langford, and AI Ferguson. Subpicosecond pulse generation from an erbium-doped fiber laser. In *Conference on Lasers and Electro-Optics*, page CFE2. Optical Society of America, 1991.

[73] Michel JF Digonnet. Closed-form expressions for the gain in three-and four-level laser fibers. *IEEE Journal of quantum electronics*, 26(10):1788–1796, 1990.

[74] Th Pfeiffer and H Bulow. Analytical gain equation for erbium-doped fiber amplifiers including mode field profiles and dopant distribution. *IEEE photonics technology letters*, 4(5):449–451, 1992.

[75] C Barnard, P Myslinski, J Chrostowski, and Mohsen Kavehrad. Analytical model for rare-earth-doped fiber amplifiers and lasers. *IEEE Journal of Quantum Electronics*, 30(8):1817–1830, 1994.

[76] Philippe M Becker, Anders A Olsson, and Jay R Simpson. *Erbium-doped fiber amplifiers: fundamentals and technology*. Elsevier, 1999.

[77] Stefano Selleri, Luca Vincetti, and Annamaria Cucinotta. *Optical and Photonic Components*. Società Editrice Esculapio, 2015.

[78] Fabrizio Di Pasquale, Alberto Gaibazzi, and Maurizio Zoboii. Analysis of erbium doped fiber amplifiers by combined runge-kutta and finite-element methods. *European Transactions on Telecommunications*, 4(3):355–363, 1993.

[79] Siamak Dawazdah Emami. Doped fiber amplifier and fiber laser. *https://www.mathworks.com/matlabcentral/fileexchange/50976-doped-fiber-amplifier-and-fiber-laser*, -(-):–, 2023.

[80] NH Sweilam, MM Khader, and AMS Mahdy. Crank-nicolson finite difference method for solving time-fractional diffusion equation. *Journal of Fractional Calculus and Applications*, 2(2):1–9, 2012.

[81] William H Press, Saul A Teukolsky, William T Vetterling, and Brian P Flannery. *Numerical recipes 3rd edition: The art of scientific computing*. Cambridge university press, 2007.

[82] Luke K Rumbaugh, Ming-Cheng Cheng, Yifei Li, and William D Jemison. Open-source fiber laser and amplifier design toolbox using custom fdtd simulation engine. In *Novel Optical Systems Design and Optimization XVII*, volume 9193, pages 103–116. SPIE, 2014.

[83] Amos Hardy and R Oron. Signal amplification in strongly pumped fiber amplifiers. *IEEE Journal of Quantum electronics*, 33(3):307–313, 1997.

[84] ST Davey and PW France. Rare earth doped fluorozirconate glasses for fibre devices. *British Telecom technology journal*, 7(1):58–68, 1989.

[85] Md Ziaul Amin, Matthew R Majewski, Robert I Woodward, Alexander Fuerbach, and Stuart D Jackson. Novel near-infrared pump wavelengths for dysprosium fiber lasers. *Journal of Lightwave Technology*, 38(20):5801–5808, 2020.

[86] HM Pask, Robert J Carman, David C Hanna, Anne C Tropper, Colin J Mackechnie, Paul R Barber, and Judith M Dawes. Ytterbium-doped silica fiber lasers: versatile sources for the 1-1.2/spl mu/m region. *IEEE Journal of Selected Topics in Quantum Electronics*, 1(1):2–13, 1995.

[87] Maria A Zachari, Panagiota S Chondrou, Stamatia E Pouliliou, Achilleas G Mitrakas, Ioannis Abatzoglou, Christos E Zois, and Michael I Koukourakis. Evaluation of the alamarblue assay for adherent cell irradiation experiments. *Dose-Response*, 12(2):dose–response, 2014.

Acknowledgements

Firstly, I want to thank Professor Annamaria Cucinotta for giving me the opportunity to work on these projects. Secondly, I would like to thank Professor Federica Poli for providing valuable guidance and feedback and challenging me to grow as a scientist. I would also like to express gratitude to Professor Stefano Selleri for his treasured support which was influential in the starting period of my PhD.

Appendix

- Appendix 1. Matlab Code for Solving Nonlinear Rate and Power-Propagation Equation in Dy-Doped Fiber Amplifiers or Fiber Sources

function [data,hFig,s] = AmplifierPerformance(s)
Using finite difference methods to solve the coupled PDEs

Uses the Forward-Time, Centered-Space explicit finite difference method
Inputs:
lamP - wavelength of pump
lamS - wavelength of signal
Pp - constant power of pump input
Ps - constant power of signal input
L - amplifier length
pump - pumping scheme: "core" or "cladding" options expected
s - settings structure with fields:
direction - pump direction: forward ("f"), reverse ("r"), bidirectional ("b"), or double-pass ("2") options expected
Ntot - doping concentration
dlam - optical sampling bandwidth (for ASE)
dz - spatial resolution of calculation
Outputs:
Z - vector of positions along fiber, for which solution was calculated
Y - matrix of values along fiber, with columns [P,S,ASEf,ASEb,n2]:

P - power of pump (direction determined from s.direction)
S - power of signal (forward propagating power at lamS)
ASEf - spectrally integrated forward propagating ASE (will not include lamS)
ASEb - spectrally integrated backward propagating ASE (will include lamS)
n2 - inversion RATIO (i.e. domain = [0,1]) where n2 = N2/Ntot

debugFlag = 0;

- INITIALIZATION

if nargin<1, s = struct; end
if isfield(s,'re'), s.re = 'erbium'; end
default to erbium, in our case Dy
if isfield(s,'pump'), s.pump = 'core'; end
if isfield(s,'plotFlag'),s.plotFlag = 1; end
if isfield(s,'mode'), s.mode = 'power'; end
if isfield(s,'direction'), s.direction = 'f'; end
if isfield(s,'dlam'),s.dlam = 2e-9; end
if isfield(s,'Pase'), s.Pase = 0; end
switch [lower(s.re(1)) lower(s.pump)]
case 'ecore' if isfield(s,'L'), s.L = 4; end
if isfield(s,'Ps'), s.Ps = 175 e-3; end
if isfield(s,'Pp'), s.Pp = 451 e-3; end
if isfield(s,'lamS'), s.lamS = 573 e-9; end
if isfield(s,'lamP'), s.lamP = 450 e-9; end
if isfield(s,'alpha'), s.alph = 6.5; end
if isfield(s,'Nt'), s.Nt = 3.66e25; end
ConvAbsDB2N(s.alph,GetDySpectrum(550));
if isfield(s,'dCore'), s.dCore = 12.5e-6; end
if isfield(s,'τ'),s.τ = 10e-3; end

if isfield(s,'τ_{32}'),s.τ_{32} = 100 e-6; end
if isfield(s,'τ_{21}'),s.τ_{21}= 1.5 e-3; end
if isfield(s,'τ_{30}'),s.τ_{30}= 1 e-2; end
if isfield(s,'τ_{10}'),s.τ_{10}= 650 e-6; end
if isfield(s,'R1'), s.R1 = 1; end
if isfield(s,'R2'), s.R2 = 1; end
if isfield(s,'R3'), s.R3 = 0.90; end
if isfield(s,'R4'), s.R4 = 0.50; end
if isfield(s,'nP'),
s.nP = min([75,s.L/0.01]);
s.nP = max([s.nP,s.L/0.010]); end
lam = [s.lamP (550e-9:s.dlam:600e-9)];
$[\sigma_{12}\ \sigma_{21}\ ]= GetDySpectrum(lam);$
$parameters$
$if\ isfield(s,'diffMethod'),s.diffMethod =' c';end$
$maxIterationsAllowed = 10e3;$
$makeInitialGuessFlag = false;$
$maxChangeAllowed = 0.0005;$
$ifdebugFlag, figure; end$

define physical constants
h = 6.626e-34;
c = 3e8;
n = 1.48;
vg = c/n;
R1 = 1;
R2 = 0.50;
R3 = 0.99;
R4 = 0.50;

define system parameters

```
z = 0:s.dz:s.L;
dt = s.dz/(2*vg);
lambdaF = dt/s.dz;
lambdaB = dt/(-s.dz);
dzSignF = 1;
dzSignB = -1;
alpha = 3e-3;
v = c./lam;
iiP = 1;
[~,iiS]= min(abs(s.lamS - lam));
aseTerm = GetASETerm(s.GammaS,σ21,lam,h,c,s.dlam,s.Nt);
Nlam = length(lam);
Nz = length(z);
Y = zeros(Nz,2*Nlam);
cl.Pf = 1;
cl.Pb = 2;
cl.Sf = iiS+1;
cl.Sb = Nlam+iiS+1;
cl.ASEf = [3:iiS,(iiS+2):(Nlam+1)];
cl.ASEb = [(Nlam+2):(Nlam+iiS),(Nlam+iiS+2):(2*Nlam)];
iiASE = cl.ASEf - 1;
dPdt = zeros(1,Nz);
dSfdt = zeros(1,Nz);
dAfdt_max = zeros(1,Nz);
dAbdt_max = zeros(1,Nz);


Compute Solution
fprintf('Solving BVP ... ');
tic;
maxres = 1;
n = 1;
```

```
N0 = s.Nt *ones(Nz,1);
N3 = s.Nt *zeros(Nz,1);
N2 = s.Nt *zeros(Nz,1);
N1 = s.Nt *ones(Nz,1);

Apply boundary conditions
Pump powers
switch s.direction
case 'f'
dzSignP = dzSignF;
cl.P = cl.Pf;
lambdaP = lambdaF;
Y(1,cl.Pf) = s.Pp*R1;
Y(end,cl.Pb) = 0;
case 'b','r'
dzSignP = dzSignB;
cl.P = cl.Pb;
lambdaP = lambdaB;
Y(1,cl.Pf) = 0;
Y(end,cl.Pb) = s.Pp;
end
Signal powers
Y(1,cl.Sf) = s.Ps*R3;
Y(end,cl.Sb) =0;
ASE powers
Y(1,cl.ASEf) = s.Pase;
Y(end,cl.ASEb) = s.Pase;

Solve fiber
```

```
while n <= maxIterationsAllowed


for zz = 2:(Nz-1)


zzF = zz;
zzB = (Nz-(zzF-1));


switch s.direction(1)
case 'f' ii0 = zzF - 1;
ii1 = zzF;
ii2 = zzF + 1;
case 'r','b' ii0 = zzB + 1;
ii1 = zzB;
ii2 = zzB - 1;
end
P0 = Y(ii0,cl.P);
P1 = Y(ii1,cl.P);
P2 = Y(ii2,cl.P);
switch lower(s.diffMethod(1))
case 'c'
D0 = - s.GammaP*sig12(iiP)*N0(ii0)*P0 ...
+ s.GammaP*sig21(iiP)*N3(ii0)*P0 - alpha*P0;
D1 = - s.GammaP*sig12(iiP)*N0(ii1)*P1 + s.GammaP*sig21(iiP)*N3(ii1)*P1 - al-
pha*P1;
D2 = - s.GammaP*sig12(iiP)*N0(ii2)*P2 + s.GammaP*sig21(iiP)*N3(ii2)*P2 - al-
pha*P2;
dPdz1 = dzSignP*(-vg*lambdaP/2)*(P2 - P0);
dPdz2 = (vg*vg*lambdaP*lambdaP/2)*(P2 - 2*P1 + P0);
Dscaled = (vg*dt)*D1;
dDdt = 0*(vg*dt/2)*(D1 + D1);
```

```
dDdz = dzSignP*(-vg*vg*dt*lambdaP/4)*(D2 - D0);
P1new = P1 + dPdz1 + dPdz2 + Dscaled + dDdt + dDdz;
case 'f','b'
de = - s.GammaP*sig12(iiP)*N0(ii0)*P0 + s.GammaP*sig21(iiP)*N3(ii0)*P0 - al-
pha*P0;
dPfdz = (P1 - P0) / (s.dz);
P1new = P1 + vg*dt*(de - dPfdz);
end
Y(ii1,cl.P) = P1new;
dPdt(ii1) = abs(10*log10(P1new/P1));
if isnan(dPdt(ii1)) || isinf(dPdt(ii1)), dPdt(ii1) = 0;
end


Sf0 = Y(zzF-1,cl.Sf);
Sf1 = Y(zzF,cl.Sf);
Sf2 = Y(zzF+1,cl.Sf);
switch lower(s.diffMethod(1))
case 'c'
D0 = - s.GammaS*sig12(iiS)*N1(zzF-1)*Sf0 ... + s.GammaS*sig21(iiS)*N2(zzF-
1)*Sf0 ... + aseTerm(iiS)*N2(zzF-1)/s.Nt ... - alpha*Sf0;
D1 = - s.GammaS*sig12(iiS)*N1(zzF)*Sf1 ... + s.GammaS*sig21(iiS)*N2(zzF)*Sf1
... + aseTerm(iiS)*N2(zzF)/s.Nt ... - alpha*Sf1;
D2 = - s.GammaS*sig12(iiS)*N1(zzF+1)*Sf2 ... + s.GammaS*sig21(iiS)*N2(zzF+1)*Sf2
... + aseTerm(iiS)*N2(zzF+1)/s.Nt ... - alpha*Sf2;
dSfdz1 = dzSignF*(-vg*lambdaF/2)*(Sf2 - Sf0);
dSfdz2 = (vg*vg*lambdaF*lambdaF/2)*(Sf2 - 2*Sf1 + Sf0);
Dscaled = (vg*dt)*D1;
dDdt = 0*(vg*dt/2)*(D1 + D1);
dDdz = dzSignF*(-vg*vg*dt*lambdaF/4)*(D2 - D0);
Sf1new = Sf1 + dSfdz1 + dSfdz2 + Dscaled + dDdt + dDdz;
case 'f','b'
```

```
de = - s.GammaS*sig12(iiS)*N1(zzF)*Sf0 ...
+ s.GammaS*sig21(iiS)*N2(zzF)*Sf0 ...
+ aseTerm(iiS)*N2(zzF)/s.Nt ... - alpha*Sf0;
dSfdz = (Sf1 - Sf0) / (s.dz);
Sf1new = Sf1 + vg*dt*(de - dSfdz);
end
Y(zzF,cl.Sf) = Sf1new;
dSfdt(zzF) = abs(10*log10(Sf1new/Sf1));
if isnan(dSfdt(zzF)) || isinf(dSfdt(zzF)), dSfdt(zzF) = 0;
end


ASE Forward: FTCS
Af0 = Y(zzF-1,cl.ASEf);
Af1 = Y(zzF,cl.ASEf);
Af2 = Y(zzF+1,cl.ASEf);
switch lower(s.diffMethod(1))
case 'c'
D0 = - s.GammaS*sig12(iiASE)'.*N1(zzF-1).*Af0 ... + s.GammaS*sig21(iiASE)'.*N2(zzF-
1).*Af0 ... + aseTerm(iiASE)'.*N2(zzF-1)./s.Nt ... - alpha*Af0;
D1 = - s.GammaS*sig12(iiASE)'.*N1(zzF).*Af1 ... + s.GammaS*sig21(iiASE)'.*N2(zzF).*Af1
... + aseTerm(iiASE)'.*N2(zzF)./s.Nt ... - alpha*Af1;
D2 = - s.GammaS*sig12(iiASE)'.*N1(zzF+1).*Af2 ... + s.GammaS*sig21(iiASE)'.*N2(zzF+1).*Af2
... + aseTerm(iiASE)'.*N2(zzF+1)./s.Nt ... - alpha*Af2;
dAfdz1 = dzSignF*(-vg*lambdaF/2)*(Af2 - Af0);
dAfdz2 = (vg*vg*lambdaF*lambdaF/2)*(Af2 - 2*Af1 + Af0);
Dscaled = (vg*dt)*D1;
dDdt = 0*(vg*dt/2)*(D1 + D1);
dDdz = dzSignF*(-vg*vg*dt*lambdaF/4)*(D2 - D0);
Af1new = Af1 + dAfdz1 + dAfdz2 + Dscaled + dDdt + dDdz;
case 'f','b'
de = -s.GammaS*sig12(iiASE)'.*N1(zzF).*Af0 ... + s.GammaS*sig21(iiASE)'.*N2(zzF).*Af0
```

```
... + aseTerm(iiASE)'.*N2(zzF)./s.Nt ... - alpha*Af0;
dAfdz = (Af1 - Af0) ./ (s.dz);
Af1new = Af1 + vg*dt*(de - dAfdz);
end
Y(zzF,cl.ASEf) = Af1new;
dAfdt = abs(10*log10(Af1new./Af1));
dAfdt_max(zzF) = max(dAfdt);
if isnan(dAfdt_max(zzF))||isinf(dAfdt_max(zzF)), dAfdt_max(zzF) = 100;
end
```

```
ASE Backward: FTCS
Ab0 = Y(zzB+1,cl.ASEb);
Ab1 = Y(zzB,cl.ASEb);
Ab2 = Y(zzB-1,cl.ASEb);
switch lower(s.diffMethod(1))
case 'c'
D0 = - s.GammaS*sig12(iiASE)'.*N1(zzB-1).*Ab0 ... + s.GammaS*sig21(iiASE)'.*N2(zzB-
1).*Ab0 ... + aseTerm(iiASE)'.*N2(zzB-1)./s.Nt ... - alpha*Ab0;
D1 = - s.GammaS*sig12(iiASE)'.*N1(zzB).*Ab1 ... + s.GammaS*sig21(iiASE)'.*N2(zzB).*Ab1
... + aseTerm(iiASE)'.*N2(zzB)./s.Nt ... - alpha*Ab1;
D2 = - s.GammaS*sig12(iiASE)'.*N1(zzB+1).*Ab2 ... + s.GammaS*sig21(iiASE)'.*N2(zzB+1).*Ab2
... + aseTerm(iiASE)'.*N2(zzB+1)./s.Nt ... - alpha*Ab2;
dAbdz1 = dzSignB*(-vg*lambdaB/2)*(Ab2 - Ab0);
dAbdz2 = (vg*vg*lambdaB*lambdaB/2)*(Ab2 - 2*Ab1 + Ab0);
Dscaled = (vg*dt)*D1;
dDdt = 0*(vg*dt/2)*(D1 + D1);
dDdz = dzSignB*(-vg*vg*dt*lambdaB/4)*(D2 - D0);
Ab1new = Ab1 + dAbdz1 + dAbdz2 + Dscaled + dDdt + dDdz;
case 'f','b'
de = -s.GammaS*sig12(iiASE)'.*N1(zzB).*Ab0 ... + s.GammaS*sig21(iiASE)'.*N2(zzB).*Ab0
... + aseTerm(iiASE)'.*N2(zzB)./s.Nt ... - alpha*Ab0;
```

```
dAbdz = (Ab1 - Ab0) ./ (s.dz);
Ab1new = Ab1 + vg*dt*(de - dAbdz);
end
Y(zzB,cl.ASEb) = Ab1new;
dAbdt = abs(10*log10(Ab1new./Ab1));
dAbdt_max(zzB) = max(dAbdt);
if isnan(dAbdt_max(zzB))||isinf(dAbdt_max(zzB)),dAbdt_max(zzB) = 100;
end

dAfdt_max(zzF) = 0;
dAbdt_max(zzB) = 0;

end

for zz = Nz

zzF = zz;
zzB = (Nz-(zzF-1));

switch s.direction(1)
case 'f'
ii0 = zzF - 1;
ii1 = zzF;
case 'r','b'
ii0 = zzB + 1;
ii1 = zzB;
end
P0 = Y(ii0,cl.P);
P1 = Y(ii1,cl.P);
de = - s.GammaP*sig12(iiP)*N1(zz)*P0 ... + s.GammaP*sig21(iiP)*N2(zz)*P0 ... -
```

```
alpha*P0;
dPfdz = dzSignP*(P1 - P0)/(dzSignP*s.dz);
P1new = P1 + vg*dt*(de - dPfdz);
P1new = max([0,P1new]);
Y(ii1,cl.P) = P1new;
dPdt(ii1) = abs(10*log10(P1new/P1));
if isnan(dPdt(ii1)) || isinf(dPdt(ii1)), dPdt(ii1) = 0;
end

Sf0 = Y(zzF-1,cl.Sf);
Sf1 = Y(zzF,cl.Sf);
de = - s.GammaS*sig12(iiS)*N1(zzF)*Sf0 ... + s.GammaS*sig21(iiS)*N2(zzF)*Sf0
... + aseTerm(iiS)*N2(zzF)/s.Nt ... - alpha*Sf0;
dSfdz = dzSignF*(Sf1 - Sf0)/(dzSignF*s.dz);
Sf1new = Sf1 + vg*dt*(de - dSfdz);
Sf1new = max([0,Sf1new]);
Y(zzF,cl.Sf) = Sf1new;
dSfdt(zzF) = abs(10*log10(Sf1new/Sf1));
if isnan(dSfdt(zzF)) || isinf(dSfdt(zzF)), dSfdt(zzF) = 0;
end

ASE Forward: FTFS
Af0 = Y(zzF-1,cl.ASEf);
Af1 = Y(zzF,cl.ASEf);
de = - s.GammaS.*sig12(iiASE)'.*N1(zzF).*Af0 ... + s.GammaS.*sig21(iiASE)'.*N2(zzF).*Af0
... + aseTerm(iiASE)'.*N2(zzF)./s.Nt ... - alpha*Af0;
dAfdz = dzSignF*(Af1 - Af0)/(dzSignF*s.dz);
Af1new = Af1 + vg*dt*(de - dAfdz);
Af1new(Af1new<0) = 0;
Y(zzF,cl.ASEf) = Af1new;
dAfdt = abs(10*log10(Af1new./Af1));
```

dAfdt$_max(zzF) = max(dAfdt)$;
$if isnan(dAfdt_max(zzF))||isinf(dAfdt_max(zzF)), dAfdt_max(zzF) = 100$;
end

Ab0 = Y(zzB+1,cl.ASEb);
Ab1 = Y(zzB,cl.ASEb);
de = - s.GammaS*sig12(iiASE)'.*N1(zzB).*Ab0 ... + s.GammaS*sig21(iiASE)'.*N2(zzB).*Ab0 ... + aseTerm(iiS)'.*N2(zzB)./s.Nt ... - alpha*Ab0;
dAbdz = dzSignB*(Ab1 - Ab0)/(dzSignB*s.dz);
Ab1new = Ab1 + vg*dt*(de - dAbdz);
Ab1new(Ab1new<0) = 0;
Y(zzB,cl.ASEb) = Ab1new;
dAbdt = abs(10*log10(Ab1new./Ab1));
dAbdt$_max(zzB) = max(dAbdt)$;
$if isnan(dAbdt_max(zzB))||isinf(dAbdt_max(zzB)), dAbdt_max(zzB) = 100$;
end

end
END POWER PROPAGATION CALCULATIONS FOR THIS UPDATE

Calculate inversion based on a four-level system
R12 = Y(:,cl.P)*sig12(iiP)./(h*v(iiP)*Ap/s.Gamma);
W12 = Y(:,cl.Sf)*sig12(iiS)./(h*v(iiS)*As/s.Gamma);
W12ASEf = sum((Y(:,cl.ASEf).*repmat(sig12(iiASE)',[Nz,1])./(h*repmat(v(iiASE)',[Nz 1])*As/s.Gamma)) ,2);
W12ASEb = sum((Y(:,cl.ASEb).*repmat(sig12(iiASE)',[Nz,1])./(h*repmat(v(iiASE)',[Nz 1])*As/s.Gamma)) ,2);
R21 = Y(:,cl.P)*sig21(iiP)./(h*v(iiP)*Ap/s.Gamma);
W21 = Y(:,cl.Sf)*sig21(iiS)./(h*v(iiS)*As/s.Gamma);
W21ASEf = sum((Y(:,cl.ASEf).*repmat(sig21(iiASE)',[Nz,1])./(h*repmat(v(iiASE)',[Nz

1])*As/s.Gamma)) ,2);
W21ASEb = sum((Y(:,cl.ASEb).*repmat(sig21(iiASE)',[Nz,1])./(h*repmat(v(iiASE)',[Nz
1])*As/s.Gamma)) ,2);
W03 = R12;
W30 = R21;
A21 = ones(Nz,1)./s.tau$_2$1;
$A32 = ones(Nz,1)./s.tau_3 2$;
$A30 = ones(Nz,1)./s.tau_3 0$;
$A10 = ones(Nz,1)./s.tau_1 0$;
$N2 = s.Nt*(W12+W12ASEf+W12ASEb+A10)./...((W12+W12ASEf+W12ASEb+$
$A10)+(W21+W21ASEf+W21ASEb+A21).*((W03+W30+A30+A32).*(A10./(A32.*$
$R12))+1))$;
$N1 = s.Nt*(W21+W21ASEf+W21ASEb+A21)./...((W12+W12ASEf+W12ASEb+$
$A10)+(W21+W21ASEf+W21ASEb+A21).*((W03+W30+A30+A32).*(A10./(A32.*$
$R12))+1))$;
$N3 = (A10./A32).*N1$;
$N0 = s.Nt-(N1+N2+N3)$;

if n>1 max([max(dPdt) max(dSfdt) max(dAfdt$_m$ax)$+max(dAbdt_max)]) < maxChangeAllowed, break;$
end

n = n + 1;
end

if n>maxIterationsAllowed,
fprintf('*** Failed to converge after
Z = z';
Yout = zeros(length(Z),5);
Psout = 0;
s.displayFlag = false;

```
s.displayASEFlag = false;
else
fprintf('*** Done after %.2f seconds and %d iterations. ',toc,n);
organize output
Y = Y;
Z = z';
n2 = N2/s.Nt;
n1 = N1/s.Nt;
n3 = N3/s.Nt;
N0 = s.Nt -(N1+N2+N3);
n0 = N0/s.Nt
switch lower(s.direction(1))
case 'f','r','b'
Yout = [Y(:,cl.Pf)+Y(:,cl.Pb) Y(:,cl.Sf) sum(Y(:,cl.ASEf),2) sum(Y(:,cl.ASEb),2)+Y(:,cl.Sb)
n2 n1 n3 n0 Y(:,cl.Sb)];


Psout = Yout(end,2);
PaseF = Yout(end,3);
PaseB = Yout(1,4);


case '2'
Yout = [Y(:,cl.Pf)+Y(:,cl.Pb) Y(:,cl.Sb) sum(Y(:,cl.ASEf),2) sum(Y(:,cl.ASEb),2) n2
Y(:,cl.Sb)];
Psout = Yout(1,2);
PaseF = Yout(end,3);
PaseB = Yout(1,4);
end
end


if s.plotFlag
```

```
hFig = figure('windowstyle','docked');
Zp = Z*100;

switch(lower(s.mode(1)))
case 'p'
if s.Pp>2,
ylabStr = 'Pump/Signal Power (W)';
yr1 = [0 max([s.Pp s.Ps])*1.1];
else
ylabStr = 'Pump/Signal Power (mW)';
Yout(:,1:4)=Yout(:,1:4)*1000;
yr1 = [0 max([s.Pp s.Ps])*1700];
end
h1 = plot(Zp,Yout(:,1),'LineWidth',2);
hold on;
h3 = plot(Zp,Yout(:,2),'LineWidth',2);
grid on ;
set(h1,'LineWidth',4,'Color','b');
set(h3,'LineWidth',4,'Color','r');

legVect = [h1 h3];

ylim(yr1);

xlabel('Fiber Length (cm)');
ylabel(ylabStr);

case 'g'
Gsf = 10*log10(Y(:,cl.Sf)./s.Ps);
```

```
h4 = plot(Zp,Gsf,'LineWidth',2);
grid on;
yr1 = [-10 65];
ylabStr = 'Signal Gain (dB)';
legVect = [h4];
set(h4,'LineWidth',4,'Color','r');
ylim(yr1);


xlabel('Z (cm)');
ylabel(ylabStr);
ylabel(ylabStr);


case 'a'
xsurf = Z;
ysurf = lam([2:(iiS-1),(iiS+1):end])';
zsurf = Y(:,cl.ASEf) + Y(:,cl.ASEb);
zsurf = 1000*zsurf;
zlabelStr = 'Power (mW)';
xsurf = 100*repmat(xsurf,[1,size(zsurf,2)]);
ysurf = 1e9*repmat(ysurf,[size(zsurf,1),1]);
surf(xsurf,ysurf,zsurf);
hT = title('Distribution of ASE Power in Amplifier');
set(hT,'fontsize',18);
set(gca,'fontsize',16,'linewidth',2);
xlabel('Fiber Length (cm)');
ylabel('Wavelength (nm)');
zlabel(zlabelStr);


if isfield(s,'output')
if s.output == 'z'
```

```
data1 = z;
data2 = Yout(:,2);
data3 = Yout(:,1);
else
data = Psout;
end else
data = Psout;
end

function aseTerm = GetASETerm(GammaS,sig21,lam,h,c,dlam,Ntot)
aseTerm = 2*dlam*GammaS.*sig21.*(h*(c^2)./(lam.^3)) * Ntot;

end
```